REMOTE FIELD EDDY CURRENT BASED APPROACHES FOR HIGH SENSITIVE DETECTION OF DEFECTS IN FERROMAGNETIC STEAM GENERATOR TUBES

By

S. THIRUNAVUKKARASU
(Enrollment No: ENGG02200704006)

Indira Gandhi Centre for Atomic Research, Kalpakkam

A thesis submitted to the

Board of Studies in Engineering Sciences

In partial fulfillment of requirements

for the Degree of

DOCTOR OF PHILOSOPHY

of

HOMI BHABHA NATIONAL INSTITUTE

December, 2013

Homi Bhabha National Institute

Recommendations of the Viva Voce Board

As members of the Viva Voce Board, we certify that we have read the dissertation prepared by **S. Thirunavukkarasu** entitled "**Remote field eddy current based approaches for high sensitive detection of defects in ferromagnetic steam generator tubes**" and recommend that it may be accepted as fulfilling the dissertation requirement for the Degree of Doctor of Philosophy.

______________________________ **Date:** 01 Jan. 2015

Chairman-**Dr. T. Jayakumar**

______________________________ **Date:** 1/1/2015

Guide / Convener-**Dr. B. Purna Chandra Rao**

______________________________ **Date:** 01/01/2015

Member 1-**Dr. B.K. Panigrahi**

V.S. Srinivasan______________________________ **Date:** 1/1/2015

Member 2-**Dr. V.S. Srinivasan**

______________________________ **Date:** 1 JAN 2015

External Examiner

Final approval and acceptance of this dissertation is contingent upon the candidate's submission of the final copies of the dissertation to HBNI.

I hereby certify that I have read this dissertation prepared under my direction and recommend that it may be accepted as fulfilling the dissertation requirement.

Date: 1/1/2015

Place: Kalpakkam **Guide**

STATEMENT BY AUTHOR

This dissertation has been submitted in partial fulfillment of requirements for an advanced degree at Homi Bhabha National Institute (HBNI) and is deposited in the library to be made available to borrowers under rules of the HBNI.

Brief quotations from this dissertation are allowable without special permission, provided that accurate acknowledgement of source is made. Requests for permission for extended quotation from or reproduction of this manuscript in whole or in part may be granted by the Competent Authority of HBNI when in his or her judgment the proposed use of the material is in the interests of scholarship. In all other instances, however, permission must be obtained from the author.

(S. Thirunavukkarasu)

Date: 01.01.15

Place: Kalpakkam

DECLARATION

I, hereby declare that the investigation presented in the thesis entitled **"Remote field eddy current based approaches for high sensitive detection of defects in ferromagnetic steam generator tubes"** submitted to Homi Bhabha National Institute (HBNI), Mumbai, India, for the award of **Doctor of Philosophy in Engineering** Sciences, is the record of work carried out by me under the guidance of **Dr. B. Purna Chandra Rao**, Head, Non-Destructive Evaluation Division, Metallurgy and Materials Group, Indira Gandhi Centre for Atomic Research, Kalpakkam. The work is original and has not been submitted earlier as a whole or in part for a degree / diploma at this or any other Institution/University.

(S. Thirunavukkarasu)

Date: 01.01.15

Place: Kalpakkam

LIST OF JOURNAL PUBLICATIONS

1) **S. Thirunavukkarasu**, B.P.C. Rao, G.K. Sharma, Viswa Chaithanya, C. Babu Rao, T. Jayakumar, Baldev Raj, Aravinda Pai, T.K. Mitra and Pandurang Jadhav, "Methodology for non-destructive assessment of integrity of steam generator shell welds", International Journal of Structural Integrity, Vol. 2, No. 2, pp. 145-157, 2011.

2) **S. Thirunavukkarasu**, B.P.C. Rao, T. Jayakumar and Baldev Raj, "Techniques for processing remote field eddy current signals from bend regions of steam generator tubes of Prototype Fast Breeder Reactor", Annals of Nuclear Energy, Vol. 38, pp. 817-824, 2011.

3) **S. Thirunavukkarasu**, B.P.C. Rao, S. Mahadevan, T. Jayakumar, Baldev Raj, Z. Zeng, Lalita Udpa and S. Satish. Udpa, Finite element modeling for detection of localized defects using remote field eddy current technique, Journal of Research in Nondestructive Evaluation (Taylor and Francis), Vol.20, No. 3, pp. 145-258, 2009.

4) **S. Thirunavukkarasu**, B.P.C. Rao, S. Vaidyanathan, T. Jayakumar and Baldev Raj, "Influence of Sodium Deposits in Steam Generator Tubes on Remote Field Eddy Current Signals", International Journal of Pressure Vessels and Piping, Vol. 85, No. 4, pp. 211-218, March 2008.

Solely dedicated to

my Mother

ACKNOWLEDGEMENTS

I owe my deep sense of gratitude to my research supervisor and mentor Dr. B. Purna Chandra Rao, Head, Nondestructive Evaluation Division (NDED), Indira Gandhi Centre for Atomic Research (IGCAR) for his guidance, consistent encouragement and all round support that led to the successful completion of this work. I have benefited immensely from many fruitful discussions with him and I would cherish the lessons learnt from him during my entire career, in the years to come.

I express my sincere gratitude to Dr. T. Jayakumar, Director, Metallurgy and Materials Group, IGCAR and the Chairman of my doctoral committee, for his inspiration, encouragement and most importantly providing direction during the course of thesis work. I would like to extend my heartfelt thanks to the former directors of IGCAR, Dr. Baldev Raj and Shri S. C. Chetal and the present Director, Dr. P. R. Vasudeva Rao, for permitting me to pursue research in this reputed centre. I thank eminent members of the doctoral committee Dr. B.K. Panigrahi and Dr. V.S. Srinivasan for their regular appraisal, kind advice and suggestions to improve the quality of this work.

I take this opportunity to thank Dr. C. K. Mukhopadhyay, Head, EMSI section, NDED, IGCAR for providing me the freedom to pursue this research work. My sincere thanks to Shri S. Mahadevan, Program Leader, XRDM, NDED, IGCAR, for providing his valuable advice, time and guidance during the entire research work. I wish to acknowledge Shri S. Shuaib Ahmed, Senior Research Fellow (SRF), HBNI, for providing me technical support in various occasions of the thesis work and extending his help in the preparation of the manuscript in an effective manner. I thank Shri Govind Kumar Sharma for spending his valuable time in reading thesis and proof correcting before the printing.

My thanks are also due to my fellow colleagues Smt. B. Sasi, Dr. W. Sharatchandra Singh, Shri S. Ponseenivasan, Shri V. Arjun, who have helped me to learn various technical ingredients for analysis of the results and assisting me in correcting the manuscript. My grateful thanks are due to Shri P. Krishnaiah (Retired), Shri K. Sambasiva Rao, SRF, HBNI and Shri Anil Kumar, SRF, HBNI, for their help in the fabrication of RFEC probes and electronic circuits. I extend my sincere thanks to the staff members of IDEAS, MMG, IGCAR, for their timely help in the fabrication of formers for various types of RFEC probes. I also thank the staff members of the NDED for assisting me in various ways to effectively work and complete the research work. I also thank the anonymous reviewers whose valuable comments were very much useful to improve the technical content of the thesis.

This work would not have been possible but for the love, sacrifice, patience and support of my wife Smt J. Jayachitra and my daughters Kum. Harini and Kum. Shalini. I also specially thank my daughter Harini for all her help in collating the references of the thesis. I also sincerely thank my relatives and friends who were accommodating and supporting during the course of this work.

(S. Thirunavukkarasu)

TABLE OF CONTENTS

ABSTRACT		**V**
LIST OF FIGURES		**VII**
LIST OF TABLES		**XII**
CHAPTER 1	**: INTRODUCTION**	**1**
1.1	Components of fast breeder reactor	1
1.2	Steam generators of PFBR	1
1.3	Introduction to nondestructive evaluation	6
1.4	Electromagnetic nondestructive evaluation techniques	8
1.4.1	Eddy current technique	8
1.4.1.1	Eddy current probes	11
1.4.1.2	Eddy current instrument	14
1.4.2	Magnetic flux leakage technique	15
1.4.3	Magnetic Barkhausen emission technique	16
1.4.4	Potential drop technique	17
1.4.5	Other ENDE techniques	19
1.4.6	General characteristics of ENDE techniques	20
1.5	State of the art ENDE of tubes	21
1.5.1	Testing of non-ferromagnetic tubes	21
1.5.1.1	Rotating probe/tube technique	22
1.5.2	Testing of ferromagnetic tubes	23
CHAPTER 2	**: MOTIVATION AND OBJECTIVE**	**25**
2.1	Introduction	25
2.2	NDE of PFBR steam generator tubes	25
2.2.1	NDE during manufacturing and quality assurance	25
2.2.1.1	Saturation eddy current testing	25
2.2.2	NDE of installed SG tubes for in-service inspection	27
2.3	Principle of remote field eddy current technique	28

2.4 Important features of RFEC technique 32
2.5 State of the art of RFEC technique 33
2.5.1 RFEC technique and probe 34
2.5.2 RFEC instrumentation 37
2.5.3 RFEC detection of defects 40
2.6 Motivation 45
2.7 Objective of the thesis 47
2.8 Organization of the thesis 47

CHAPTER 3 : MODEL BASED APPROACH FOR OPTIMIZATION AND EXPERIMENTAL VALIDATION 49

3.1 Introduction 49
3.2 Finite element modeling 49
3.3 Differential formulation of RFEC problem 50
3.4 The FEMM software 52
3.5 Formalism for nonlinear material modeling 53
3.6 Determination of the BH curve of modified 9Cr-1Mo steel 55
3.6.1 Experimental procedure 55
3.6.2 Computation of H and B fields from the measured current and voltage values 55
3.7 Modeling of RFEC technique 57
3.7.1 Construction of the model geometry 57
3.7.2 Boundary conditions 58
3.7.3 Meshing of the model geometry 59
3.7.4 Solving the model 61
3.7.5 Post-processing of model predicted vector potential 61
3.8 Finite element model predictions 62
3.8.1 Optimization of the exciter-receiver coil spacing 66
3.8.2 Optimization of operating frequency 68
3.8.3 Prediction of RFEC signals of grooves 68
3.9 Development of RFEC instrumentation 70
3.9.1 Excitation unit 71
3.9.2 Receiver unit 73

3.10	Development of RFEC probe	76
3.11	Performance evaluation	77
3.12	Experimental validation of the model predictions	79
3.13	Discussion	82
3.14	Summary	85

CHAPTER 4 : SIGNAL PROCESSING APPROACH FOR NDE OF BEND REGION **87**

4.1	Introduction	87
4.2	Detection of defects in the straight section of SG tube	87
4.3	Issues with detection of defects in the bend regions of SG tubes	90
4.4	Signal processing techniques	92
4.4.1	Fourier filtering technique	92
4.4.2	Cross-correlation technique	93
4.4.3	Wavelet transform technique	94
4.5	Experimental measurements in bend regions of SG tube	96
4.6	Results of the application of signal processing techniques	99
4.6.1	Fourier filtering technique	99
4.6.2	Cross-correlation technique	102
4.7	Discussion	106
4.8	Summary	109

CHAPTER 5 : APPROACHES BASED ON SIGNAL FEATURE IDENTIFICATION AND MULTIFREQUENCY MIXING **111**

5.1	Introduction	111
5.2	Experimental studies on sodium influence on RFEC signals	111
5.3	Studies in sodium test vessel	111
5.4	Results of the experimental studies	114
5.5	Model based investigation of the sodium influence	120
5.6	Multifrequency mixing approach	123
5.7	Background of the multifrequency mixing technique	124
5.8	New multifrequency mixing algorithm	125
5.9	Multifrequency mixing of model predicted signals	126
5.10	Discussion	133

5.11 Summary 135

CHAPTER 6 : CONCLUSIONS 138

6.1 Technical and scientific contribution 141

CHAPTER 7 : FUTURE WORKS 142

REFERENCES 144

ABSTRACT

This thesis proposes different approaches for high sensitive detection of defects in ferromagnetic steam generator (SG) tubes using remote field eddy current (RFEC) nondestructive testing technique. The thesis considers modified 9Cr-1Mo ferromagnetic SG tubes (OD 17.2 mm and thickness 2.5 mm) of prototype fast breeder reactor (PFBR) in India. Effective inspection of SG tubes using RFEC technique requires due consideration of the following issues:

1) Design and development of high sensitive RFEC instrument and optimized probes to reliably detect localized defects in SG tubes.
2) Reliable detection of defects in expansion bend regions of the SG tubes.
3) Detection of defects in the presence of sodium deposits on the SG tubes and also in the defects
4) Detection of defects under Inconel support structures.

A nonlinear finite element model has been proposed to understand the RFEC technique in the SG tubes, to precisely identify the RFEC region for placing the receiver coil and to optimize the operating frequency for enhanced detection of defects. The thesis details the design and development of RFEC instrument that uses harmonic-free stable excitation source and lock-in amplifier to measure small amplitude response from localized defects. The capability of the instrument has been demonstrated by detecting localized defects as small as 0.46 mm which is 20% of the tube wall thickness (WT) in the straight sections of the SG tube using an optimized RFEC probe.

For reliable detection of defects in the bend regions of the SG tubes, continuous wavelet transform (CWT) based digital signal processing approach has been

developed, after systematically analysing the Fourier filtering, cross correlation and wavelet transform based digital signal processing techniques on a series of defects in the bend regions. CWT processing using the optimized Bior2.8 wavelet could reliably detect 0.23 mm (10% WT) deep grooves anywhere in the bend regions of the SG tube with SNR of 7 dB.

A first of its kind experimental investigation has been carried out, to study the influence of sodium deposits in the defect regions of the SG tube, on RFEC signals. A definite influence of sodium has been observed from the experimental studies. RFEC signal parameters have been identified based on the systematic studies before and after the formation of the sodium deposits in the defective regions. An approach based on invariant parameter of the RFEC signals has been proposed for detection and sizing of defects deeper than 0.23 mm (10% WT) in the presence of sodium deposits.

For detection of defects under Inconel support structures, a novel dual frequency mixing algorithm based on linear kernel transform (LKT) has been developed. The performance of the mixing algorithm has been demonstrated on model predicted RFEC signals of grooves (depth 20% WT, 30% WT, and 40% WT) under support structures. The robustness of the mixing algorithm has been assessed for detection of outer surface grooves partially and fully off-centered with the support structure, with very good success.

Capabilities of the approaches for detection of defects have been analyzed and future directions have been set towards high probability of detection of defects, anywhere in the SG tubes. The proposed approaches will enable reliable in-service inspection of SG tubes, ensuring structural integrity and safety of SGs of PFBR.

LIST OF FIGURES

Figure No. **Captions** **Page No.**

Figure 1.1 Components of the Prototype Fast Breeder Reactor. 2
Figure 1.2 a) Schematic of the PFBR SG b) photograph of the SG tube sheet and c) tube bundle during fabrication stages in the shop floor. 3
Figure 1.3 Impingement wastage on SG tube during controlled experiments [6]. 5
Figure 1.4 Schematic of a generic NDE system. 7
Figure 1.5 Schematic of the eddy current technique and distortion of eddy currents [12]. 9
Figure 1.6 Type of eddy current probes used for different geometries [14]................ 12
Figure 1.7 Typical EC probes (pencil, pancakde, ring, encircling and bobbin) used for specific applications [12]. 13
Figure 1.8 Typical eddy current signals of various defects in a tube obtained by bobbin type differential probe [14]. 14
Figure 1.9 Principle of magnetic flux leakage technique [17].................................... 15
Figure 1.10 Discrete changes during the magnetization process and Barkhausen emissions observed in a ferromagnetic material [8]. 17
Figure 1.11 Principles of potential drop measurement technique [22]....................... 18
Figure 1.12 Typical tube sheet and differential bobbin probes used for EC testing. 22
Figure 2.1 Flow sheet of the quality control of SG tubes [35]. 26
Figure 2.2 Saturation EC test setup for quality assurance of SG tubes [36]. 26
Figure 2.3 EC signals (vertical component) of the through holes of 1.2 mm diameter without and with magnetic saturation. 27
Figure 2.4 Principle of RFEC technique.. 29
Figure 2.5 The field log for a moving ID receiver coil from an exciter coil [42] 30
Figure 2.6 Magnetic field profile insider the ferromagnetic tube wall [43]. 31
Figure 2.7 RFEC amplitude signals for uniform wall thinning grooves [45]............. 32
Figure 2.8 Difference between the linear and nonlinear model predicted induced voltages (μV) in the RFEC receiver coil as a function of excitation current (A) [43]. 37

Figure 2.9 Schematic of the RFEC instrument used in [59]. 39
Figure 2.10 Slope of the Phase-frequency curves for support plate and defects [65]. 44
Figure 3.1 Experimentally obtained BH curve of modified 9Cr-1Mo steel. 56
Figure 3.2 Geometric model of the RFEC technique. 58
Figure 3.3 Triangular mesh generated in the RFEC geometric model. 60
Figure 3.4 Surface plot of the logarithm of magnetic flux density and normalized arrow plots of the magnetic field at frequencies 700, 800 and 900 Hz. 63
Figure 3.5 Amplitude and phase of the induced voltage in a receiver coil in the frequency range of 100 Hz to 500 Hz. 64
Figure 3.6 Amplitude and phase of the induced voltage in a receiver coil in the frequency range of 600 Hz to 1000 Hz. 65
Figure 3.7 Amplitude and phase of the induced voltage in a receiver coil in the frequency range of 1100 Hz to 1500 Hz. 65
Figure 3.8 Characterization of direct, transition and remote field zones. 67
Figure 3.9 RFEC signal amplitude of a grooves (width 3 mm, and depth 10%, 20% and 30% WT) predicted at different frequencies. 69
Figure 3.10 Model predicted RFEC signals of 20%, 30% and 40% WT grooves in the tube. 70
Figure 3.11 Schematic of the RFEC instrument. 71
Figure 3.12 Control system logic of the current source. 72
Figure 3.13 Schematic of the lock-in amplifier. 74
Figure 3.14 RFEC instrument and computer controlled data acquisition system. 75
Figure 3.15 Flexible RFEC probe developed for negotiation of bend regions in SG tubes. 77
Figure 3.16 Schematic of the calibration tube with reference defects. 78
Figure 3.17 Experimentally measured real and imaginary components of the RFEC signals (at 825 Hz) of reference defects as per ASME Section V Article.17. 78
Figure 3.18 Experimentally measured RFEC signals of 0.46 mm (20% WT), 0.69 mm (30% WT) and 0.92 mm (40% WT) deep grooves in SG tube. 80

Figure 3.19 Measured and model predicted RFEC signals. 81
Figure 3.20 Measured and linear model predicted RFEC signals. 82
Figure 3.21 Comparative behavior of linear and nonlinear models. 84
Figure 4.1 RFEC signals for grooves of 3 mm width at 825 Hz. 88
Figure 4.2 RFEC signals for 5 mm diameter flat bottom holes of different depths. 88
Figure 4.3 RFEC signals of 5 mm length, 2.3 mm width axial notches of different depths. 89
Figure 4.4 RFEC signals of 5 mm length, 2.3 mm width circumferntial notches of different depths. 90
Figure 4.5 Typical RFEC signals from the bend regions of the SG tube having grooves at three characteristic locations and the photograph of the bend tube. 91
Figure 4.6 Different wavelets considered for processing of the RFEC signals. 95
Figure 4.7 Schematic of SG tube with grooves D1, D2 and D3 in the bend region. 96
Figure 4.8 RFEC signals from tube defect-free bend tube (T1). 98
Figure 4.9 RFEC signals from tube T2 having 10% WT grooves in the bend regions. 99
Figure 4.10 RFEC signals from tube T3 having 20% WT grooves in the bend regions. 99
Figure 4.11 SNR as function of lower and upper cut-off band-pass frequencies for RFEC signals of tube T3. 100
Figure 4.12 Results of application of Fourier filtering to RFEC signals of defect-free tube T1, tube T2 having three 10% WT deep grooves and tube T3 having three 20% WT deep grooves. 102
Figure 4.13 Results of application of cross correlation technique to RFEC signals of defect-free tube T1, tube T2 having three 10% WT deep grooves and tube T3 having three 20% WT deep grooves. 104
Figure 4.14 Wavelet transform processed RFEC signals of defect-free bend tube T1, tube T2 having three 10% WT deep grooves and tube T3 having three 20% WT deep grooves. 106

Figure 4.15 As-received RFEC signals from tube T4 having 2 mm diameter hole and 1.15 mm deep circumferential notch in the bend region and the signals processed by the Fourier filtering, cross correlation and wavelet transform techniques. 107
Figure 4.16 Quantitative evaluation of thickness of grooves in straight and bend regions of SG tubes. 108
Figure 5.1 Photograph of the test vessel used to study the influence sodium deposits on SG tubes. 113
Figure 5.2 Photograph of the flange after sodium exposure and removal from the vessel. 114
Figure 5.3 RFEC signals of 3 mm width grooves of different depths, before and after sodium exposure. 115
Figure 5.4 RFEC signals of 2 mm width grooves of different depths, before and after sodium exposure. 115
Figure 5.5 Measured RFEC signal with and witout sodium deposits in 20% WT groove of 3 mm and derived signal parameters used. 117
Figure 5.6 Valley depth (H) for 3 and 2 mm width grooves of different wall loss. 118
Figure 5.7 The measured peak-to-peak amplitude (A) for different wall loss defects (width 3 mm) before and after sodium exposure. 119
Figure 5.8 The measured peak-to-peak amplitude (A) for different wall loss defects (width 2 mm) before and after sodium exposure. 120
Figure 5.9 Surface plots of the induced current density in the tube wall due to the exciter coil and a 50% wall loss groove and the groove filled with sodium. 121
Figure 5.10 Model predicted RFEC signals of grooves with and without sodium filling. 122
Figure 5.11 The model predicted peak-to-peak amplitude (A) for different wall loss defects (width 3 mm) with and without sodium filling. 122
Figure 5.12 Drawing of the tube support strip and photograph of the tube bundle. 123
Figure 5.13 Schematic of the architecture of linear kernel transform. 126

Figure 5.14 Model predicted RFEC signals of wall thinning grooves in the presence of support structure at different frequencies. 127
Figure 5.15 Results of Mix-1 (825 & 725 Hz) for different wall thinning grooves. 128
Figure 5.16 Results of Mix-2 (825 & 625 Hz) for different wall thinning grooves. 129
Figure 5.17 Schematic of the CASE-I and CASE-II defects under support structures. 130
Figure 5.18 Raw and mixed RFEC signals of a 20% WT groove partly outside the support structure (CASE-I). 131
Figure 5.19 Raw and mixed RFEC signals of a 20% WT groove off-centred with the support structure (CASE-II). 132

LIST OF TABLES

Table No.	Captions	Page No.
Table 1.1	Operating parameters of the PFBR steam generator.	3
Table 1.2	Comparison of electromagnetic nondestructive evaluation techniques.	21
Table 3.1	Dimensions and material properties used in the finite element model.	58
Table 3.2	The solution time and the vector potential values for different number of mesh elements	60
Table 3.3	Calculated A and B points as in Figure 3.8 at different frequencies for characterization of RFEC region.	68
Table 3.4	Design parameters of the RFEC probe.	76
Table 3.5	Comparsion linear and nonlinear model predicted RFEC amplitudes of a 20% WT deep groove.	84
Table 4.1	Details of the artificial defects made in the bend regions of the SG tube	97
Table 4.2	Signal, noise and SNR of the tubes T2 and T3 in as received condition.	98
Table 4.3	Signal, noise and SNR of the tubes T2 and T3 before and after Fourier filtering	101
Table 4.4	Signal, noise and SNR of the tubes T2 and T3 before and after the application of cross correlation.	103
Table 4.5	Comparative performance of various mother wavelets for RFEC signals from tube T2 having three 10% WT deep grooves.	105
Table 4.6	Signal, noise and SNR of the tubes T2 and T3 before and after CWT processing.	105
Table 5.1	Dimensions of grooves machined in steam generator tubes	112
Table 5.2	Similarity metric to assess the performance of the Mix-1 and Mix-2.	130

NOMENCLATURE

List of Symbols

σ	Electrical Conductivity
δ	Standard Depth of Penetration
μ	Magnetic Permeability
μ_r	Relative Magnetic Permeability
Ω	Ohm
1D, 2D and 3D	One Dimension, Two Dimension and Three Dimension
A	Magnetic Vector Potential
A_r, A_ϕ, A_z	Radial, Azimuthal and Axial Components of the Magnetic Vector Potential respectively
B	Magnetic Flux Density
B_r, B_z	Radial and Axial Components of the Magnetic Flux Density
°C	Degree Centigrade or Celsius
dB	Decibels
E	Electric Field
H	Magnetic Field Intensity
Hz	Hertz
J	Current Density
K	Kelvin
kHz	Kilo Hertz
MHz	Mega Hertz
mHz	milli Hertz
mm	millimeter
S/m	Siemens per Meter
V	Electric Scalar Potential or Volts
mV	milli Volts

List of abbreviations

ACPD	Alternating Current Potential Drop
A/D	Analog to Digital
AISI	American Iron and Steel Institute
ASME	American Society for Mechanical Engineers
BCG	Biconjugate Gradient
Bior	Bi-Orthogonal
CAD	Computer Aided Design
CWT	Continuous Wavelet Transform
DAQ	Data Acquisition
DB	Daubechies
DCPD	Direct Current Potential Drop
EC	Eddy Current
EDM	Electric Discharge Machining
FBH	Flat Bottom Hole
FE	Finite Element
FFT	Fast Fourier Transform
GUI	Graphical User Interface
Gaus2	Second Order Derivate of Gaussian Function
IACS	International Annealed Copper Standard
ID	Internal Diameter
IHX	Intermediate Heat Exchanger
ISI	In-Service Inspection
LKT	Linear Kernel Transform
MBE	Magnetic Barkhausen Emission
Mexh	Mexican Hat
MFL	Magnetic Flux Leakage
NDE	Non-Destructive Evaluation
NDT	Non-Destructive Testing
OD	Outer Diameter
PC	Personal Computer
PD	Potential Drop
PFBR	Prototype Fast Breeder Reactor

PIG	Pipe Inspection Gauge
PLL	Phase Locked Loop
RFEC	Remote Field Eddy Current
SCC	Stress Corrosion Cracking
SG	Steam Generator
SNR	Signal-to-Noise Ratio
SQUID	Super Conducting Quantum Interface Device
SSOR	Symmetric Successive Over Relaxation
THD	Total Harmonic Distortion
WT	Wall Thickness

Chapter 1: Introduction

1.1 Components of fast breeder reactor

The fast reactor program in India is an important phase, enabling the closing of fuel cycle by utilizing the large thorium reserves of the country, and thus providing energy security to the nation. The Prototype Fast Breeder Reactor (PFBR) is a first of its kind breeder reactor in India which is in advanced stage of construction [1]. Figure 1.1 shows the key structural components and the flow sheet of the PFBR. It is a pool type reactor and uses sodium as the coolant. The main structural components of the reactor such as active core, core-support structure, primary sodium pump and intermediate heat exchangers (IHX) are immersed in sodium in the main vessel of the reactor. The IHXs transfer primary sodium heat to secondary sodium. The secondary sodium exchanges the heat with water in the steam generator (SG) to produce supersaturated steam, which, in turn, is used to run the turbine to generate electricity. The core structural materials operate under radioactive, high temperature, pressure, and sodium environment. As a result, progressive damage of these components takes place. Such damage should be closely monitored and assessed to ensure the safe and reliable operation of the nuclear reactor.

1.2 Steam generators of PFBR

The steam generators of PFBR are one of most critical components, as sodium and water coexist in the system [2]. The very high reactivity of sodium with water makes the SG a key component in determining the plant availability. This demands high level of structural integrity. The SGs in PFBR are vertical with a height of 26 m. They are countercurrent shell-and-tube type heat exchangers with sodium on the shell side

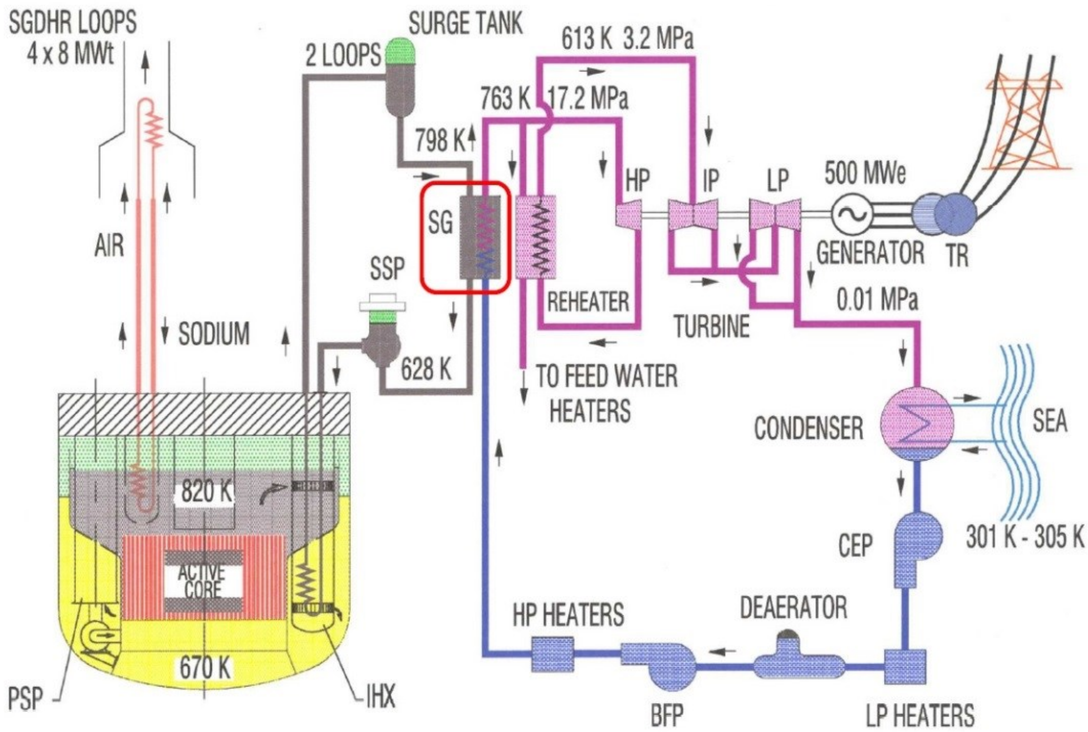

Figure 1.1 Components of the Prototype Fast Breeder Reactor.

flowing from top to bottom, and water/steam on the tube side flowing from bottom to top as depicted in Figure 1.2(a). Figure 1.2(b) and Figure 1.2 (c) show the internal views of the SG during fabrication at the shop floor. There are a total of eight SG's in the PFBR. Each SG has 557 number of seamless tubes of 17.2 mm OD, 2.3 mm wall thickness and 23 m in height, welded to top and bottom tube-sheets at the ends. Each tube has a thermal expansion bend of 375 mm radius (developed length 1,075 mm). Figure 1.2 also shows the SG tube bundle and the inner side of tube sheet joint. The SG tube bundles are supported at various locations including the expansion bend by structures made of Inconel 718. SG tubes separate sodium and water and prevents sodium-water chemical reaction and contamination. The operating temperature and pressure of the SG are as given in Table 1.1.

.

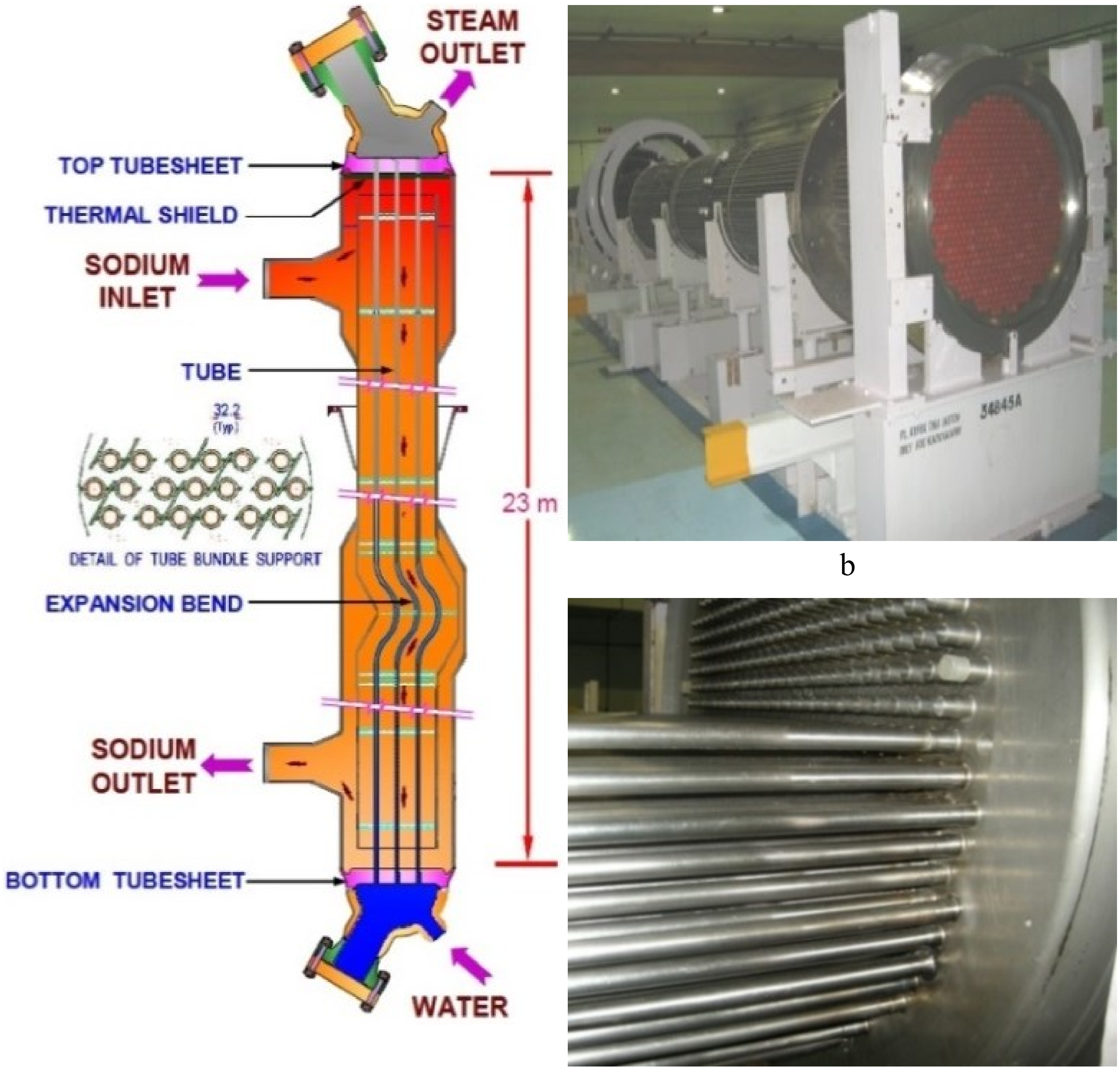

Figure 1.2 a) Schematic of the PFBR SG b) photograph of the SG tube sheet and c) tube bundle during fabrication stages in the shop floor.

Table 1.1 Operating parameters of the PFBR steam generator.

Process fluid	**Inlet temperature, K (°C)**	**Outlet temperature, K (°C)**	**Pressure, bar**
Sodium	798 (525)	628 (355)	0.8 (shell side)
Water	508 (235)	766 (493)	2.8 (tube side)

The safety and reliability of the SG have been ensured right from the material selection. Selection of material for the SG has to be based on the following important considerations [3]:

- Effect of creep and low cycle fatigue on the high temperature mechanical properties
- Resistance to loss of carbon to liquid sodium which leads to reduction in strength
- Resistance to stress corrosion cracking in sodium and water media
- Weldability, workability and cost

Cr-Mo ferritic steels (2.25Cr-1Mo, Nb stabilized 2.25Cr-1Mo, 9Cr-1Mo, modified 9Cr-1Mo), austenitic stainless steels (AISI 304/316/321) and alloy 800 are some of the candidate materials for the SG [3]. In view of the inferior resistance to aqueous stress corrosion cracking (SCC), austenitic stainless steels of 300 series are not preferred. Alloy 800 shows better resistance to SCC than austenitic steels, but it is prone to SCC in chloride and caustic environments. Therefore, ferritic steels are preferred for SG. Among the ferritic steels, 2.25Cr-1Mo and 9Cr-1Mo steels and their variants offer better mechanical properties. 9Cr-1Mo shows much better mechanical properties with the addition of stabilizing elements like Vanadium and Niobium that enhance the creep and fatigue resistance. This modified 9Cr-1Mo steel (Grade 91 or T91 steel) exhibits higher creep strength and enables use of comparatively thinner SG tubes. International experience also favors the use of this steel [4]. Hence, modified 9Cr-1Mo has been chosen as the structural material for the SG of PFBR.

During the reactor operation, SG tubes are subjected to hostile conditions such as high temperature, pressure and corrosive environment. As a result, progressive damage of the SG tubes takes place. Fouling, SCC, fretting and crevice corrosion are some of the life limiting factors of the SG tubes. If there is failure in the SG tube then sodium would come in contact with water and the following reaction would occur:

$$2Na+H_2O \rightarrow 2NaOH+H_2 \quad ...\ 1.1$$

$$2NaOH+Na \rightarrow Na_2O+H_2 \quad ...\ 1.2$$

The evolved hydrogen in reaction (1.1) is absorbed by sodium and the product further reacts with excess sodium as given in (1.2) [5]. Sodium water reaction is exothermic. Further, defects of any size producing a minimum steam leak rate of 100 mg/s would result in high pressure water jetting into the sodium, leading to the cascading failure of the adjacent tubes by the combined action of corrosion and erosion known as impingement wastage [6]. Figure 1.3 shows the impingement wastage (depth ~ 2 mm) occurred in a SG tube, when controlled experiments were performed in a sodium test facility to assess the impingement wastage resistant of modified 9Cr-1Mo SG tubes. A steam leak was experimentally simulated, through a 0.1 mm diameter hole in one SG tube. Thus, failure of a SG tube would result in catastrophic failure of whole SG. Hence, it is essential to ensure the health of the SG tubes. Nondestructive testing and evaluation plays a vital role in ensuring the structural integrity of the SG tubes through periodic in-service inspection (ISI).

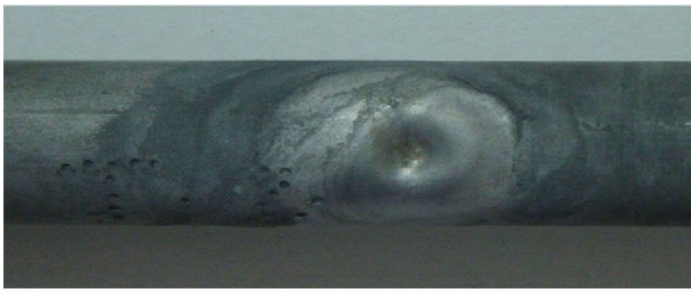

Figure 1.3 Impingement wastage on SG tube during controlled experiments [6].

1.3 Introduction to nondestructive evaluation

Nondestructive testing (NDT) is an interdisciplinary science that deals with the assessment of soundness and integrity of a component or structure through detection of discontinuities as well as defects without causing any damage to it [7,8]. The traditional NDT domain has transformed into nondestructive evaluation (NDE) with the added capability of quantitative characterization of defects. NDE is routinely used in nuclear power plants, transportation, aerospace, petrochemical and other industries to ensure quality, reliability, structural integrity and safety of critical components such as heat exchangers, railroads, aircraft engines, gas pipelines etc., whose failures can affect the plant availability, productivity and profitability [8,9]. The terms discontinuities and defects are often used in NDE. Discontinuities are any local variation in material continuity including change in geometry (such as holes, cavities), structure, composition or properties. Any discontinuity either single or multiple that creates a substantial chance of material failure in service, is commonly called a “defect”. Finding defects is one of the most frequent objectives of NDT. It must be understood, however, that a defect under one set of conditions may be only a simple discontinuity that is not harmful in a different application. Defects could be formed in a material or component during the manufacturing process (process induced defects) such as casting, welding rolling, forging and machining and also during service life (service induced defects) like creep damage, fatigue damage, embrittlement and corrosion.

A generic NDE system is shown in Figure 1.4. In this, the excitation transducer couples the energy source into the test specimen. The receiving sensor, placed on the same or opposite side of the specimen picks up the response of the field/flaw interaction and generates an output signal. The output signal is then processed, and passed through an inversion scheme that performs defect characterization, *i.e.* estimation of defect dimensions, location, and shape.

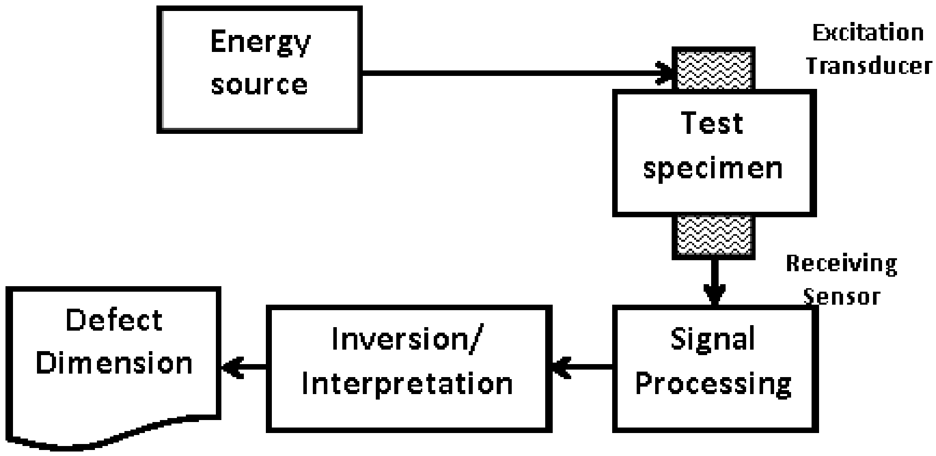

Figure 1.4 Schematic of a generic NDE system.

There are nearly 50 different NDE techniques in use today and nearly every form of energy has been used as basis for NDE measurements. Ultrasonic, radiography, eddy current, magnetic, penetrant, infrared thermography and acoustic emission techniques are popularly used in engineering industry. The measurements made in NDE techniques are relative and not absolute. As a result, calibration or reference standards consisting of artificial defects are used for comparison and interpretation of the measured data [10]. Calibration standards are made from specimen having identical dimensions, material properties and ageing conditions as that of the component being inspected. Flat bottom hole and notch type of artificial defects of different dimensions are often used to represent the real-world volumetric and linear defects, for calibration of instruments and for defect sizing. Electric discharge machining (EDM) is used for fabrication of these artificial defects. As NDE sensor response is influenced by disturbing noise due to material property variation and other electronic sources, expertise is essential for interpretation of the NDE results and for decision on acceptance/rejection of a component. Hence, training and certification of the personal performing NDE is an important requirement. There are a number of standards such as ASME, ASTM, RCCMR, BS and BIS, which provide the standard guidelines for preparing test procedure, performing inspection and training and certification requirements.

1.4 Electromagnetic nondestructive evaluation techniques

Among the host of NDE techniques, the electromagnetic NDE (ENDE) techniques are widely used for testing thin (thickness < 5 mm) and electrically conducting materials. They consist of eddy current (EC), magnetic flux leakage (MFL), magnetic Barkhausen emission (MBE) and potential drop (PD) techniques. The ENDE techniques use static (steady state) and low frequency (diffusive) electromagnetic fields to interrogate the material. They use both coils and solid state sensors to detect the manifestations. Thus, the ENDE techniques differ in their characteristics, primarily based on the frequency of excitation.

1.4.1 Eddy current technique

Eddy current technique is a popular and widely used ENDE technique for detection of defects in thin metallic materials. EC technique works on the principle of electromagnetic induction [11,12]. In this technique, changes in impedance of a coil excited with sinusoidal current, is measured upon placing the coil over an electrically conducting material. The primary magnetic field setup by the coil induces eddy currents in the material as shown in Figure 1.5, which in turn, generates secondary magnetic fields. According to the Lenz's law, the secondary magnetic field opposes the primary magnetic field of the coil. The net change in the flux linking the coil results in the reduction of the coil voltage. Eddy currents in the materials are perturbed as shown in Figure 1.5 by the presence of discontinuities and defects which, results in, the change in the secondary magnetic field and the voltage of the excitation coil. When the coil is fed with constant current, this voltage change across the coil would also manifest as change in the impedance of the coil, according to the Ohm's law. The impedance is a complex quantity with resistance (real) and inductive reactance (imaginary) components. The impedance changes for defect-free and defective regions are different and this enables one to detect the presence of a defect.

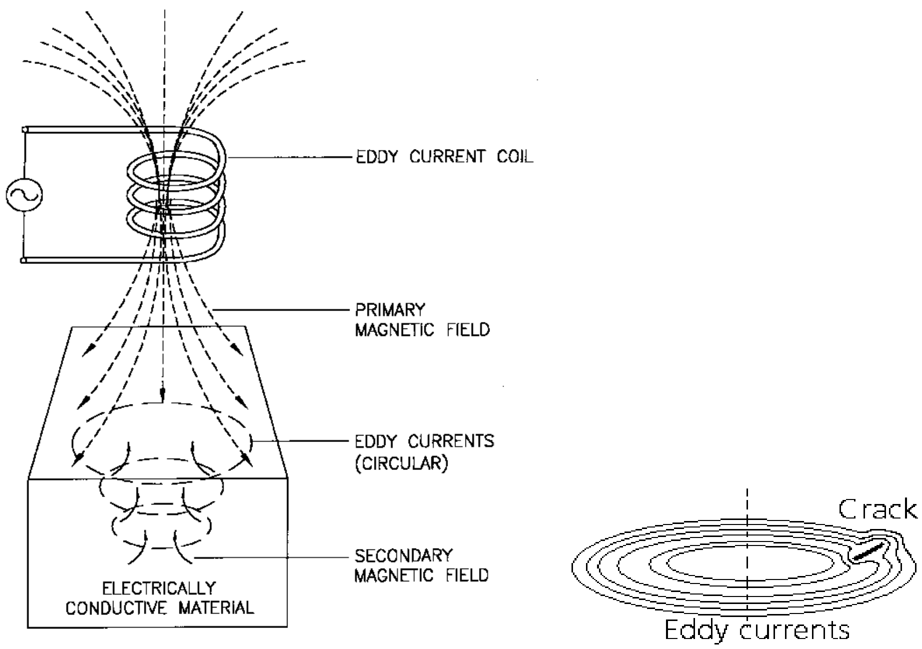

Figure 1.5 Schematic of the eddy current technique and distortion of eddy currents [12].

The amplitude and phase characteristics of the eddy current sinusoids in the test material can be obtained by solving the governing differential equation. The governing differential equation for coil excited with current density J and producing eddy currents in an isotropic homogeneous electrically conducting material is derived from the Maxwell's curl equations as [13].

$$\nabla \times \boldsymbol{E} = -\frac{dB}{dt} \qquad \text{... 1.3}$$

$$\nabla \times \boldsymbol{B} = \mu \boldsymbol{J} \qquad \text{... 1.4}$$

where $\boldsymbol{E}$ is the electric field, $\boldsymbol{B}$ is the magnetic field vector, $\boldsymbol{J}$ is the current density and μ is the magnetic permeability. Taking the curl of equation (1.3) and substituting (1.4) in the resulting equation, we obtain

$$\nabla \times \nabla \times \boldsymbol{E} = -\frac{d}{dt}[\nabla \times \boldsymbol{B}] \qquad \text{... 1.5}$$

$$\nabla \times \nabla \times \boldsymbol{E} = -\mu \frac{d\boldsymbol{J}}{dt} \qquad \text{... 1.6}$$

For sinusoidal excitation with frequency, f a time dependence of $e^{-j\omega t}$ can be assumed where $\omega=2\pi f$, and also using the constitute relation $J=\sigma E$, equation (1.6) can be written as

$$\nabla^2 \mathbf{J} = j\omega\mu\sigma\mathbf{J} \qquad \text{... 1.7}$$

where $j=\sqrt{-1}$. Solution to differential equation (1.7) in a one dimension along the thickness of the test object yields [15]:

$$\boldsymbol{J_z} = \boldsymbol{J_0} e^{-\{-z\sqrt{\pi f \mu \sigma}\}} \sin(\omega t - \beta) \qquad \text{... 1.8}$$

and $\beta = \sqrt{\pi f \mu \sigma}$

where J_z is the current density anywhere along the thickness of the material (z-axis) and J_0 is the current density at the surface of the material.

The solution to equation (1.8) contains the amplitude and phase terms depicting the nature of the eddy currents induced in the material by the excitation coil. The amplitude term describes the exponential attenuation of the eddy currents along the thickness of the material. The phase term β implies the linear variation of the phase of the eddy current sinusoids with thickness. The depths at which the current density falls to *1/e* times the surface current density in a material is called standard depth of penetration denoted as δ [13]:

$$\delta = \frac{1}{\sqrt{\pi f \mu \sigma}} \qquad \text{... 1.9}$$

where δ is called the standard depth of penetration, f is excitation frequency, μ is magnetic permeability and σ is electrical conductivity. As can be seen, the standard depth of penetration of eddy currents in the test object decreases with increase in σ, μ and f.

1.4.1.1 Eddy current probes

Eddy current probes are operated in absolute (single coil), differential (two coils wound in opposition) and send-receive (separate coils for excitation and detection) modes [14]. Their design is dependent on the object geometry viz. tube, plate, bar etc. as shown in Figure 1.6 and also on the expected type as well as location of the defect. Absolute probes are good for detection of cracks (long or short) as well as gradual variations. However, absolute probes are sensitive also to lift-off, probe tilt, temperature changes etc. Differential probes have two sensing coils wound in opposite direction, investigating two different regions of the material. They are good for high sensitive detection of small defects. They are reasonably immune to changes in temperature and the operator-induced probe wobble [15] . While pancake or surface probes are used for testing plates and regular geometries, encircling or bobbin type probes are employed for testing tubes, rods, and other cylindrical objects

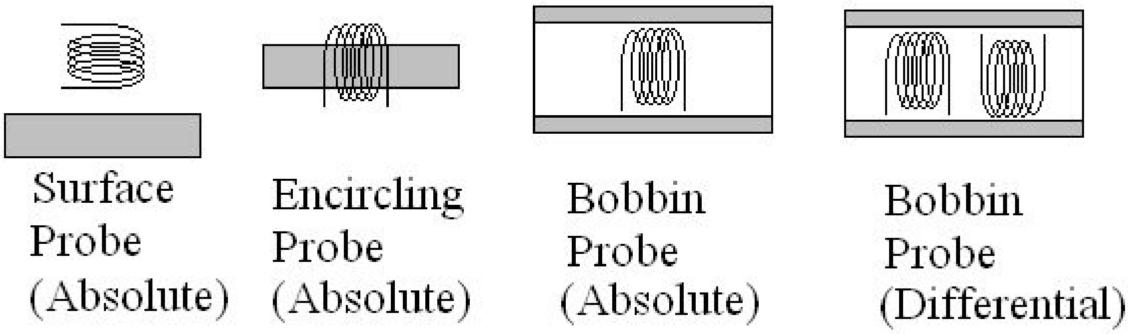

Figure 1.6 Type of eddy current probes used for different geometries [14].

The most simple and widely used probe types are:

- Surface or pancake or pencil probes (with the probe axis normal to the surface), are chosen for testing plates and bolt-holes, either as a single sensing element or an array - in both absolute and differential (split-D) modes.
- Encircling probes for inspection of rods, bars and tubes with outside access and
- Bobbin probes for pre-and in-service inspection of heat exchanger, steam generator and condenser tubes with inside access. Phased array receivers also possible for enhanced detection, imaging and sizing.

EC probes possess directional properties *i.e.* regions of high and low sensitivity (impedance change). Defects that cause maximum perturbation to eddy currents are detected with high sensitivity *i.e.* defects that are perpendicular to eddy currents (Figure 1.5). For good sensitivity to small shallow defects, a small probe should be used. Similarly, in order to detect sub-surface and buried defects, large diameter high throughput probes operating at lower frequencies are necessary. As a general rule, the probe diameter should be less than or equal to the expected defect length and also comparable to the thickness of the test object. The sensing area of a probe is the physical diameter of the coil plus an extended area of 4δ due to the magnetic field spread [15]. Hence, it is common to use ferrite cores as well as shields with high μ and low σ, to contain the field without affecting the depth of penetration. Figure 1.7 shows some typical EC probes used for specific applications [15].

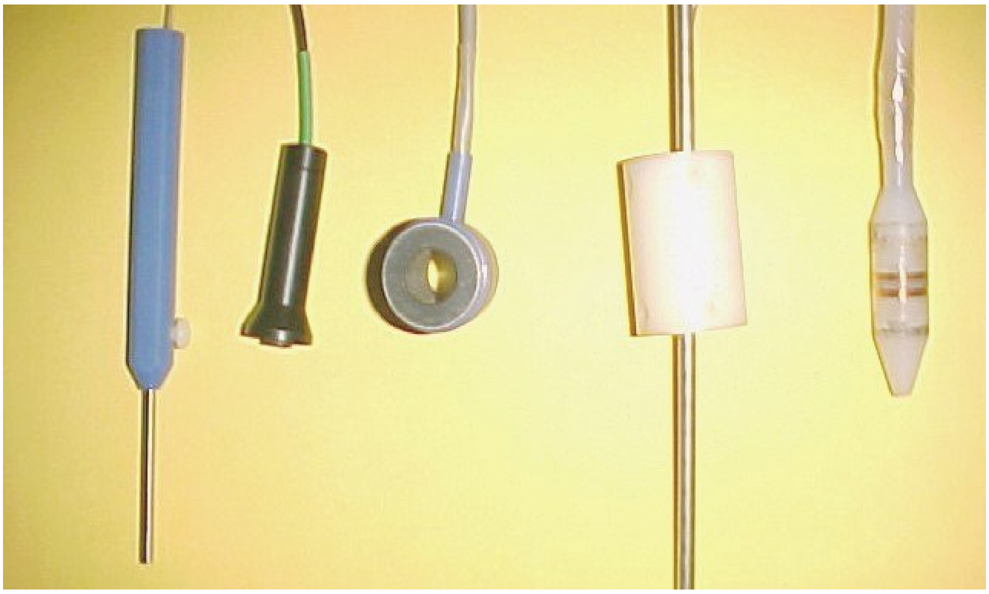

Figure 1.7 Typical EC probes (pencil, pancakde, ring, encircling and bobbin) used for specific applications [12].

Figure 1.8 shows the typical signals observed from reference defects (flat bottom holes of different depths expressed as percentage of wall thickness as mentioned in the figure) used for the inspection of heat exchanger tubes by ID bobbin type differential probe. The differential ID bobbin probe produce Lissajous type signals for defects present in the heat exchanger tubes [16].

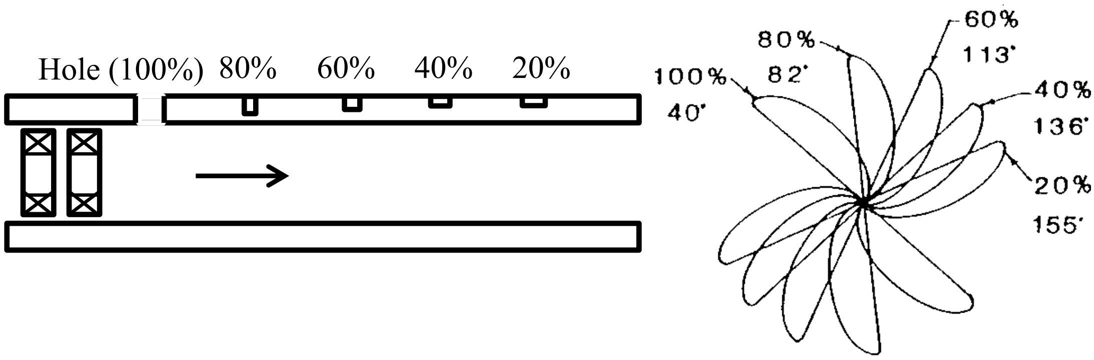

Figure 1.8 Typical eddy current signals of various defects in a tube obtained by bobbin type differential probe [14].

1.4.1.2 Eddy current instrument

In EC technique the alternating current through the coil is kept constant (~ few hundred mA) and the change in the coil impedance is measured. Since the impedance change is very small (< micro-ohms), high precision A.C. bridge circuits are employed. The bridge imbalance is correlated with the defect or material attribute responsible. Typical analogue EC instrument consists of an oscillator (excitation frequency, ~ 50 Hz-5 MHz), constant current supply (step down from 230 V AC), a bridge circuit, amplifier, filters, oscilloscope (to display the impedance changes in a 2-D graph or as a vector) or meter display unit or decision making unit.

With the micro-electronic revolution, digital EC instruments have replaced the analog EC instruments. These instruments are portable, high-sensitive, low-cost, automated, modular and efficient. They are, in many instances, interfaced to personal computers, industrial computers, and laptops with possibility for easy measurements, adjustments, controls, data storage, analysis and management, all performed by suitable software.

1.4.2 Magnetic flux leakage technique

In MFL technique, static magnetic fields are used to interrogate a ferromagnetic material. These fields are used to magnetize the materials close to magnetic saturation. When a defect is present in the material, the magnetic permeability is reduced at the defect region and this causes distortion of magnetic field lines around the defect and leakage of some of the magnetic fields out of the material as shown in

Figure 1.9. The success of MFL technique depends on proper magnetization of the object, detection of leakage flux using a suitable sensor, processing of raw data to enhance signal-to-noise ratio, and interpretation of the MFL signals. Permanent magnets, magnetic yokes, solenoid or Helmholtz type electromagnets and current carrying conductor are used to magnetically saturate the ferromagnetic material [17]. The leakage flux is measured using Hall and Giant Magneto Resistance (GMR) sensors.

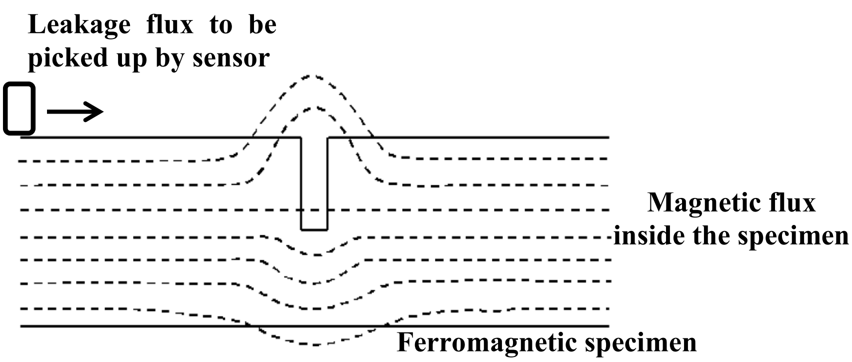

Figure 1.9 Principle of magnetic flux leakage technique [17].

MFL technique is widely used in industry for assessing the quality and structural integrity of underground oil and gas pipelines, oil-storage tank floors and wire ropes. MFL technique is commonly used for online detection of metal-loss and gouging in oil and gas transmission pipelines that run a few kilometers. Pipe Inspection Gauge (PIG) is commonly used for this purpose [18].

1.4.3 Magnetic Barkhausen emission technique

When a ferromagnetic material is subjected to a varying magnetic field, the magnetization occurs in discrete jumps as depicted in the zoom-in view of Figure 1.10 [19]. These discrete jumps induce voltage pulses in an inductively coupled pick-up coil placed over the material. This phenomenon is called Magnetic Barkhausen Emission and is attributed to the discrete jumps of domain walls overcoming obstacles. MBE technique is sensitive to microstructural variation and strain in the material while magnetizing the material using permanent or electromagnets. Figure 1.10 shows typical electrical signals associated with the Barkhausen jumps measured by the inductive coil. Features such as the peak amplitude and RMS are measured from the signals and correlated to the changes in the microstructure of the material [20]. This technique is mostly used for microstructural characterization rather than defects detection.

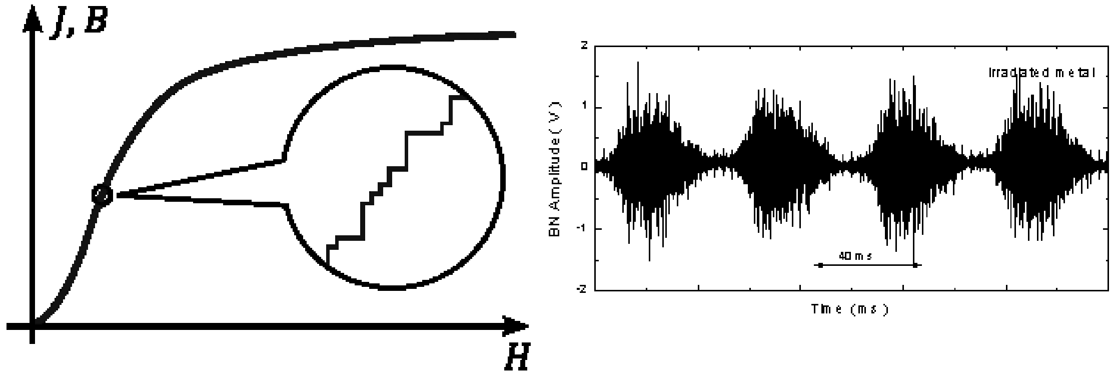

Figure 1.10 Discrete changes during the magnetization process and Barkhausen emissions observed in a ferromagnetic material [8].

The MBE technique has proved its viability as a potential electromagnetic NDE technique for the evaluation of residual stresses and microstructural changes. Many common surface treatments such as grinding, shot peening, carburizing and induction hardening results in the modification the stress state and microstructure of the material and hence can readily be detected using MBE technique. Dynamic processes like creep and fatigue which influence the stress and microstructure can also be detected and quantified with MBE. MBE technique is also used for characterization of contact fatigue damage in helical gears [21].

1.4.4 Potential drop technique

Direct current potential drop (DCPD) technique is one of the oldest NDE techniques [22]. In this technique, direct electrical currents are injected into a conducting specimen through one pair of electrodes, while a second pair of electrodes is placed across a crack or where crack initiation is expected as shown. Figure 1.11 shows the schematic arrangement of the electrodes across a crack in a conducting specimen. The injecting electrodes are positioned at a sufficient distance to ensure field uniformity in the inspection area. When the length or depth of a crack increases, the cross sectional area of the specimen is reduced. This causes an increase in resistance and also results in the increase in the potential difference measured between the electrodes positioned across the crack. The amplitude of the measured voltage depends on the conductivity, geometry of the specimen and also factors such as distance between the measuring electrodes, temperatures changes etc.

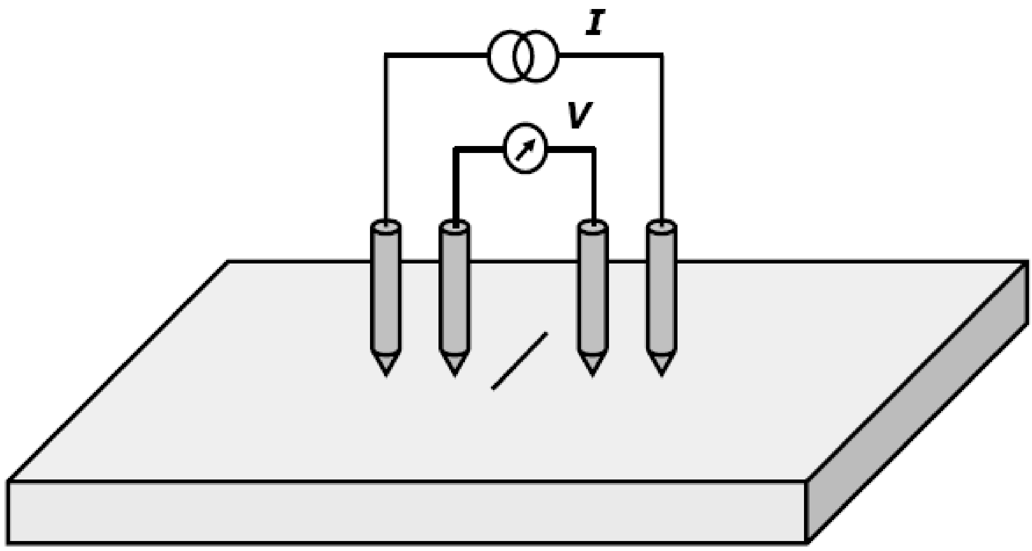

Figure 1.11 Principles of potential drop measurement technique [22].

The alternating current potential drop (ACPD) technique is similar to DCPD with the main difference being the use of alternating excitation current. The currents in the ACPD technique are forced to flow in a thin layer below the surface due to the *skin effect*. This results in smaller effective cross-section and hence, generates very high potential difference even for smaller currents. DCPD and ACPD techniques are used for the measurement of crack length and depth during fatigue testing of components. In general, these techniques can be applied in situations where the position or probable location of the crack is known *apriori*, by other NDE techniques.

1.4.5 Other ENDE techniques

There are several variants of each of the electromagnetic NDE techniques based on the type of excitation source. For example in EC technique, pulsed and sweep frequency excitations are used and are called pulsed and sweep frequency EC techniques respectively. MFL technique uses static, low frequency and pulsed excitations sources. The techniques also differ based on the type of receiving sensors. A variant of the potential drop technique called the alternating current field mapping which maps the field distribution when alternating current is passed into the material. High sensitive SQUID based sensors are also being used in EC technique for improved detection of subsurface defects [23]. A popular imaging technique which is primary based on the eddy currents, called magneto optic imaging (MOI) technique is also in use. In this technique, the perturbed eddy current fields in a material due to the presence of defects is mapped using magneto optic sensor. The magneto optic sensor works based on the Faraday rotation of the polarization of light. This technique is predominantly used in aircraft industry for detection of cracks and corrosion in riveted air frames [24]. Microwave imaging or ground penetrating radar technique is also an ENDE technique which uses electromagnetic waves in the GHz frequency regime. This technique is a time domain electromagnetic technique and applicable for testing dielectric materials. This technique is strikingly different in the above mentioned aspects, from the diffusive fields ENDE techniques. In this technique, microwaves propagating through a dielectric medium (e.g., concrete) are reflected when they encounter another medium having different dielectric properties such as rebars or voids. The reflection strength is based on the dielectric contrast between the host medium and the reflecting medium.

1.4.6 General characteristics of ENDE techniques

Due to *skin-effect*, most of the ENDE techniques are applicable to thin metallic materials only. The sensors and transducer used in ENDE techniques also are highly directional, especially the solid state sensors are sensitive only to one component of the electromagnetic fields. The ENDE techniques are influenced by several physical variables such as conductivity, permeability, permittivity, excitation frequency etc. Deterministic modeling of the ENDE techniques is possible, which means the result of performing an ENDE technique can be predicted by analytical and numerical modeling by solving the governing partial differential equation (PDE). The governing PDE can be derived from the Maxwell's equations of electromagnetics explained in Section 1.4.1. ENDE techniques provide ample scope for application of signal and image processing methodologies. In most of the ENDE techniques, due to the diffusive nature of the EM fields, inversion is very much involved. Regularized optimization and machine learning strategies are applied, in general, for the inversion of the ENDE results [25,26]. Table 1.2 summarizes the comparative capabilities of various electromagnetic NDE techniques. These techniques are mostly non-contact techniques. Electromagnetic techniques are sensitive to changes in the electrical conductivity and magnetic permeability of the material being tested and are also sensitive to microstructural changes [27]. ENDE techniques are also applied for characterization of coating thickness, sorting of materials, conductivity measurements, sizing of cracks and characterization of microstructures [28,29].

Table 1.2 Comparison of electromagnetic nondestructive evaluation techniques.

Technique	Frequency range	Physical variable	Materials applicable	Sensor employed	Detection capability
EC	5-5000 kHz	electrical conductivity, magnetic permeability	Conducting materials	Inductive coils, Hall, GMR and GMI, SQUID	Surface & Subsurface (< 5mm)
MFL	Steady state, 10 -100 Hz	magnetic permeability	Ferromagnetic materials	Hall, GMR	Surface & Subsurface (< 5mm)
MBE	50-250 kHz.	Metallurgical conditions, stresses	Ferromagnetic materials	Inductive coils	Surface & Subsurface (<3 mm)
Potential drop	Steady state, Low frequency	Conductivity	Conducting materials	Voltage measuring devices	Only sizing

1.5 State of the art ENDE of tubes

1.5.1 Testing of non-ferromagnetic tubes

EC technique is used for testing plates and tubes in production stages as well as during service. This technique is the most preferred one for testing nonmagnetic (μ_r=1) heat exchanger tube. EC testing of heat exchanger tubes is carried out using bobbin type differential probes. Figure 1.12 shows typical tube sheet arrangement and differential bobbin probes used. ASME, Section 5, Article 8 provides the standard guidelines for EC examination of non-ferromagnetic heat exchanger tubing [30]. It recommends the use of a calibration standard consisting of flat bottom holes of different depths. The measured phase angle of EC signal from the calibration defects is used for sizing of defects. An appropriate excitation frequency is chosen by the inspector for testing of the tubes, such that one standard depth of penetration of eddy current in the material is achieved and the phase angle separation between the calibration defects is maximized.

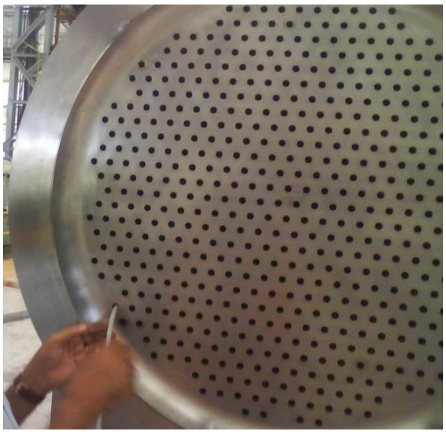

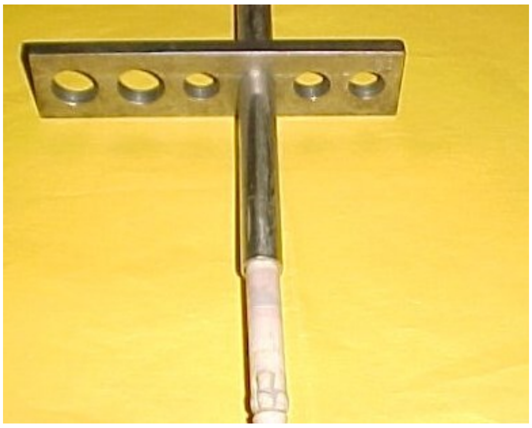

Figure 1.12 Typical tube sheet and differential bobbin probes used for EC testing.

Eddy current technique is a fast and reliable technique for inspection of heat exchanger tubes. Typical inspection speed in EC testing is 1 m/s (1000 mm/s), which is high as compared to other NDE techniques. There is no requirement of using coupling medium like the one used in ultrasonic technique. This technique will tolerate a lift-off up to 2 mm. This noncontact coupling of eddy currents enables testing at elevated higher temperatures.

1.5.1.1 Rotating probe/tube technique

Conventional bobbin type EC probes detect defects that are oriented in the axial direction. Circumferentially oriented cracks offer less perturbation to the eddy currents and hence, the detection sensitivity for such cracks is less. To overcome this, the use of the localized differential probes was reported [31]. For enabling 100% volumetric inspection of the tubes and viewing the projected C-Scan data of the tube wall, such localized probes should be rotated circumferentially inside the tube while simultaneously scanning in the axial direction, resulting in a helical scanning of the tube wall. The inspection time involved in such circumferential scanning is further be reduced by the use of circumferentially arranged multiple pancake type probes (array probes). The data from each individual probe is acquired simultaneously or by electronic multiplexing [32]. The array probes operate in send-receive mode for detection of defects oriented in all possible directions. Thus, the eddy current technology has been well established for inspection of nonmagnetic SG tubes.

1.5.2 Testing of ferromagnetic tubes

Inspection of ferromagnetic SG tubes by conventional EC testing is different from the nonmagnetic tube inspection due to the nonlinear magnetic permeability variations and reduced skin depth [33]. The depth of penetration of eddy currents in ferromagnetic materials is lower as compared to nonmagnetic materials due to higher permeability. It is possible to reduce the excitation frequency to achieve higher depth of penetration in ferromagnetic materials. However, this results in the reduction of detection sensitivity for defects, due to the large volume of interrogation of the material and small induced voltages or change in coil impedance. As a result, smaller defects may be missed [13]. Hence, conventional EC testing is not preferred for inspection of thick (>1.0 mm) ferromagnetic tubes.

When a ferromagnetic material is magnetized, the magnetic flux density in the material increases nonlinearly with the applied field and exhibits hysteresis. This phenomenon is popularly known as the BH characteristic. The sinusoidal excitation used in EC testing, is equivalent to magnetization and demagnetization. This would result in the formation of minor BH loops which would affect the impedance changes of the coil [33]. Thus, the nonlinear BH characteristics introduce high frequency noise during EC testing of ferromagnetic tubes. This noise sometimes masks the genuine signals from defects, resulting in poor signal-to-noise ratio (SNR) and leading to missing of potentially harmful defects.

DC saturation based EC testing is employed for ferromagnetic tubes, in which the tube material is magnetized to near saturation region such that the variations due to magnetic permeability are minimized. In such condition the material behaves like nonmagnetic and the disturbing noise due to permeability variations is absent. A solenoid magnetising coil concentrically embedded with an encircling differential eddy current probe is used for DC saturation EC testing. Subsequent to EC testing, the tubes are demagnetised in an AC solenoid coil to remove residual magnetism [33]. DC saturation using large size solenoid type magnetising coils can only be used with an encircling type EC probes. For large diameter (>40 mm) tubes having inside access bobbin type magnetising coils or strong permanent magnets are used for magnetising the tubes. However, there are difficulties in probe pushing and pulling due to these strong magnets sticking to the tube and also for demagnetisation of the tubes.

This thesis is concerned with the NDE of modified 9Cr-1Mo SG tubes of PFBR. The material is ferromagnetic in nature. In view of the limitations for using conventional EC techniques, it is important to develop appropriate techniques for the NDE of PFBR SG tubes.

Chapter 2: Motivation and objective

2.1 Introduction

This chapter presents the NDE practices during the quality assurance of PFBR SG tubes and reviews the need for the development of appropriate technique for ISI, towards identifying remote field eddy current (RFEC) technique. It then reviews the state of the art RFEC technique through comprehensive literature survey and explains the motivation for the development of RFEC technique for ISI of SG tubes.

2.2 NDE of PFBR steam generator tubes

2.2.1 NDE during manufacturing and quality assurance

The modified 9Cr-1Mo SG tubes are manufactured through a two-stage cold mill pilgering process. The produced tubes are approximately 25 m long with 17.2 mm outer diameter and nominal wall thickness of 2.3 mm, with a positive tolerance of 0.4 mm in wall thickness. Hence, during manufacturing, the average thickness is set around 2.5 mm while maintaining an OD of 17.2 mm. The produced tubes are subjected to 100% volumetric inspection by immersion ultrasonic and DC saturation EC techniques as per the RCCMR standard RMC 2000 and 6000 respectively [34]. Figure 2.1 shows the flow sheet followed for the quality control of SG tubes [35].

2.2.1.1 Saturation eddy current testing

Figure 2.2 shows the schematic of the setup used for the saturation EC testing of SG tubes [36]. A solenoid type magnetising coil carrying 3A of current, setup a magnetic field necessary to saturate the tube and a concentrically kept encircling differential probe operating at 25 kHz is used for detecting localised defects. A calibration tube consisting of three 1.2 mm diameter through holes at 120° apart, axially separated by 100 mm is used for ensuring sensitivity of the method. The tubes are passed through the magnetizing coil at a constant speed of 400 mm/sec and then demagnetised using AC solenoid coil. Figure 2.3 shows the typical EC signals without and with magnetic saturation of the modified 9Cr-1Mo SG tube. A three-fold increase in the SNR is observed after magnetisation of the SG tube.

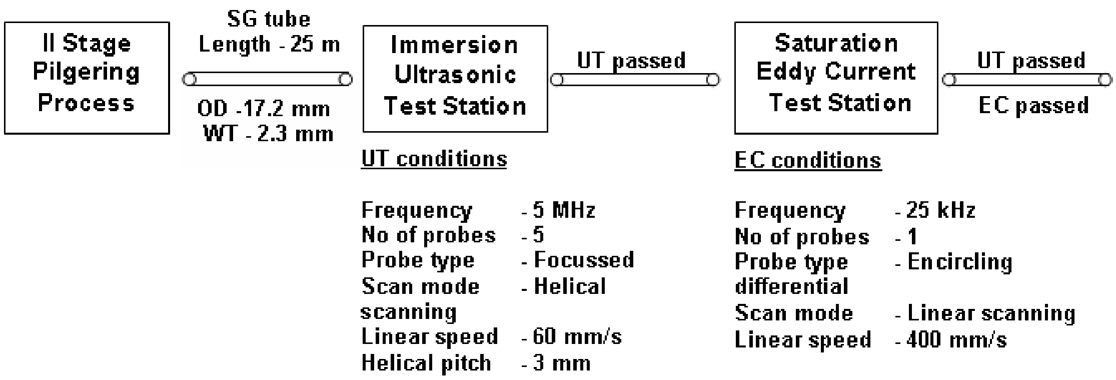

Figure 2.1 Flow sheet of the quality control of SG tubes [35].

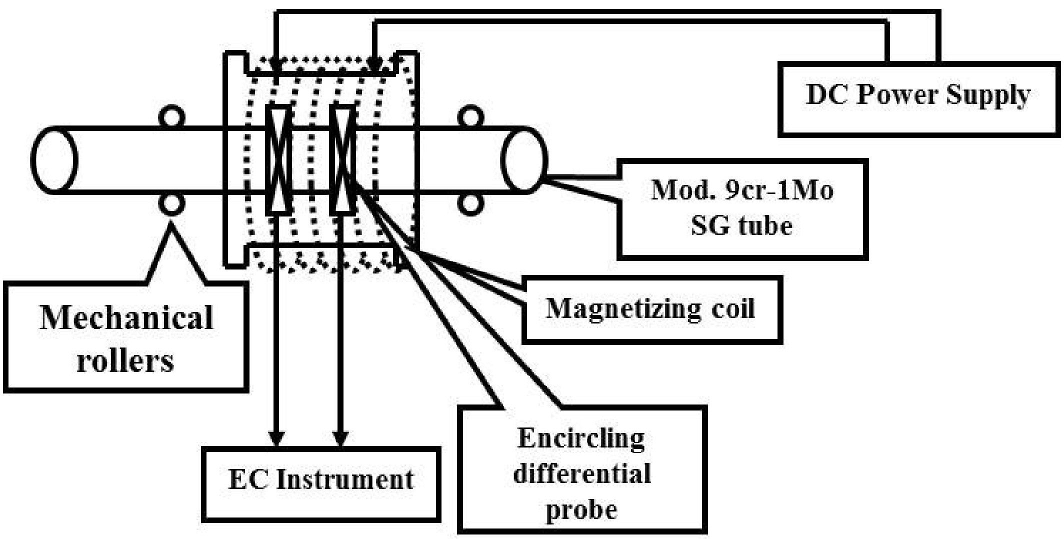

Figure 2.2 Saturation EC test setup for quality assurance of SG tubes [36].

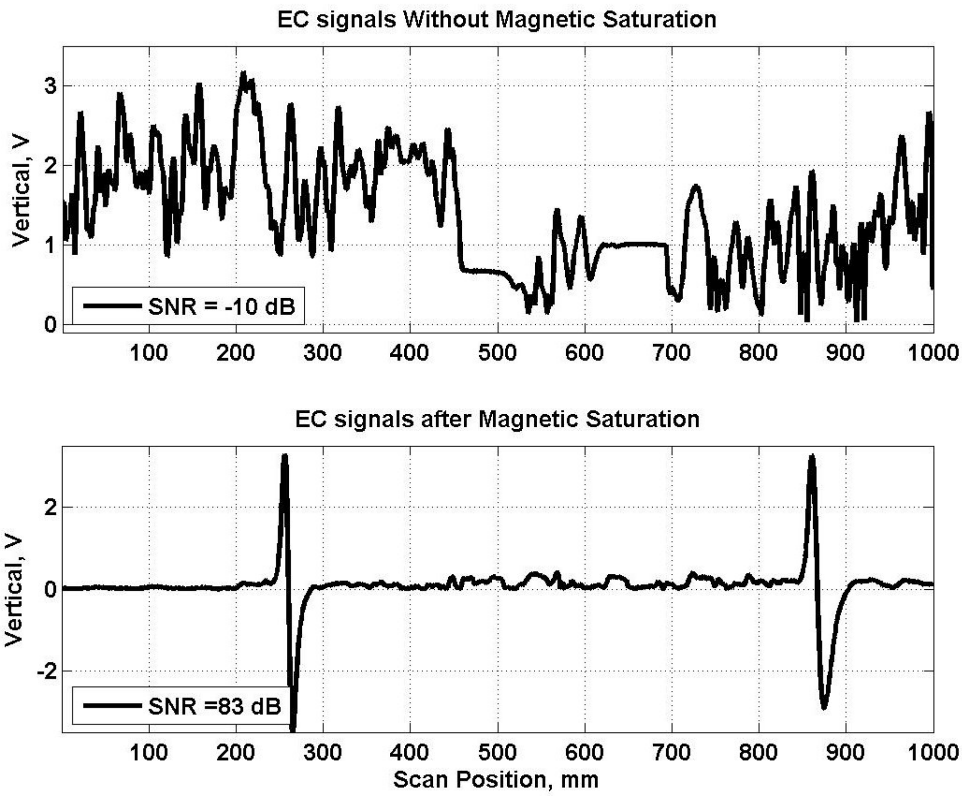

Figure 2.3 EC signals (vertical component) of the through holes of 1.2 mm diameter without and with magnetic saturation.

2.2.2 NDE of installed SG tubes for in-service inspection

Periodic ISI of SG tubes is essential for ensuring the structural integrity. The saturation EC technique used for the quality assurance of the SG tubes cannot be applied for installed SG tubes due to difficulty in magnetization and demagnetization (only small diameter coil can be used with less magnetizing current) that requires the use of large size coils. Immersion ultrasonic testing used during the quality assurance is also not applicable for ISI, as the transducers need to be rotated for full length testing and a coupling medium is required. Another promising NDE technique for ISI of SG tubes is the MFL technique. In this technique also, it is essential to magnetize the tube. But the recent study of the MFL technique using high sensitive GMR sensors shows that the magnetization level can be significantly reduced, for the measurement of leakage fields [17]. However, demagnetization of the tubes to the required level of residual magnetism (6 Gauss) in the tube is a concern. Remote field eddy current (RFEC) technique, a low frequency EC technique, which uses an exciter and receiver coil (send-receive) separated by a characteristic distance, is attractive for ISI of installed SG tubes. RFEC technique inherits many of the advantages of the conventional EC technique and is also free from constraints faced by the saturation EC, MFL and ultrasonic techniques. In view of the advantages, RFEC technique has been chosen for ISI of PFBR SG tubes.

2.3 Principle of remote field eddy current technique

The first known reference to the RFEC technique was the patent by McLean (1965) [37]. Later, researchers applied this technique for detection of external corrosion in oil-well casings and pipes [38,39]. These pipe diameters were in the range of 178-203 mm and thickness in the range of 9.5-12 mm. RFEC technique is mostly applicable to tubular components with ID bobbin type probe. However, with special type of exciter coil arrangement this technique could also be adopted for inspection of external tube wall and plates [40,41].

RFEC technique uses separate exciter and receiver coils that are kept inside the tube as schematically shown in Figure 2.4. The separation distance is usually 2 to 3 times the inner diameter of the tube [38]. Low frequency sinusoidal excitation in the range of 50 Hz to 5 kHz (depending on the skin depth) is applied to the exciter coil to generate time varying magnetic fields. The eddy currents induced in the tube wall, as a result, generate secondary magnetic fields. The primary field axially travel in the inner side of the wall and the secondary fields travel axially and radially in the tube wall. In such a situation, there exist two regions of importance:

i) The region inside the tube wall where the field due to the exciter coil decays exponentially along the axial direction, called the direct field region as shown in [42] and

ii) The region inside the tube wall where the concentrated flux in the tube wall enters back into the tube at a distance where the direct field component is less, is called the remote field region.

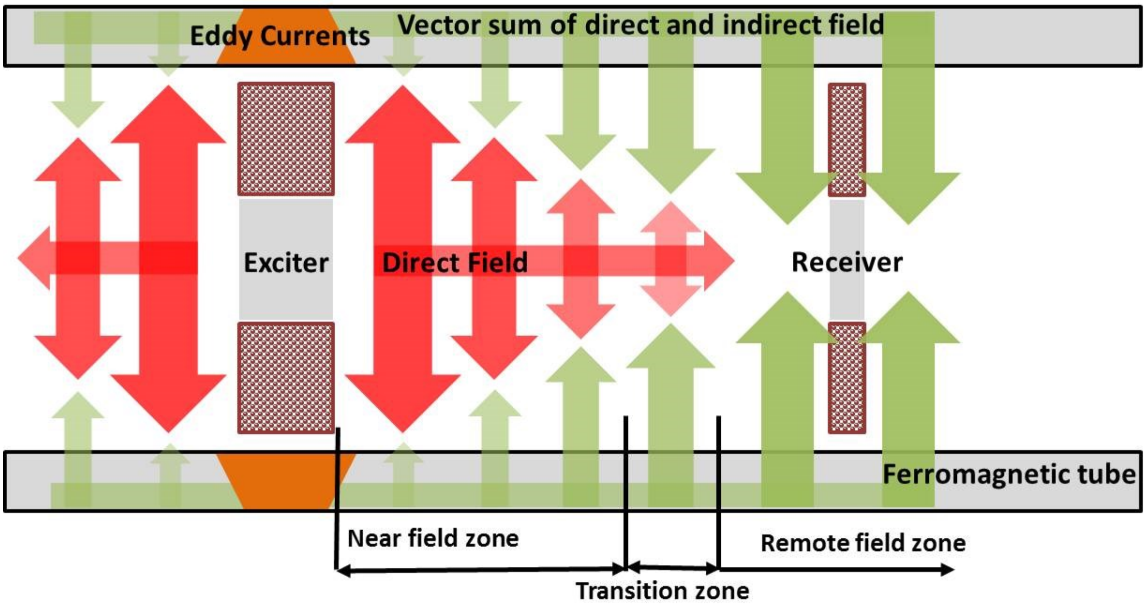

Figure 2.4 Principle of RFEC technique.

Close to the exciter coil the direct field dominates and far from the exciter, *i.e.* in the remote field zone the indirect field due to the eddy current in the tube is dominant. There is a transition region, in which both direct and indirect fields are significant and interact in a sometimes unexpected way [42]. The destructive interaction of the direct and indirect fields at the transition region results in an insignificant magnetic field in the region which is termed as amplitude or potential valley. There is an abrupt and unexpected variation in the phase angle of the magnetic field sinusoids in the transition region which is called the phase knot. Figure 2.5 shows the field log reported in [42], obtained by moving an ID coil in the axial direction from a fixed exciter located at zero on the plot. Close to the exciter the detector amplitude is very large and dominated by the direct coupling. It attenuates rapidly up to about 1.8 pipe diameters. A slope change is encountered beyond which the indirect coupled signal dominates in the remote field region.

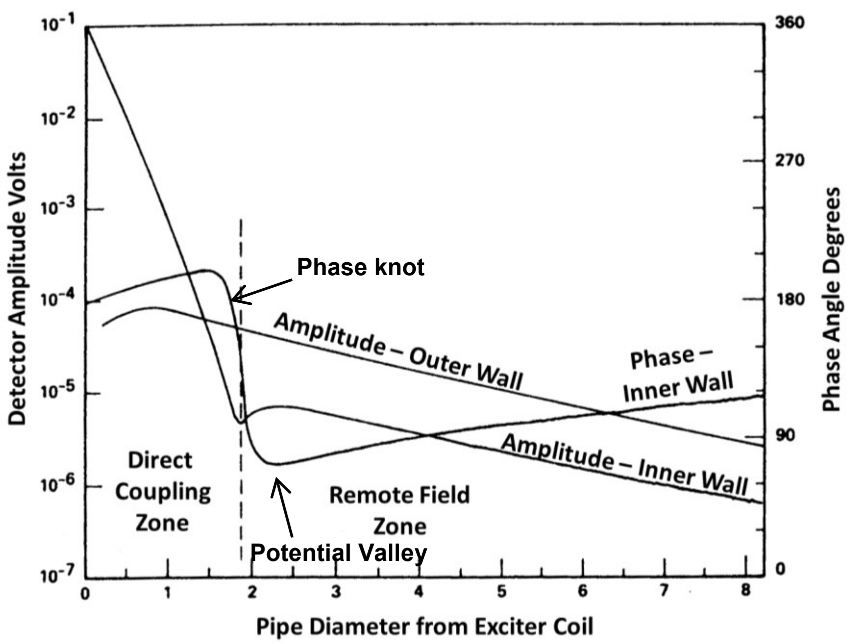

Figure 2.5 The field log for a moving ID receiver coil from an exciter coil [42]

Figure 2.6 shows the magnetic field inside the tube wall for a pipe outer diameter of 80 mm and thickness 6.5 mm [43]. The field line profile depicts two regions with totally different behaviors. In the vicinity of the exciter, the field lines are encircling the exciter coil (the direct field region), there is another area at a larger distance where the field lines are directed away from the exciter coil (remote field region). The sharp separation between these two regions is the characteristic of the transition region. Figure 2.6 also clearly depicts the phase knot and the potential valley.

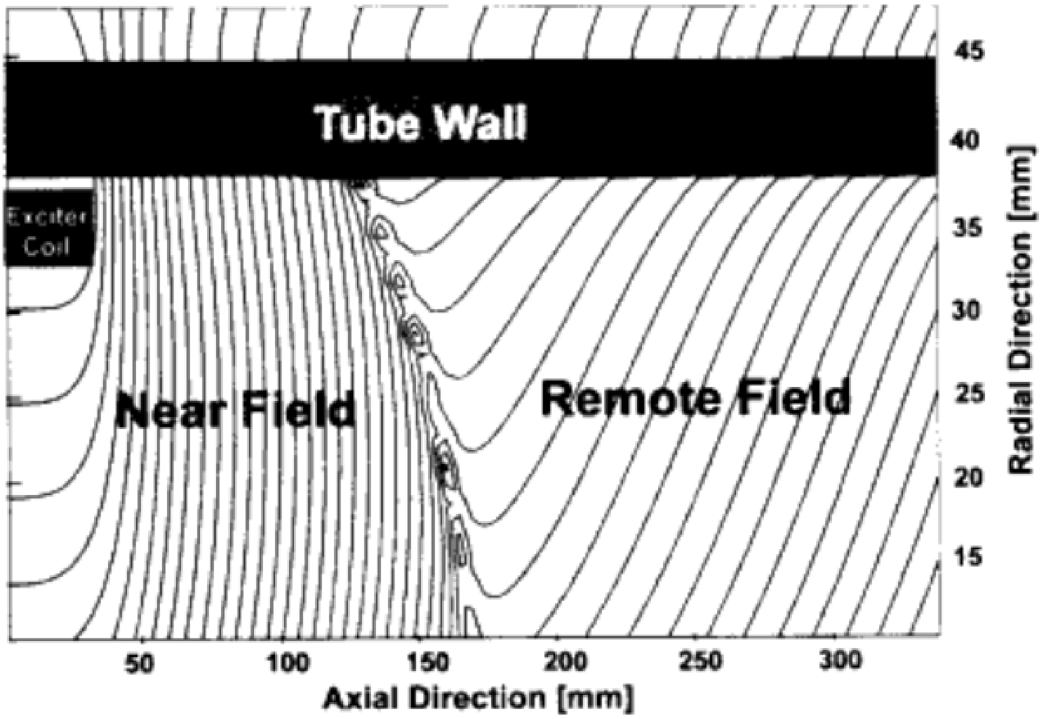

Figure 2.6 Magnetic field profile insider the ferromagnetic tube wall [43].

The magnetic flux in the remote field region is attenuated and lagged in phase. When a receiver coil is placed in the remote field region, the indirectly coupled magnetic flux induces a voltage which carries the information of the tube wall condition. The amplitude and phase lag of this induced voltage are measured and correlated to the wall loss or presence of defects [44], when the exciter and receiver coils are moved in tandem inside the tube or pipe. The amplitude or phase lag of the induced voltage during the coils' transit over a defect is called the RFEC signal. Figure 2.7 shows the typical RFEC amplitude signals of OD wall thinning grooves. As seen, the RFEC signals show characteristic double peaks, one when the defect is under the receiver coil and the other when the same defect is under the exciter coil.

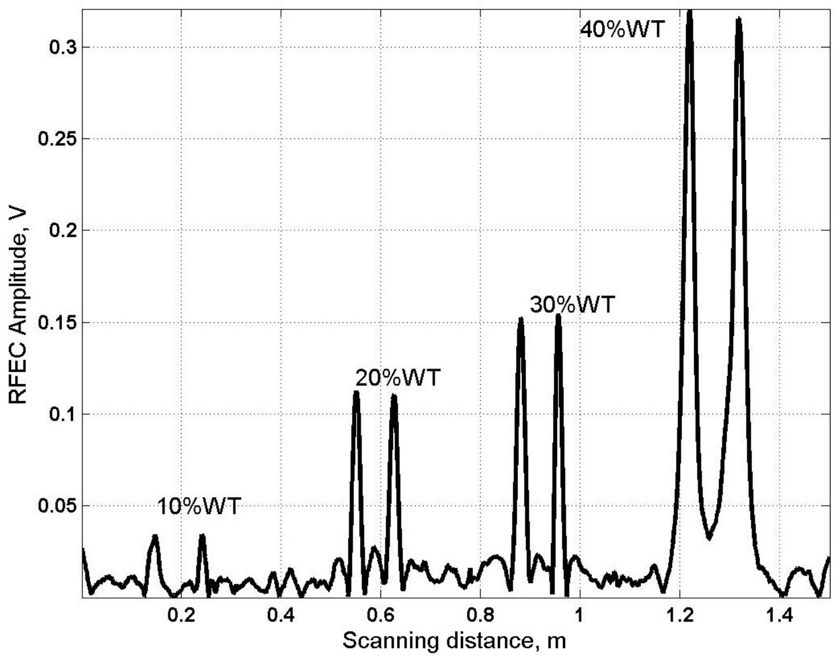

Figure 2.7 RFEC amplitude signals for uniform wall thinning grooves [45].

2.4 Important features of RFEC technique

RFEC technique offers several advantages for testing of ferromagnetic tubes including the following:

1) RFEC is a low frequency and through transmission technique. The effective length of the RFEC probe is approximately 2-3 times the diameter of the tube. As a result, the noise due to continuously varying permeability is averaged and minimised. Hence, it is not necessary to magnetize the tubes. Due to the through transmission nature of electromagnetic fields, it also offers equal sensitivity to ID and OD defects.
2) Due to minimal permeability noise, the RFEC technique offers higher sensitivity as compared to conventional EC testing at similar operating frequencies and is less prone to lift-off variations [46].

3) The phase velocity of the electromagnetic waves travelling in the tube wall is a linear function of the distance. Hence, the measured phase lag between the exciter and receiver coil voltages in RFEC technique has a linear relationship with wall thickness [46].
4) Inspection speed of up to 300 mm/s in the RFEC technique is reported in the literature, which is high as compared to ultrasonic rotating mirror inspection technique which has a maximum inspection speed of 100 mm/s [47].
5) The signal interpretation and analysis methodologies used in the conventional EC testing, can readily be used in RFEC testing also. RFEC signals can be analyzed in impedance plane as it is done for the conventional eddy current signals. Other forms of representation such as polar plots and amplitude and phase angle based analysis used in conventional eddy current technique is also applicable for RFEC signals [11].
6) RFEC technique is efficient in detecting wall thinning defects such as corrosion and erosion. The technique is capable of detecting linear defects such as cracks and volumetric defects such as pitting, fouling and impingement wastage [6]. The technique can also be used for detection of defects near tube supports and tube sheet [48].

2.5 State of the art of RFEC technique

Application of the RFEC technique for ISI of SG tubes is challenging especially in small diameter tubes such as the PFBR SG tubes (17.2 mm outer diameter and 2.5 mm thick). This involves the optimization of the RFEC probe, instrumentation and addressing the site related inspection issues such as detection of defects in bend regions of the SG tubes, in the presence of sodium, and under support structures.

2.5.1 RFEC technique and probe

For high sensitive detection of defects in PFBR SG tubes using RFEC technique, it is important to design a probe with the receiver coil exactly placed in the remote field region. This is possible only when the direct field, transition and remote field regions are accurately identified. In this context, there is a strong need to study the existence of RFEC region in PFBR SG tubes to optimized probe design. This could be accomplished either by controlled experimentation or by numerical modeling.

Teitsma *et al* (2005). used RFEC technique for detection of external corrosion in 152.4 mm OD, 6.35 mm wall thickness, seamless unpiggable gas pipelines [49]. They carried out pull out test by displacing the receiver coil in the axial direction keeping the exciter coil at a fixed position, to identify the locations of direct, transition and remote field regions. The pull out test was performed at excitation frequencies of 32 Hz and 63 Hz. It revealed the existence of remote field region at 254 mm from the exciter coil, *i.e.* ~1.7 times the pipe OD.

However, performing such pull out test is cumbersome and tedious, for wide range of frequencies and excitation currents, especially in small diameter tubes. Numerical modeling is attractive to identify the RFEC region in such cases. Palanichamy (1987) reported the results of the application of an axisymmetric finite element (FE) model in 25 mm ID and 35 mm OD steel casing [50]. The relative permeability of the pipe was 70 and the electrical resistivity was 15 μΩ-cm. He predicted the RFEC response due to OD flaws of depths in the range of 1 mm to 4 mm. RFEC signals were predicted at an operating frequency of 90 Hz for the receiver coils placed at different locations *i.e.* in the transition region and different positions in the remote field regions. Studies revealed that the RFEC signals characteristics were found to be similar when the receiver coils was kept within the RFEC regions.

Lord *et al.* (1988) studied the physics behind the RFEC technique through an axi-symmetric FE model [51]. The predictions revealed the presence and the extent of phase knots and potential valley between the excitation and sensor coils. They also explored the subtle difference between the conventional EC and RFEC techniques, in the context of RFEC technique possessing equal sensitivity to both ID and OD defects.

Shin *et al.*(2001) explored the RFEC phenomenon in nonmagnetic Inconel 600 SG tubes (19.685 mm ID and 22.225 mm OD) through an axi-symmetric FE model [52]. They observed the existence of phase knots and potential valley at 300 kHz and the transition region occurring within one tube diameter axial distance. The predicted optimum distance between exciter and sensor coils was found to be 1.5 times the OD for the detection of defects. This distance, is half of the distance for an equivalent ferromagnetic tube.

Musolino *et al.* (2012) used semi-analytical model in which the governing partial differential equation was solved by analytical means in Fourier transform domain [53]. The constant coefficients in the resulting modified Bessel function were obtained through solving simultaneous linear equations. The model was applied to a ferromagnetic tube having 60 mm ID and 74 mm OD (μ_r=190 and σ = 10.5x10^6 S/m). The predictions of the semi-analytical model were compared with a numerical model and experimental results and were found to be within 10%.

3D FE modeling was also reported by researchers for prediction of RFEC response from localized defects. Mihalache *et al.* (2005) developed a 3D model using second order tetrahedral finite elements to predict and experimentally validate the RFEC behavior in 2.25Cr-1Mo SG tubes [54]. However, 3D FE models are computationally intensive and time consuming, as compared to 2D or axi-symmetric models. In this regard, several approaches were proposed by various research groups to improve the computational efficiency and to get quicker solution. Zhang *et al.*(1998) developed a quarter-model exploiting the radial-axial and radial-circumferential symmetry in large diameter pipes and studied the RFEC signals from near-side and far-side cracks [55]. Lin *et al.* (1990) employed ‘‘zoom-in’’ technique, in which the solution at the boundary was obtained from an equivalent 2D problem and this was used for solving the larger 3D problem [56].

However, most of the numerical modeling studies reported in the literature are based on linear models which do not take into consideration the nonlinear variation of the permeability with excitation current. These models assume a constant relative permeability of the material. In this regard, there is a strong need to develop and apply numerical models that incorporate the nonlinear material property.

Ostermeyer (1998) attempted to address this issue through a nonlinear model, based on an iterative approach [43]. In this model, the BH characteristic of the magnetic material obtained at an operating frequency of 80 Hz was given as an input to the model. In this iterative model, the predicted magnetic flux density (B) was used to interpolate in the BH curve to obtain the magnetic field (H). The iteration process continued till the interpolated H and model predicted H converged. The predictions were made for a tube of 80 mm OD and 6.5 mm thickness. Significant difference in the model predicted induced voltage in the receiver coil was observed between the linear and nonlinear models, when the exciter coil current was varied as shown in Figure 2.8.

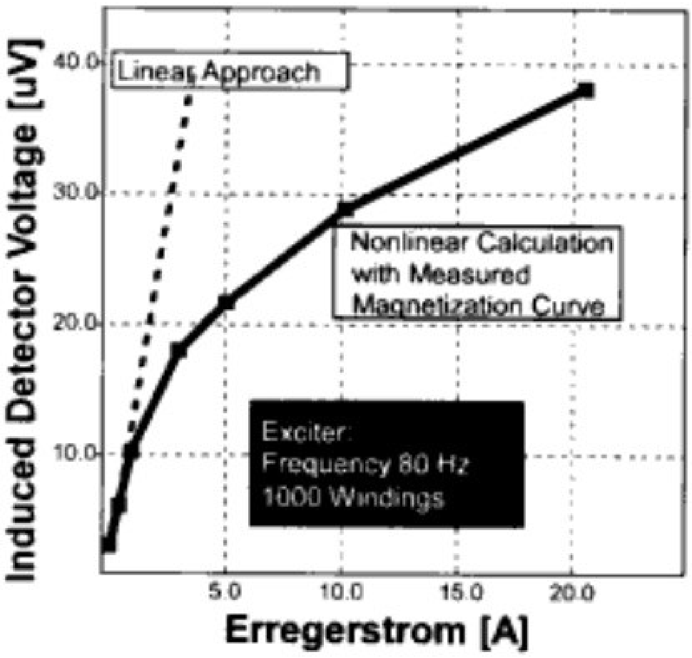

Figure 2.8 Difference between the linear and nonlinear model predicted induced voltages (μV) in the RFEC receiver coil as a function of excitation current (A) [43].

However, studies related to such nonlinear models are scarce in open literature. Hence, it is important to carry out nonlinear model of the RFEC technique for optimization of the probe to achieve high sensitive defect detection.

2.5.2 RFEC instrumentation

High sensitive detection of defects using RFEC technique is possible by appropriate design of the instrument. In RFEC technique, the induced voltage in the receiver coil is of the order of μV and is heavily influenced by the materials noise due to the diffusive electromagnetic fields. The RFEC instrument should be able to detect feeble information from defects.

The RFEC instrument in early days of invention consists of a function generator along with a power amplifier for excitation and a measurement system for pickup coil voltage [39]. Atherton *et al*. (1988) used a phase sensitive detector to analyze the receiver coil voltage [57]. The phase sensitive detector measured the phase of sinusoids, merged in noise and was used for measurement of weak fields enabling detection of small localized defects. They employed a preamplifier mounted on the RFEC probe to amplify the receiver coil voltage, prior to the phase sensitive detector. The phase sensitive detector produced two DC outputs corresponding to in-phase and quadrature components of the receiver coil voltage. The output of the phase sensitive detector was read into a personal computer using analog-to-digital converter. This experimental measurement system was used for detecting defects in the pressure tubes of the CANDU type nuclear reactors. They could detect 1 mm deep (25% WT) axial and circumferential slots on the OD side of the pressure tubes.

Dubois *et al.*(1992) reported the use of a PC lock-in amplifier based RFEC instrument to detect and size corrosion loss in 102 mm ID, 114.3 mm OD steel casings [58]. They studied the performance of the RFEC probe in the transition region and found that the impedance plane RFEC signals due to permeability noise and defect had different phase angles which could be used for their classification.

Nestleroth (2005) reported a PC based instrument shown in Figure 2.9 comprising of a rotating permanent magnet excitation with multiple Hall sensor receiving elements [59]. The Hall sensor outputs were initially conditioned and amplified and were acquired by a PC using 24-bit high dynamic range A/D converter. Three such A/D converters were synchronized using an optical fiber. Labview software based lock-in amplifier was used for phase and amplitude measurement of the Hall sensor output. This new technique was applied for the detection of a variety of artificial, simulated corrosion anomalies such as circumferential grooves, partial penetration welds, metal loss in steel pipes of 300 mm OD and 9 mm thickness. They could successfully detect metal loss with a minimum depth of 35% WT having length and width of 30 mm.

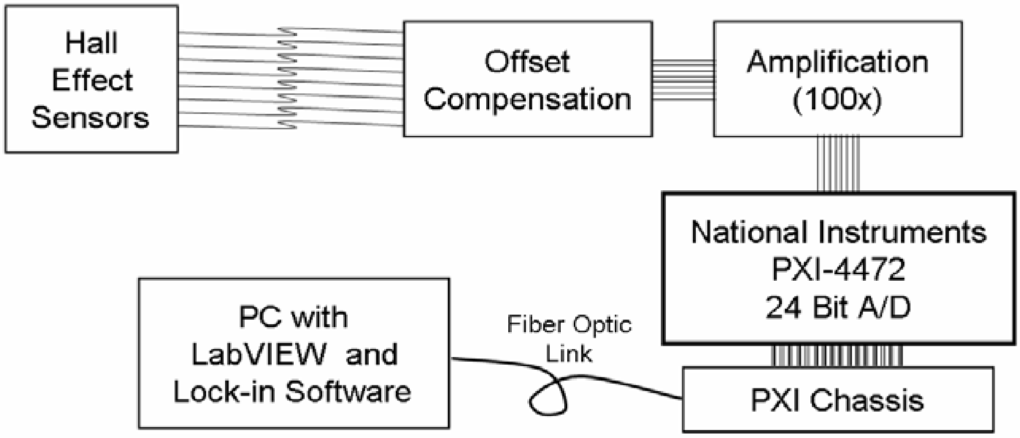

Figure 2.9 Schematic of the RFEC instrument used in [59].

Sun et.al (1997) have developed remote field eddy current technique for inspecting Aluminium plates of thickness up to 12 mm [40]. They employed a pot cored excitation coil and E-cored receiver coil RFEC probe and used SQUID based measurement system for sensing the feeble receiver coil response. Detection of deep sub-surface defects located between 12 mm and 25 mm in aluminum plates has been demonstrated using this RFEC probe, which is beyond the capability of conventional single frequency EC techniques.

Witte *et al.*(2006) developed RFEC technique for the inspection of weld seams of thick wall austenitic steel tubes from the external side using a probe with exciter and receiver coils separated by few centimeters [41]. They used a conventional EC tester and connected the RFEC probe in send-receive mode. They demonstrated detection of a drilled hole of 1.5 mm diameter and internal (subsurface) notches of 15% and 30% WT depths having a width of 1.5 mm.

It is inferred from the open literature that the use of lock-in amplifier based instrumentation is essential in RFEC instrument for the measurement of weak fields from defects and for phase sensitive detection. Other advancements as inferred from the literature include i) increase in the dynamic ranges of the A/D converters, ii) use of multiple receiver coil elements and iii) use of computer based measurement system.

2.5.3 RFEC detection of defects

In a typical SG tube the RFEC detection of defects is influenced by several geometrical and physical constraints. Detection of defects in the expansion bend regions of the SG tubes is one such geometrical constraint and is highly influenced by disturbing variables such as changes in electromagnetic coupling due to exciter-receiver coil misalignment, bending stresses, magnetic permeability variations and probe wobble. In RFEC probe, the exciter-receiver misalignment may cause the detector to move into the transition region, leading to large amplitude disturbing signals.

Atherton *et al*. (1992) studied the effect of eccentricity and tilt of exciter on RFEC response [60]. They carried out pull out tests in a test rig on 208 mm ID steel casing, to investigate the effect on the remote field. The measurements showed that, if the detector coil is positioned well within the remote field region, the RFEC effect is unchanged by tilt and eccentricity of the exciter for pipeline steel at operating frequencies of about 100 Hz. Tilt and eccentricity result in the extension of the transition regions farther into the remote field region up to a point about 3.5 pipe IDs from the exciter coil at which point the remote field dominates. In this context, Atherton *et al*. (1992) suggested approaches such as use of cores and shields and maintaining large enough coil spacing to ensure that the receiver coil stays always in the RFEC region.

Sutherland and Atherton (1997) studied the effect of bending stresses on RFEC signals [61]. They examined different stress states such as elastic, plastic and residual. They conducted studies in (32.8 mm ID, 38 mm OD) steel tubes bent in a special bending rig and used spot type receiver coils. The generated stress in the steel tube depends on the distance from a neutral plane in the bending rig and the bending moment at that axial location. Studies revealed that the bending stresses and tube curvature produced distinct RFEC signals. The RFEC signals due to elastic stresses had the same signatures as that of the defects due to wall loss defects and hence, were misinterpreted. They concluded that the effects of bending stresses and tube curvature must be considered while interpreting the RFEC signals of defects.

Rosen and Atherton (1993) reported the use of conducting shielding near the exciter coil to minimize the effects of coil tilt [62]. They carried out pull out tests with coil tilts for steel and aluminum shielding. Their observation revealed that, in general, the conducting shielding rapidly attenuates the strong direct field, thereby bringing the transition region close to the shielding. The tilt, further affects the transition zone by either changing its extent in steel or moving the transition point in Aluminum.

In general, signal processing techniques are resorted when disturbing noise such as the ones discussed earlier occurs in any measurement. Upda *et. al.* (1987) used Fourier descriptors for classification of RFEC signals which are influenced by noise [63]. The Fourier descriptor uses the differences in the shape of the trajectories as a basis for discrimination. The Fourier descriptors derived from the closed loop trajectories of the RFEC signals were incorporated into a feature vector and a nearest neighbor rule was used to classify the RFEC signals of unknown defects. Test results on a variety of machined defects such as through holes, OD slots and wall thinning could be reliably classified using this scheme. Lopez *et al.* (2008) applied discrete wavelet transform based signal processing to eliminate noise due to probe wobble in EC testing of SG tubes [64]. They used different wavelets such as Harr, Dabauchies (DB), and Biorthogonal. Using a differential bobbin type probe, they obtained signals of artificial holes of 0.9 mm and 1.1 mm diameter in a stainless steel tube of 19.05 mm ID, 21.53 mm OD. They reported that the 'db5' wavelet preserved the signal characteristics and effective in removing the wobble noise.

Detection of defects under the support structures of the SG tubes is another important aspect. As the support plates themselves are electrically conducting, they produce large amplitude disturbing signal, masking the desired information of defects such as denting and fretting corrosion under the support structures. Support structures interrupt the electromagnetic field travelling from exciter to detector, thus creating a shadow [48]. As a result, the detector coil voltage changes significantly and the sensitivity to defects reduced due to this large changes in the detector coil voltage. One way to remove such shadow effect is the use of dual exciter or dual receiver type RFEC probes, as reported by Mackintosh and Beresford (2005) [48]. In dual exciter

RFEC probe, two exciter coils are placed symmetrically on either side of the receiver coil. This type of probe was shown to improve the detection sensitivity near the support plate by removing the shadow. The dual receiver RFEC probe was also reported to be helpful in removing the shadow. However, these types of probes produce complex signals which are difficult to interpret.

The RFEC signal response of support plates was examined by Shatat *et al.* (1997) using a FE model [65]. They obtained the phase angle of the detector coil voltage, exactly under the support plate in the presence of grooves simulating fretting wear in the tubes. They analyzed the slope of the phase-frequency curve with and without support plates and defects under support plate. For constructing the phase-frequency curve the detector voltage was acquired beneath the support plate at different frequencies in the range of 10-20 Hz. The phase-frequency curves were also experimentally measured in a carbon steel pipe of 19 mm OD (2.3 mm wall thickness) and 6.4 mm thick support plate having an OD of 19.8 mm. The measured phase angle as a function of the square root of frequency was plotted to obtain the phase-frequency curves as the phase angle follows the skin depth relation. The slope of the phase-frequency curve without support plate and defects was found to be -19.8° and with support plate was -20°. When 37% and 81% WT deep grooves were placed under the support plate, the slopes of the phase-frequency curves changed significantly to -16.7° and -12.3° respectively as shown in Figure 2.10. These slopes in combination with the skin depth equation were used to estimate the wall thinning to a reasonable accuracy of 31% and 76% respectively. Hence, they recommended a multifrequency approach for sizing of fretting wear under support plates.

ISI of the PFBR SG tubes would be carried out during plant shut down when sodium and water are drained. In such conditions, there is a possibility that stray sodium would remain on the outer surface and also would fill the defects, if any, on the SG tubes. This is expected to adversely affect the RFEC signals, as sodium is electrically conducting.

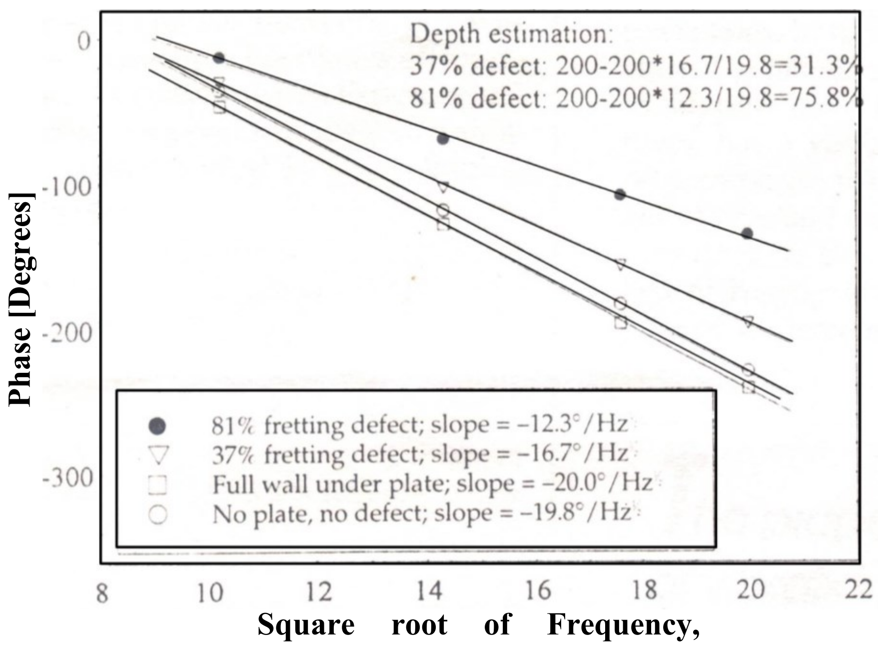

Figure 2.10 Slope of the Phase-frequency curves for support plate and defects [65].

Studies on the effect of sodium on RFEC signals are scarce in open literature. Ovidiu *et al.* (2009) studied the influence of support structure and sodium on the RFEC signals. They proposed a three frequency mixing technique for suppressing the RFEC signals due to sodium and support structures in SG tubes of FBR made up of Cr-Mo steel having 24.2 mm ID and 32.8 mm OD [66]. They used 150 Hz, 450 Hz and 600 Hz for signal mixing. A multifrequency mixing algorithm based on the affine transform was proposed and the mixing parameters were optimized using a numerical model. Experimental studies were conducted in a sodium test vessel with OD grooves and support plates. They observed that the two frequencies mixing (450 Hz, 600 Hz) yield higher SNR for eliminating the RFEC signals due to support structures when sodium is not present. They reported that three frequency mixing was necessary for eliminating the RFEC signals when sodium and support plates are present. The three frequency mixing resulted in 4 times improvement in the signal strength as that of the noise (support structure and sodium signals).

Ovidiu *et al.*(2011) studied multifrequency mixing of RFEC signals predicted by a numerical model for eliminating disturbing signals generated by support structure and sodium from that due to defects [67]. Possible combinations of RFEC signals due to support plate, sodium deposits and defects were subjected to dual frequency mixing (150 Hz and 450 Hz). The RFEC signals were also analyzed for case of one individual tube and the support plate covering 9 adjacent tubes in the SG. The study reported that a 20% reduction of support plate signal due to electromagnetic shielding of the surrounding tubes was observed for large support plate models. However, it was possible to increase the SNR of defects under support plate of a large model with multiple SG tubes. Multifrequency approach is promising for the detection of defects in the presence of support structures in RFEC testing.

2.6 Motivation

For high sensitive detection of defects in SG tubes, it is essential i) to identify remote field region for placing the receiver coil and ii) to optimize the operating frequency maximizing the defect detection. As inferred from the literature, model based studies are essential and useful to accomplish these tasks. However, as discussed in Section 2.5.1, numerical models incorporating the nonlinear material characteristics are scarce in open literature. Hence, there is a strong need to develop and use nonlinear models to study the RFEC technique in these small diameter SG tubes of interest.

Development of RFEC instrument capable of measuring small amplitude (of the order of μV) changes in the receiver coil is vital for high sensitive detection of defects. As observed from the literature, development of RFEC instrument based on lock-in amplifier is necessary for the measurement of such weak responses and phase sensitive detection of receiver coil voltage.

As discussed in Section 2.5.3, studies in the literature confirmed the influence of disturbing noise from electromagnetic coupling due to exciter-receiver coil misalignment, bending stresses, magnetic permeability variations and probe wobble in the bend regions of the tube on RFEC signals. However, efforts have not yet been made in processing the signals to eliminate disturbing noise. Offline and online signal processing techniques, exploiting the spectral characteristics and frequency localization properties of the RFEC signals, is beneficial to eliminate strong disturbing noise and enhance genuine defects signals.

As discussed in Section 2.5.3, the influence of sodium deposits on RFEC signals has not been studied in detail. Hence, it is important to experimentally study the influence of sodium on RFEC signals of defects and explore possible approaches to minimize the influence, if any. Signal feature identification based approach is attractive in this context, and this may enable detection and sizing of defects in the presence sodium. As also noted from the literature, multifrequency methods are useful to detect defects under the support structures.

2.7 Objective of the thesis

The primary objective of the research work is to develop RFEC technique for in-service inspection (ISI) of PFBR SG tubes. The following approaches are being proposed to achieve this:

1) Carry out nonlinear finite element modeling for optimization of the RFEC technique in modified 9Cr-1Mo ferromagnetic SG tubes of PFBR.
2) Develop high sensitive noise-free, lock-in amplifier based RFEC instrument
3) Apply signal processing based approach to eliminate strong disturbing noise from the bend regions of the SG tubes.
4) Experimentally study the influence of sodium on RFEC signals of defects and to explore signal feature based approach for detection and sizing of defects.
5) Develop multifrequency mixing approach for detection of defects under the support structures of the SG tubes.

2.8 Organization of the thesis

The rest of the thesis has been organized in the following manner:

Chapter 3 presents the approach based on nonlinear 2D-axi symmetric finite element (FE) model to optimize RFEC probe. This chapter provides the formalism of the FE model to handle nonlinear magnetic permeability. It discusses the application of this model to identify direct, transition and remote field regions in SG tubes and to optimize the excitation frequency. This chapter also discusses the experimental details and development of lock-in amplifier based high sensitive RFEC instrument and flexible RFEC probes.

Chapter 4 starts with the detection of different types of defects such as flat bottom holes, notches and grooves towards establishing the sensitivity of the RFEC technique, in the straight sections of the SG tubes. It presents the issues related to the detection of defects in the bend regions of the SG tubes. Further, it discusses various digital signal processing techniques for detection of defects in the bend regions and proposes an effective approach after detailed experimentation.

Chapter 5 explains the experimental investigations conducted in a sodium test vessel with SG tubes having uniform wall loss defects of different depths and then presents an approach for detection of defects in the presence of sodium deposits. It also discusses the new dual frequency mixing algorithm based on linear kernel transform for detection of defects under the support structures. It highlights the results of the mixing algorithm to model predicted RFEC signals of grooves.

Chapter 6 summarizes the major conclusions drawn from the research work and Chapter 7 provides the scope for future research directions.

Chapter 3: Model based approach for optimization and experimental validation

3.1 Introduction

This chapter discusses the optimization of the RFEC technique for achieving high sensitive defect detection. Optimization of the RFEC technique involves the identification of the remote field region for placing the receiver coil and selecting the operating frequency at which the RFEC characteristics are well defined and the response to defects in the tube is high. Finite element (FE) method based optimization has been followed in this research work.

3.2 Finite element modeling

The FE method solves the governing partial differential equation in a domain of interest [68]. A variety of validated software are available in the open literature [69,70]. In this method, the domain of interest is discretized into a finite number of sub-domains, usually referred as elements [71,72]. The interconnecting points are called nodes. The exact variation of the unknown function (e.g. potential) is approximated by simple interpolation functions with unknown coefficients at each nodes associated with the elements. In other words, the original boundary value problem with infinite degrees of freedom is transformed into a problem with finite degrees of freedom. Then, a system of algebraic equations is obtained by applying the Ritz variational or Galerkin procedure and solution of the boundary value problem is obtained by solving the system of linear equations [72]. The variable in question, such as potential, field, etc. are computed at the nodes situated within the region of interest. Finally, desired response of intent such as induced voltage and impedance are determined from the model variable data. In the case of RFEC probe coil problem the excitation coils exhibit cylindrical symmetry and 2D model is sufficient.

3.3 Differential formulation of RFEC problem

The governing partial differential equation of RFEC phenomenon is similar to the conventional eddy current technique as described in Section 1.4.1. This can be derived from the Maxwell's curl equations as given below [69,73]:

$$\nabla \times \boldsymbol{E} = -\frac{d\boldsymbol{B}}{dt} \qquad \text{... 3.1}$$

$$\nabla \times \boldsymbol{H} = \boldsymbol{J} + \frac{d\boldsymbol{D}}{dt} \qquad \text{... 3.2}$$

where **E** is electric field, **B** is magnetic flux density, **H** is magnetic field intensity, **J** is current density and **D** is the displacement current. In equation (3.2) the displacement current term can be ignored as it is insignificant in quasi-static cases. The constitutive relation is **B**=μH**,** where μ is the magnetic permeability of the material. The relationship between B and H for ferromagnetic materials such as modified 9Cr-1Mo considered in the present study is nonlinear, wherein μ is a function of B:

$$\mu(\boldsymbol{B}) = \frac{\boldsymbol{B}}{\boldsymbol{H}(\boldsymbol{B})} \qquad \text{... 3.3}$$

The magnetic flux density is written in terms of the vector potential (**A**) as:

$$\mathbf{B} = \nabla \times \boldsymbol{A} \qquad \text{... 3.4}$$

Introducing the vector potential in equation (3.2) and using equation (3.31), we obtain:

$$\nabla \times \left[\frac{1}{\mu(\boldsymbol{B})} \nabla \times \mathbf{A}\right] = \boldsymbol{J} \qquad \text{... 3.5}$$

For time varying magnetic fields, the current density is actually a combination of the induced eddy current density ($\mathbf{J_e}$) in the material and the applied source current density ($\mathbf{J_s}$), *i.e.* $\mathbf{J}=\mathbf{J_e}+\mathbf{J_s}$. Then equation (3.5) is written as:

$$\nabla \times \left[\frac{1}{\mu(\boldsymbol{B})} \nabla \times \mathbf{A}\right] = \boldsymbol{J_e} + \boldsymbol{J_s} \qquad \text{... 3.6}$$

The induced current density $\mathbf{J_e}$ obeys the constitutive relation of $\mathbf{J_e}= \sigma\mathbf{E}$. The induced electric field obeys equation (3.1). Substituting the vector potential form of B into equation (3.1) yields:

$$\nabla \times \boldsymbol{E} = -\frac{d(\nabla\times\boldsymbol{A})}{dt} \qquad \text{... 3.7}$$

Equation (3.7) can be written as

$$\nabla \times \left[\boldsymbol{E} + \frac{dA}{dt}\right] = 0 \qquad \text{... 3.8}$$

Equation (3.8) introduces the notion of a curl less quantity which can be written as the negative gradient of a scalar potential as follows:

$$\boldsymbol{E} + \frac{dA}{dt} = -\nabla V \qquad \text{... 3.9}$$

where V is the electric scalar potential. For sinusoidal excitation with frequency (f) a time dependence of $e^{-j\omega t}$ can be assumed where $\omega=2\pi f$. This will transform equation (3.9) into

$$\boldsymbol{E} = -j\omega\boldsymbol{A} - \nabla V \qquad \text{... 3.10}$$

Substituting equation (3.10) in (3.6) yields the governing partial differential equation of the RFEC phenomenon:

$$\nabla \times \left[\frac{1}{\mu(\boldsymbol{B})} \nabla \times \mathbf{A}\right] = -j\sigma\omega\boldsymbol{A} - \sigma\nabla V + \boldsymbol{J_s} \qquad \text{... 3.11}$$

Equation 3.11 has been solved by FE method using FEMM software.

3.4 The FEMM software

In this study FEMM (Finite Element Method Magnetics) software has been used to solve the governing partial differential equation of eddy current behavior in a conducting and magnetic material. FEMM is an open source software and is a suite of programs for solving static and low frequency electromagnetic problems in two-dimensional planar and axisymmetric domains [69,73]. It addresses the linear as well as nonlinear time harmonic magnetics, linear electrostatic and steady state heat flow problems. FEMM software composed of the following three major parts:

1. **Interactive shell:** Encompass graphical pre- and post- processors. It is a CAD interface to define the geometry of the problem or import the standard CAD models.
2. **Mesh generator**: Discretize the problem domain into large number of triangular elements. FEMM software uses the triangle program developed by *Jonathan Richard Shewchuk* for this purpose [74]. The triangle program generates exact Delaunay triangulations, constrained Delaunay triangulations, conforming Delaunay triangulations, Voronoi diagrams, and high-quality triangular meshes.

3. **Solvers**: The solver takes a set of data files that describe the problem and solves the governing partial differential equation to obtain the desired potential values throughout the solution domain. FEMM has been integrated with Lua scripting language for enabling the user to create batch runs, parametrically describe the geometry and to perform optimization.

For geometries exhibiting cylindrical symmetry such as the RFEC tube-coil problem, Equation (3.11) is expressed in cylindrical polar coordinates with A_r, A_φ and A_z. In this case the excitation source (coil carrying current) is along φ direction. Hence, A_r and A_z are identically zero and it is sufficient to solve only for the φ component of the magnetic vector potential. In equation (3.11), the magnetic permeability is a nonlinear function of the applied magnetic field (H). An iterative method is preferred for solving such problem [69]. FEMM software handles this type of nonlinear magnetic material property through the concept of complex effective permeability.

FEMM software has been used successfully for solving SQUID based eddy current NDE problem [75]. In this particular work, a scheme has been proposed to rapidly estimate the depth of an unknown flaw from 2D FE calculations using sheet inducer geometry. The linear variation of phase of the defect magnetic field has been utilized for estimating the depth of subsurface flaws. The flaw depth estimation results have been found to be in good agreement with experimental data obtained with a double-D coil excitation.

3.5 Formalism for nonlinear material modeling

The nonlinear formalism is based on an effective BH curve as reported in [76,77] by taking $\boldsymbol{H}$ to be a sinusoidally varying quantity. The amplitude of $\boldsymbol{B}$ is obtained by taking the first coefficient, $\boldsymbol{B_{fund}}$ (fundamental harmonic) in a Fourier series representation of the resulting $\boldsymbol{B}$. Linear interpolation is performed between the user-defined points on the BH curve, for the purpose of this Fourier series computation. A nonlinear hysteresis lag parameters is then applied to the effective BH curve as given in equation 3.12 below:

$$\mathbf{B}_{eff} = \boldsymbol{B}_{fund} e^{-j\varphi} \qquad \text{... 3.12}$$

where $\mathbf{B_{eff}}$ is the effective magnetic flux density, φ is the frequency independent phase lag between $\mathbf{B_{eff}}$ and $\mathbf{B_{fund}}$ called as hysteresis lag parameter. The hysteresis lag parameter is assumed to follow the permeability, hence, it can be written as:

$$\frac{\varphi}{\varphi_{max}} = \frac{\mu}{\mu_{max}} \qquad \text{... 3.13}$$

Hence equation (3.12) can be rewritten as:

$$\mathbf{B}_{eff} = \boldsymbol{B}_{fund} e^{-\left[\frac{j\varphi_{max}\mu}{\mu_{max}}\right]} \qquad \text{... 3.14}$$

The value of φ_{max} as reported by Stoll [78] is less than 20 degrees, for most of the practically used steel materials. Thus, for a given input of the DC BH curve and the φ_{max} parameter, an effective BH curve is constructed after computing $\mathbf{B_{eff}}$ using the above formalism. This effective permeability model is used for modeling the RFEC technique.

3.6 Determination of the BH curve of modified 9Cr-1Mo steel

3.6.1 Experimental procedure

The BH curve of modified 9Cr-1Mo steel was experimentally obtained using method described by Soong (2008) [79]. The following steps have been adopted for the BH curve measurement of modified 9Cr-1Mo.

1) A ring type specimen was made out of modified 9Cr-1Mo steel with the following dimensions: OD 45.01 mm, ID 37.45 mm, and Thickness 3.75 mm (axial). This ring specimen was used as a magnetic core.
2) Two copper wires were concentrically wound on this core material. One winding (main winding) was used to create magnetic field intensity (**H**) by passing a known value of current (I_m).
3) The induced voltage (V_s) in the other winding (sense coil) was measured and used to compute the magnetic flux density (**B**).
4) The **H** and **B** fields were computed from the measured current and voltage from the main and secondary windings respectively. One cycle of a triangular waveform was applied in the main winding to obtain the entire hysteresis curve.

3.6.2 Computation of H and B fields from the measured current and voltage values

The magnetic field intensity created by the main winding is given by:

$$\boldsymbol{H}_m(t) = \frac{N_m(t) \times I_m(t)}{l_{core}} \qquad \text{... 3.15}$$

where N_m the number of turns in the main coil, I_m is the current in the main winding and l_{core} is the mean magnetic path length of the core (which is nothing but the mean radius of the core). All the parameters in equation (3.15) can be measured and hence the magnetic field intensity can be calculated.

The induced voltage in the sense coil winding V_s is given by:

$$V_s(t) = N_s \frac{d\varphi}{dt} = N_s A_{core} \frac{d\boldsymbol{B}}{dt} \quad \text{... 3.16}$$

where N_s is the number of turns in the sense coil and A_{core} is the cross sectional area of core. Rearranging equation (3.16) to solve for the flux density yields:

$$\boldsymbol{B}(t) = \frac{1}{N_s A_{core}} \int V_s \, dt \quad \text{... 3.17}$$

The induced voltage in the sense coil can be measured during magnetization of the core and numerically integrated to obtain **B**.

Figure 3.1 shows the experimentally obtained BH curve (for the initial magnetization) of the mod. 9Cr-1Mo steel using the method described in [79].

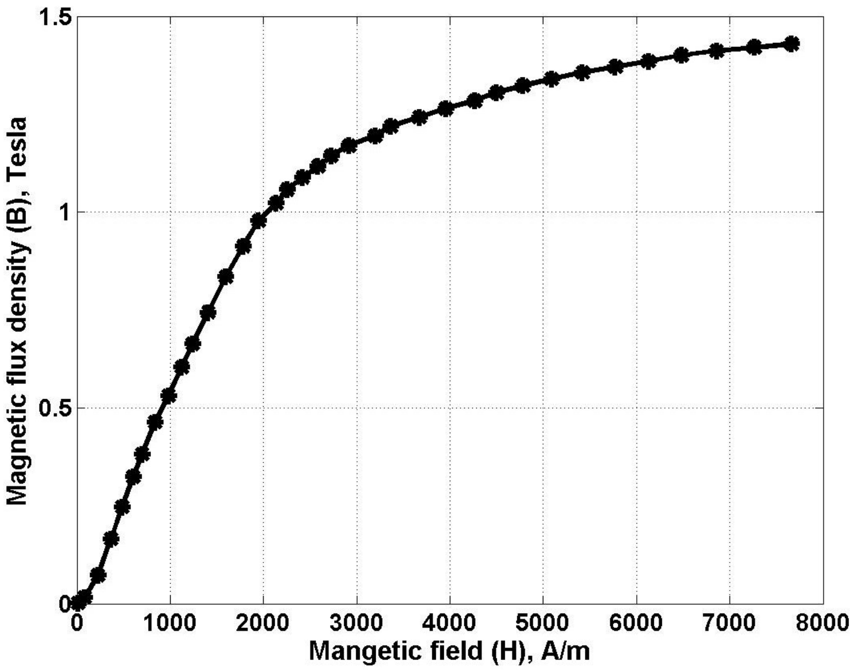

Figure 3.1 Experimentally obtained BH curve of modified 9Cr-1Mo steel.

3.7 Modeling of RFEC technique

Implementation of FE model involves the following major steps:

1. Construction of the model geometry and defining the material properties
2. Defining boundary condition
3. Meshing of the geometry
4. Solving the model and
5. Post processing of the model predicted vector potential

3.7.1 Construction of the model geometry

The RFEC geometry (domain of interest) consists of a modified 9Cr-1Mo SG tube, excitation coil and an outer air box. Figure 3.2 shows a part of the geometry for modeling the RFEC technique. Lua scripting with MATLAB interface was used to create the model geometry. The dimensions of the geometry and material properties of the tube coil and air box used in the model are given in Table 3.1 . The excitation coil consists of 400 turns of copper wire carrying 100 mA current.

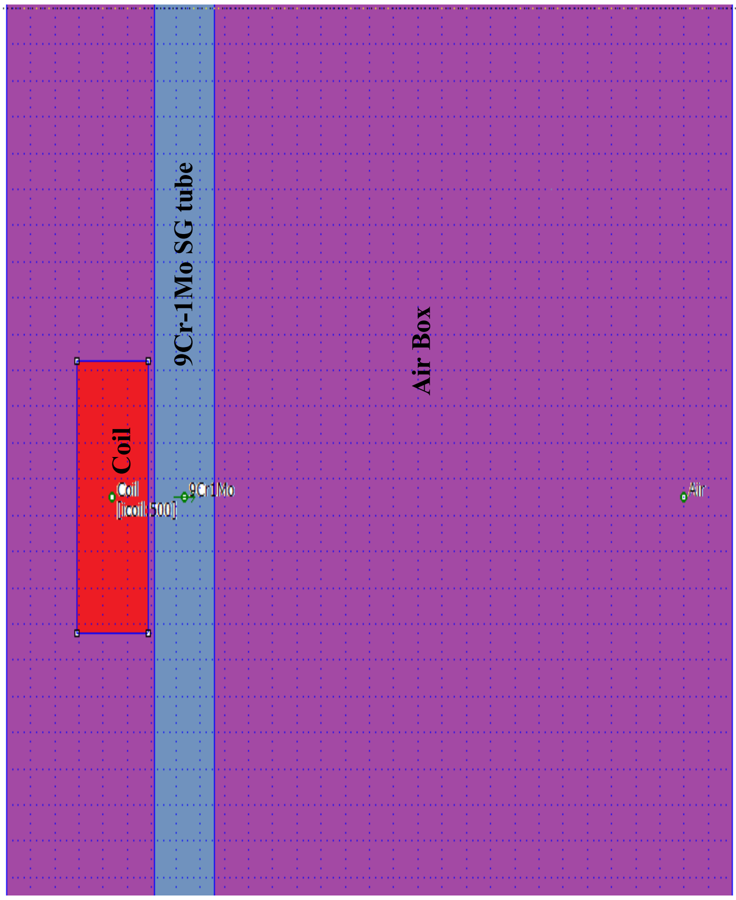

Figure 3.2 Geometric model of the RFEC technique.

Table 3.1 Dimensions and material properties used in the finite element model.

Region	Dimensions, mm			Electrical conductivity, S/m	Relative permeability
	Length	Inner dia.	Outer dia.		
SG Tube	200	12.20	17.2	2.3×10^6	BH curve input
Excitation coil	7.50	05.80	11.7	6.0×10^6	1
Air box	200	17.20	30.0	0	1

3.7.2 Boundary conditions

The two popular boundary conditions used in FE method are Dirichlet and Neumann conditions. Dirichlet or natural boundary condition defines the vector potential values at the outer boundary to zero. For imposing Dirichlet boundary condition, the outer boundary should be sufficiently away from the source. On the other hand, the Neumann condition sets the normal derivative of the vector potential to zero. For imposing the Neumann condition, the outer boundary should be smooth and extent of which should be determined by trial and error. FEMM software provides an option of asymptotic boundary condition which is a mixed Dirichlet and Neumann condition for open boundary problems like the RFEC problem. Open boundary conditions are used by several and explained elsewhere [80]. Asymptotic boundary condition has been defined at the outer boundary of the air box in the RFEC model geometry. This boundary condition reduces the effective size of the outer boundary such that higher number of mesh nodes in the outer air box could be reduced/avoided leading to quicker solution time.

3.7.3 Meshing of the model geometry

The region of interest is discretized by uniformly distributed triangular mesh elements. The mesh is optimized after systematic trial and error that give due emphasis to the solution accuracy and computational time. Table 3.2 gives the solution time and the vector potential values at r=7.45 mm and z=0 mm (middle of the tube wall) for different number of mesh elements. As seen from Table 3.2, the vector potential values tend to converge beyond 54642 elements. The solution time also increased significantly after 54642 number of mesh elements. Hence 54642 numbers of elements considered as optimum. This optimized mesh corresponds to approximately 2 elements per one standard depth of penetration at a nominal excitation frequency of 1000 Hz. Figure 3.3 shows the mesh in the RFEC geometry.

Table 3.2 The solution time and the vector potential values for different number of mesh elements

S. No.	**Number of elements**	**Solution time, S**	**Number of mesh elements across the tube thickness (2.3 mm)**	**Vector potential (A) x 10^{-5} T-m**
1	5126	0.35	1	0.0615
2	7189	0.53	2	0.2617
3	14222	0.73	3	0.2622
4	24735	1.16	4	0.2625
5	**54642**	**2.83**	**6**	**0.2632**
6	216574	16.30	10	0.2637
7	1332712	221.91	25	0.2636

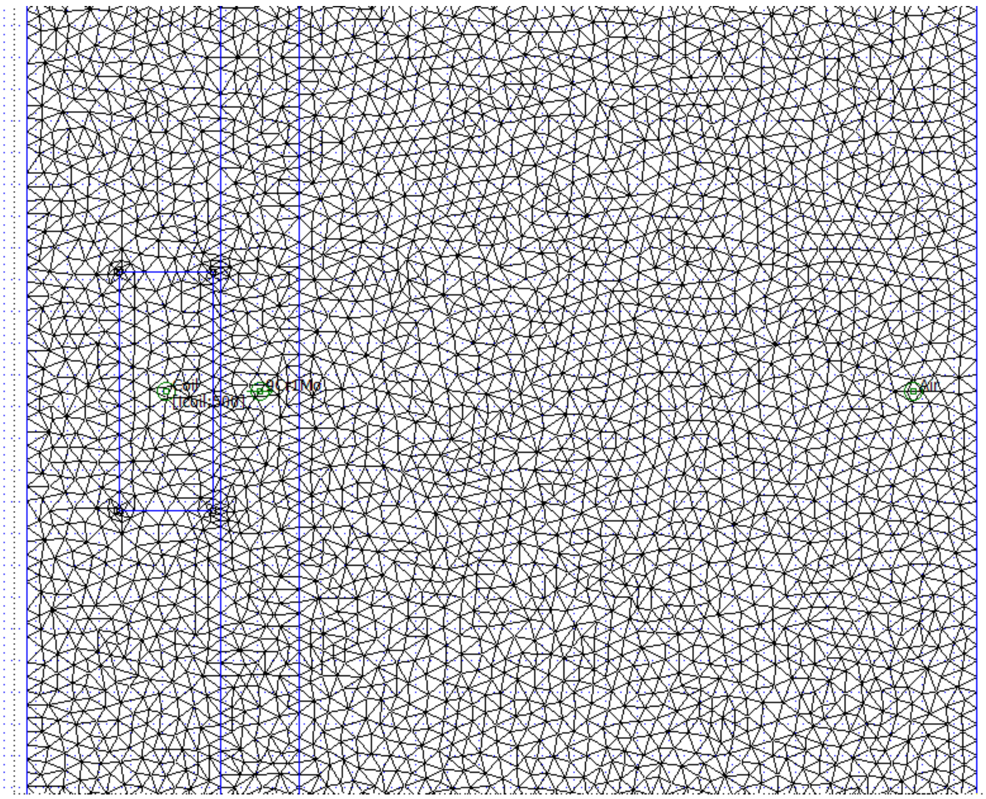

Figure 3.3 Triangular mesh generated in the RFEC geometric model.

3.7.4 Solving the model

Solving the model means finding the inverse of the resulting global matrix after discretization and applying the Ritz variational or Galerkin minimization to find the unknown vector potential values at the nodal points of the mesh. The global matrix for the time harmonic partial differential equation (3.11) is complex and symmetric in nature. Hence, the complex symmetric version of the Biconjugate gradient (BCG) matrix solver is used [81]. In linear algebra, the BCG is an algorithm to solve system of linear equations of the following form: **Ax=b,** Here A and b are known matrices and x is the unknown to be determined. The symmetric version of the BCG implementation takes advantage of the symmetric structure to minimize the number of computations that must be performed per iteration. The BCG solver was observed to be converging to a solution very slowly and required higher computational time [73]. Possible reason for this slow convergence was due to ill conditioning (higher condition number) of the matrix (A). The convergence could be accelerated by using Symmetric successive over relaxation (SSOR) preconditioner, to minimize the computational time [82]. Typical solution time in a standard Intel core I5, 3.6 GHz, 64 bit processor is 2.5 seconds for the RFEC problem geometry with 54642 elements.

3.7.5 Post-processing of model predicted vector potential

As discussed in Section 3.3, the model computes the φ component of the vector potential (A_{φ}) in the solution domain, which is used to calculate the radial, axial components of magnetic flux density and magnetic field as per the following equations:

$$B_r = -\frac{dA_\varphi}{dz} \qquad \text{... 3.18}$$

$$B_z = \frac{dA_\varphi}{dr} + \frac{A_\varphi}{r} \qquad \text{... 3.19}$$

In order to study the direct, transition and remote field regions, induced voltage in a single turn fictitious coil of 11.7 mm diameter inside the tube was computed for various axial positions from the exciter coil. As fields due to the coil decay exponentially, it reduces rapidly with axial distance. In order to perceive such changes, logarithms of the field quantities were analyzed. The amplitude (logarithm) and phase angle (degrees) of the induced voltage were analyzed as a function of axial distance from the exciter coil for determining the direct, transition and remote field regions. The analyses were carried out in frequency range of 100-1500 Hz where the SG tube is expected to exhibit RFEC characteristics.

3.8 Finite element model predictions

Figure 3.4 shows the surface plot of the logarithm of magnetic flux density and normalized arrow plots of the magnetic field at frequencies 700, 800 and 900 Hz. The surface plot provides the magnitude information and the arrow plots provide the direction of the magnetic field. The following two important observations can be made from Figure 3.4:

1) A clear boundary between 25 and 30 mm is observed in the arrow plots. This is mainly due to the back entry of the indirect field due to eddy currents which destructively interfere with the direct field of the excitation coil. Phase knots and potential valley forms at this boundary, which separates the direct and indirect fields.

2) Below 25 mm the arrows point in the direction of the direct field and above 30 mm the arrows point opposite to the direct field. This is mainly due to the back entered indirect field (due to eddy currents in the tube wall) which is out of phase with the direct field.

Potential valley and phase knots are not observed in the field plot of 700 Hz, but could be observed in the field plots of 800 and 900 Hz. This means that the presence of indirect field is dominant beyond 800 Hz. This, qualitative analysis confirms the presence of back entered indirect field due to eddy current in the tube wall beyond 30 mm distance from the excitation coil. Thus, the arrow and surface plot reveal the presence of direct, transition and remote field regions inside the tube wall.

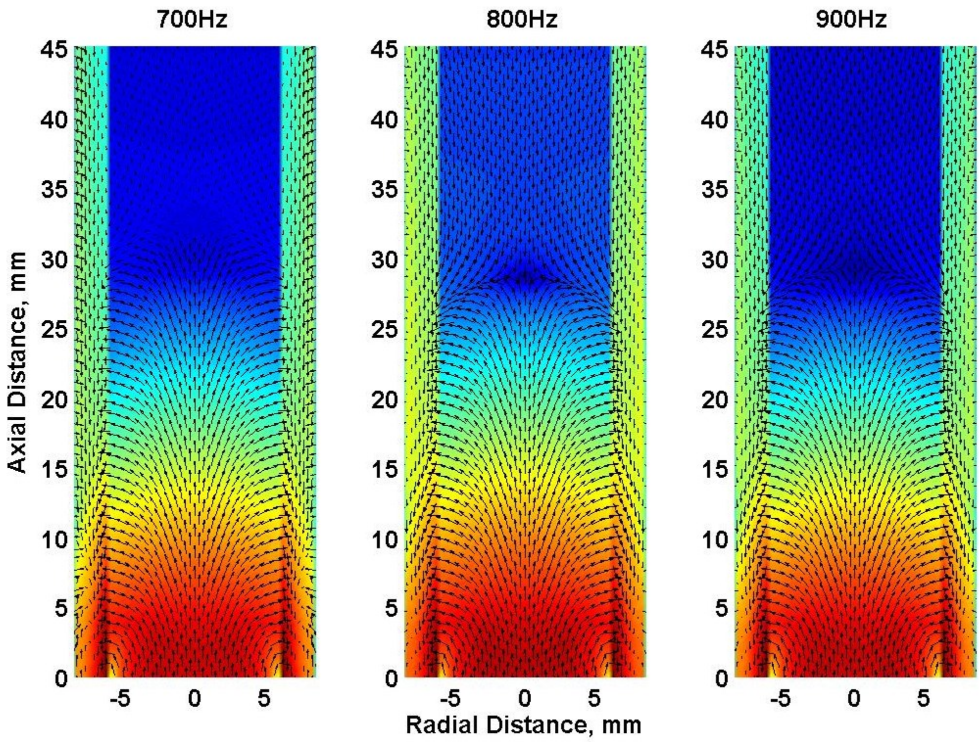

Figure 3.4 Surface plot of the logarithm of magnetic flux density and normalized arrow plots of the magnetic field at frequencies 700, 800 and 900 Hz.

Figure 3.5, Figure 3.6 and Figure 3.7 show the logarithm of amplitude and phase of the induced voltage in the fictitious finite size bobbin coil as a function of axial distance in the frequency range of 100 Hz to 1500 Hz in steps of 100 Hz. It can be observed from these figures that the amplitude of the induced voltage decreases exponentially up to a distance of 20 mm (Region I). There is a deviation in this exponential decay between 20 and 35 mm. In the frequency range of 100-500 Hz, a slope change is observed between 20 and 30 mm. Beyond 500 Hz, within 20-35 mm axial distance, the amplitude goes to minimum and then increases, thus forming a valley (Region II). Beyond 35 mm the amplitude again decreases exponentially with different rate as compared to the initial distance of up to 20 mm (Regions III).

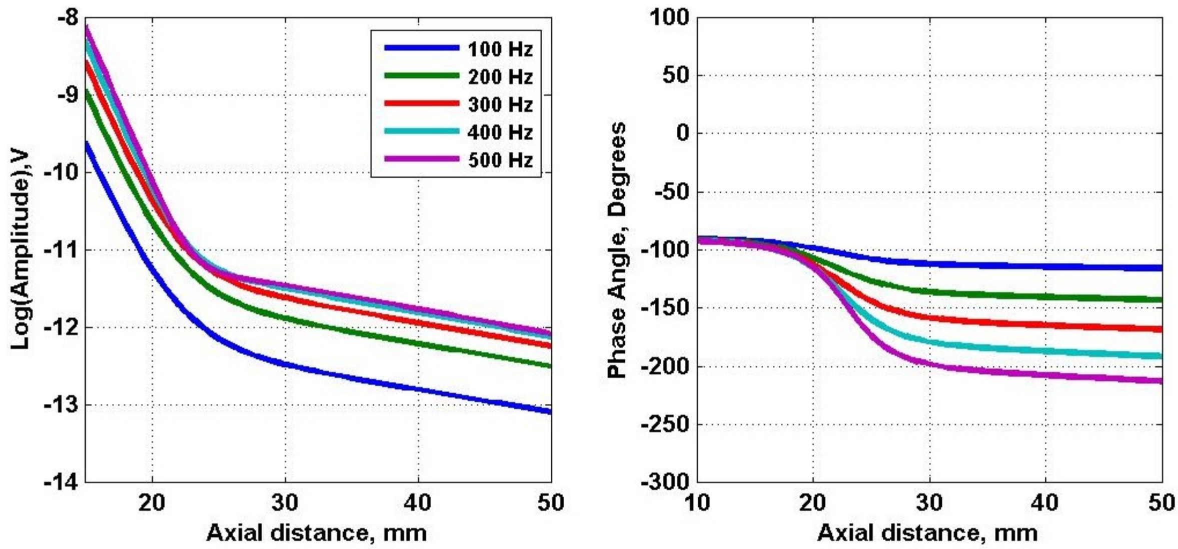

Figure 3.5 Amplitude and phase of the induced voltage in a receiver coil in the frequency range of 100 Hz to 500 Hz.

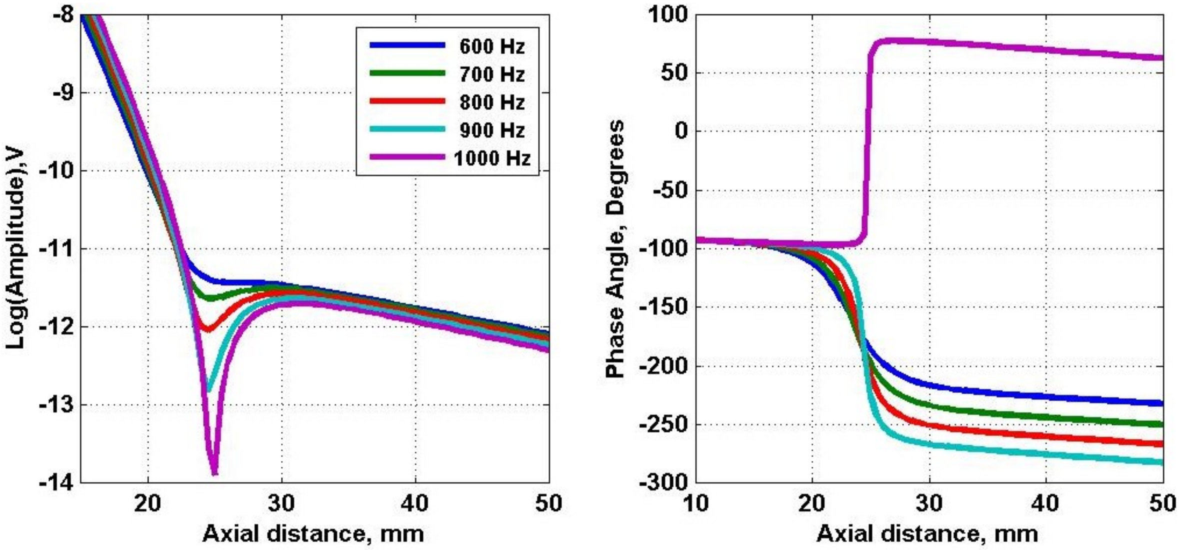

Figure 3.6 Amplitude and phase of the induced voltage in a receiver coil in the frequency range of 600 Hz to 1000 Hz.

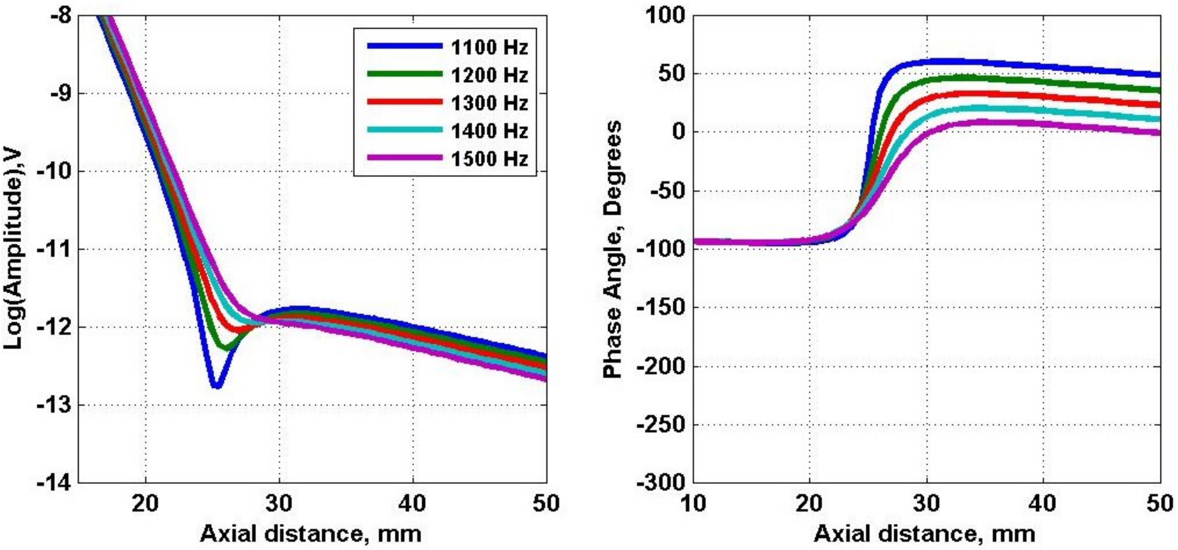

Figure 3.7 Amplitude and phase of the induced voltage in a receiver coil in the frequency range of 1100 Hz to 1500 Hz.

The phase angle of the induced voltage shows an abrupt change in the Region II *i.e.* between 20 and 35 mm. The Region I is mainly due to the exciter coil field, *i.e.* direct field region. In Region II, the direct field goes to a minimum and a part of the indirect field (eddy current) in the tube wall enters back inside the tube. The destructive superposition of the direct and indirect fields in this Region II is responsible for the valley in the amplitude. This region is the transition region. However, with further increase in the axial distance the direct field progressively becomes insignificant and the indirect field is dominant. This region III is the remote field region. These qualitative observations of the magnetic field contours agree well with the reported literature. As observed in Figure 3.5, the transition region is not been well defined in the frequency range of 100-400 Hz. Hence, further analysis has been restricted to 500-1500 Hz only. The phase angle of the induced voltage changes abruptly in the transition region. This signifies the clear influence of the indirect field which is out of phase with the direct field.

3.8.1 Optimization of the exciter-receiver coil spacing

In order to accurately characterize the direct field, transition and remote field regions the deviations from the straight line behavior of the logarithmic amplitude plots are analyzed as proposed by Schmidt *et. al.* [42]. The region between the two dotted lines A and B in

Figure 3.8 show the observed deviation in the linear behavior of amplitude and is taken as the transition region. With respect to this transition region, the direct field region is towards to the exciter coil (left of A) and the remote field region is away from it (right of B). The two dotted lines show the observed deviation in the straight line behavior. This deviation was quantitatively obtained by taking the difference between a straight line fit (red color) and original amplitude data in that region as shown in Figure 3.8. Wherever the difference was higher than 5%, that point was taken as the deviation point. Table 3.3 shows the calculated points A and B in the frequency range of 500-1500 Hz. Observation of the Table 3.3 reveals that the transition region starts in between 19 mm and 22 mm and the remote field region starts in between 32 mm and 40 mm. The transition region is sharper in the frequency range of 800-1200 Hz. The dip in the transition region implies that the direct and indirect fields are of similar magnitude, but differ in phase by 180 degrees [83,84]. Hence, the dip from the deviation point B denoted as (D) in Figure 3.8 has also been considered for distance optimization. The D values for different frequencies are given in Table 3.3. Observation of Table 3.2 reveals that the dip from point B, *i.e.* D is significant in the frequency range of 800-1200 Hz and the RFEC region in that range is from 34 mm to 36 mm. Thus, the spacing between the exciter and receiver coils should be at least 36 mm for the receiver to be correctly placed in the RFEC region and considered as the optimum distance.

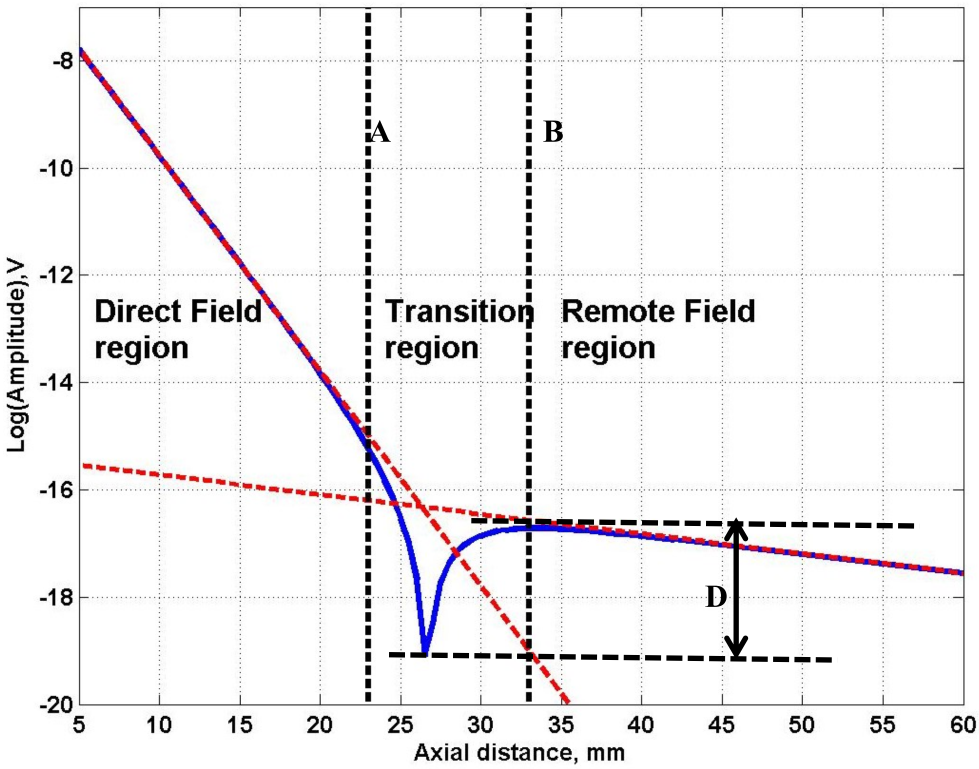

Figure 3.8 Characterization of direct, transition and remote field zones.

Table 3.3 Calculated A and B points as in Figure 3.8 at different frequencies for characterization of RFEC region.

S. No.	Frequency, Hz	A, mm	B, mm	B-A, mm	D, Volts
1	500	21.5	40.0	18.5	0
2	600	20.0	38.0	18.0	0
3	700	19.5	36.5	17.0	0
4	800	19.0	36.0	17.0	0.36
5	900	19.0	35.5	16.5	1.11
6	1000	19.5	35.0	15.5	2.13
7	1100	19.5	35.0	15.5	0.93
8	1200	20.0	34.5	14.5	0.40
9	1300	20.0	34.0	14.0	0.10
10	1400	21.0	33.5	12.5	0
11	1500	22.0	32.0	10.0	0

3.8.2 Optimization of operating frequency

In order to optimize the operating frequency, RFEC signal of 3 mm width OD groove, depths 0.23 mm (10% WT), 0.46 mm (20% WT), and 0.69 mm (30% WT) were predicted for frequencies in the range of 500-1500 Hz. The RFEC signal amplitudes were obtained by predicting the difference between the peak amplitudes of groove and groove-free regions. Figure 3.9 shows variation of this peak amplitude with frequency. As can be observed, the RFEC signal amplitudes show a peak at 825 Hz for grooves of 10%, 20%, and 30% WT deep. This operating frequency would be useful to detect defects with better sensitivity and hence, was considered as the optimum. In subsequent parts of the thesis, results for this optimum frequency will be presented and discussed.

3.8.3 Prediction of RFEC signals of grooves

The FE model was used to predict the RFEC signals (real and imaginary components of the induced voltage in the receiver coil) of OD grooves (axi-symmetric defects) in the SG tube. The optimized intercoil spacing of 36 mm and frequency 825 Hz were used for the prediction of RFEC signals of 20% (0.46 mm), 30% WT (0.69 mm) and 40% WT (0.92 mm) deep and 3 mm width grooves. The RFEC probe was parametrically moved inside the tube along the axial direction for 90 mm with a scan step of 0.5 mm, to obtain the RFEC signals. Figure 3.10 shows model predicted RFEC signals. The model predictions have been validated and the details are given in Section 3.12.

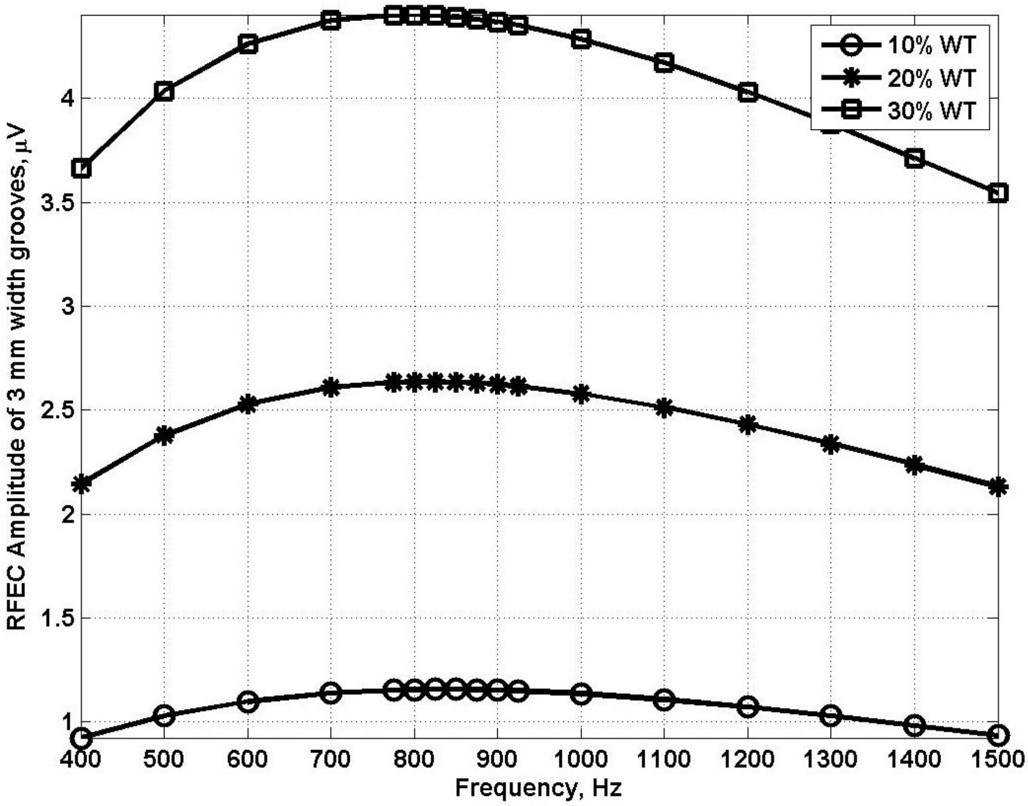

Figure 3.9 RFEC signal amplitude of a grooves (width 3 mm, and depth 10%, 20% and 30% WT) predicted at different frequencies.

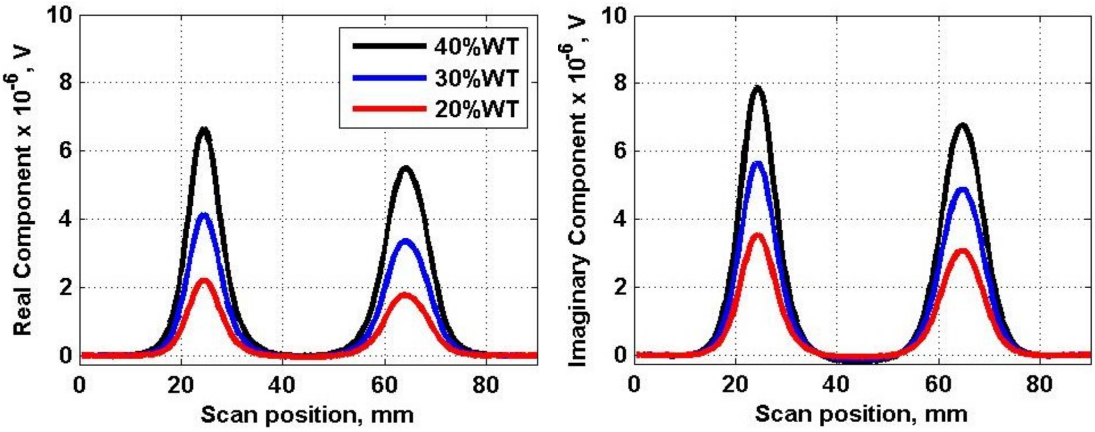

Figure 3.10 Model predicted RFEC signals of 20%, 30% and 40% WT grooves in the tube.

3.9 Development of RFEC instrumentation

The nonlinear model could be successfully used to study the RFEC behavior in modified 9Cr-1Mo SG tubes and optimize the spacing and frequency. Further RFEC signals of wall thinning grooves could be predicted. To validate the model predictions and assesses the sensitivity of the RFEC technique, experimental measurements have been carried out. This section discusses the details of the high sensitive instrument developed and experimental measurements carried out on standard defects. The overall schematic of the RFEC instrument developed is shown in Figure 3.11.

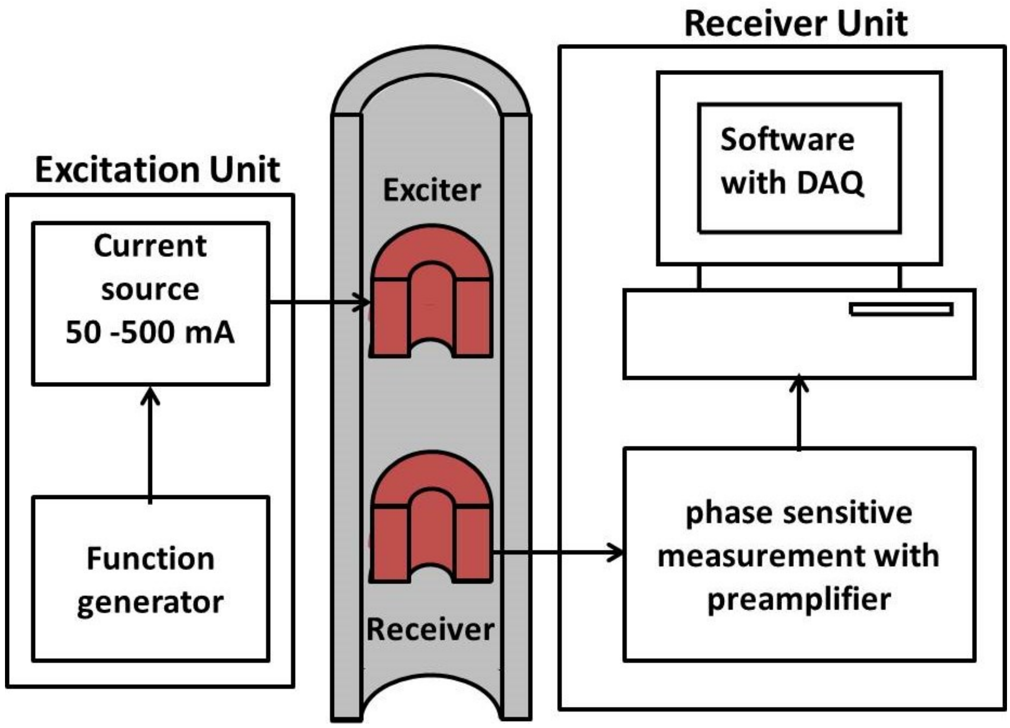

Figure 3.11 Schematic of the RFEC instrument.

There are two main modules in the instrument namely: the excitation unit and the receiver unit. The excitation unit essentially consists of a constant current, sine wave oscillator while the receiver unit consists of an instrument for the measurement of amplitude and phase of the feeble induced voltages in the receiver coil in mv to μv range. The constant current source should be free from harmonic contents and intrinsic noise. The source should also have high stability for a set-value of the current. Similarly the receiver unit is should be capable of measuring feeble signals in the receiver coil of the RFEC probe which are buried in noise.

3.9.1 Excitation unit

The excitation unit consists of a function generator and a constant current source. The function generator produces a sinusoidal voltage waveform at a desired frequency. The frequency bandwidth of the source is 10Hz-2 kHz. The constant current source is essentially a voltage to current converter which converts the voltage waveform generated by the function generator into current waveform. The source maintains a set value of the current based on real time control system logic as schematically shown in Figure 3.12.

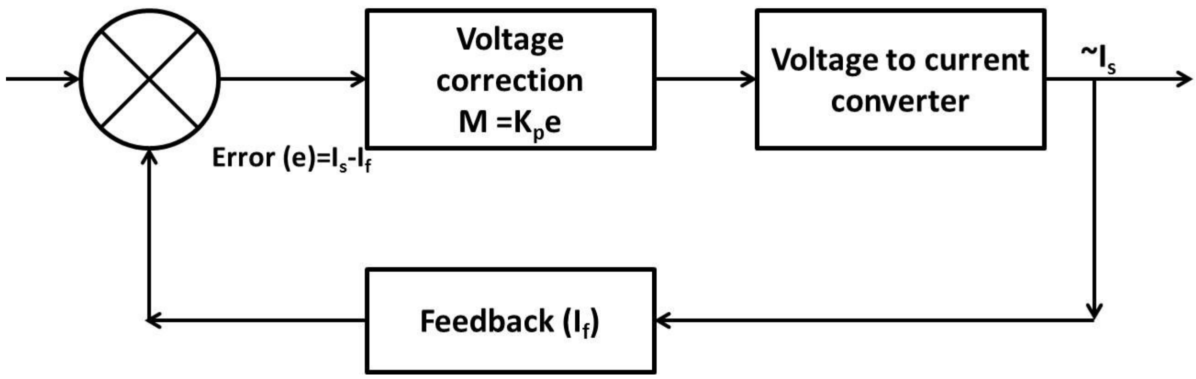

Figure 3.12 Control system logic of the current source.

In this logic, the current driven into the coil is constantly measured and whenever there is an increase/decrease in the current with respect to the set value, it increases/decreases the voltage proportional to the difference between the measured and the set value, till the desired current is achieved. It is a closed loop, negative feedback proportional controller as shown in Figure 3.12. The negative feedback has the advantages of less distortion and high bandwidth.

A quantitative estimate of the harmonic contents of the current waveform has been measured by the total harmonic distortion (THD) parameter, which is defined as the ratio of the sum of the powers of all harmonic components to the power of the fundamental frequency as shown in the equation given below:

$$THD\% = \frac{P_2+P_3+P_4+\cdots P_\infty}{P_1} \times 100 \qquad \ldots 3.20$$

The powers of the harmonic components of the waveform were evaluated by computing the power spectral density through fast Fourier transform. The measured THD% of the current source was less than 1% when the source was not connected to any load and less than 3% when it was connected to a 40 ohm inductive load at a frequency of 1000 Hz. Repetitive measurement of the current for longer duration indicated that the current value was steady at a set value and no drift was observed in the current value, when the current source was connected to 40 ohm inductive load at a frequency of 1000 Hz and the current value was set at 100 mA. For all the practical purposes, a 100 mA current was set to drive the excitation coil of the RFEC probe to reduce the heating of the coil.

3.9.2 Receiver unit

The receiver circuit measures the amplitude and phase of the induced voltage in the receiver coil. The receiver coil signal is influenced by noise from various sources. As the excitation sine wave travels through the tube wall and along the outer surface of the tube, it is highly attenuated before it reaches the receiver coil and also influenced by the variations in material properties such as the permeability that produce high frequency noise. For measuring feeble response (usually of the order of μV as predicted by the FE model) buried in the noise, a lock-in amplifier based receiver unit was developed.

The lock-in amplifier measures the amplitude and phase of a sinusoid with respect to reference sinusoid [85]. It locks the frequency of the sinusoids which matches the reference frequency, thereby acting as a narrow band pass filter with a bandwidth of the order of mHz. A schematic working of the lock-in amplifier is shown in Figure 3.13. In this, the amplitude 'A' and the phase angle 'θ' of a input sine wave of angular frequency ω_s, to be measured with respect to a reference sine wave whose angular frequency ω_R. The phase locked loop (PLL) block measures the frequency of the reference sine wave and generates orthogonal sine and cosine components. These two waves are individually multiplied with the input sine wave. The resulting components have additive and subtractive frequency terms in sine and cosine as shown in Figure 3.13. When there is match in the reference frequency and input sine wave frequency, the additive terms gives higher frequency components and the subtractive terms provide DC components. The higher frequency components can be filtered using a low pass filter to obtain the DC components X and Y. These DC components are the in-phase (X) and quadrature (Y) components of the receiver coil induced voltage. The Amplitude (A) and the phase (θ) are calculated from the measured in-phase and quadrature components. The resulting output would be free from high as well as low frequency noise as only the components corresponding to the reference sine wave are selectively processed and measured.

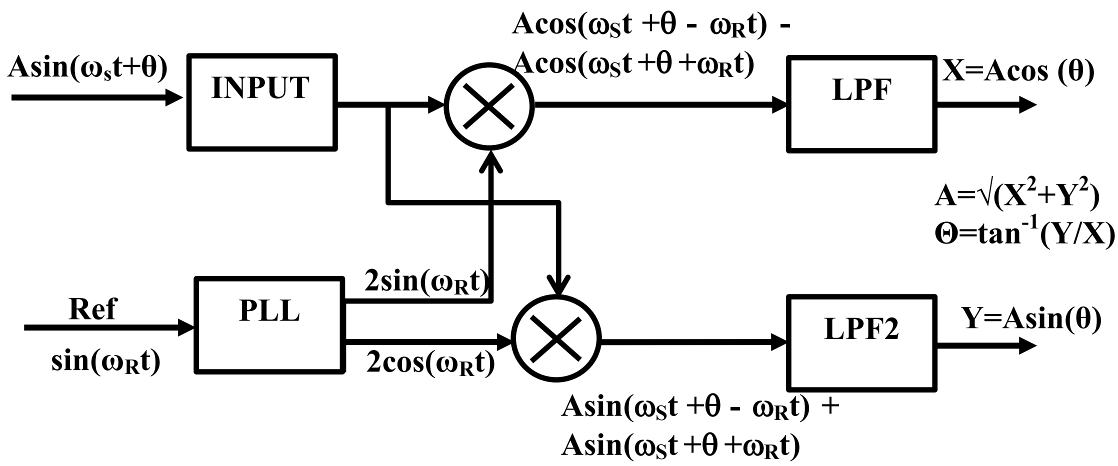

Figure 3.13 Schematic of the lock-in amplifier.

A dual channel lock-in amplifier with a built-in preamplifier (M/s. Ametek Advanced Measurement Technology), operating in the frequency bandwidth of 10 Hz - 250 kHz was used. The lock-in amplifier provides the analog output of either X and Y or A and θ. The in-phase and quadrature components from the lock-in amplifier output were acquired using a computer controlled data acquisition (DAQ) system.

The DAQ system used an analog-to-digital (A/D) converter with high dynamic range (16 bit) and sampling rate (250 kSa/s). A front end graphical user interface (GUI) was developed using MATLAB software. The GUI has display and processing modules. The display module contains the real-time display of complex plane as well as time domain RFEC signals. Gain and phase controls are provided in the GUI to describe magnification and to rotate phase angle of the signals in the complex plane in steps of 0.1 degree. The processing module contains circuit null balance action, display clear signals using dynamic time warping based baseline or trend removal algorithm. Figure 3.14 shows the photograph of the RFEC instrument.

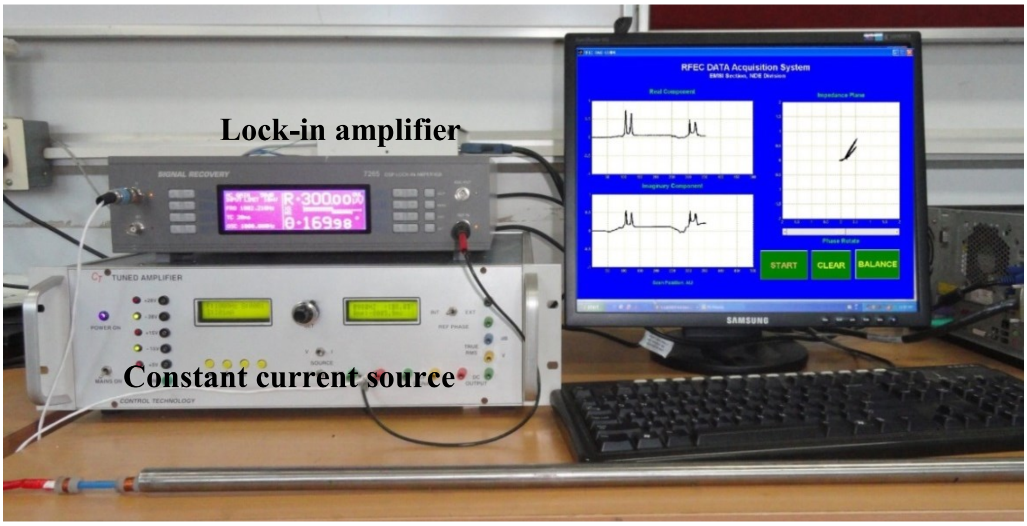

Figure 3.14 RFEC instrument and computer controlled data acquisition system.

3.10 Development of RFEC probe

An RFEC probe with exciter and receiver coil was fabricated with dimensions optimized by using the FE model. The spacing between the exciter and receiver was maintained at the optimum distance of 36 mm. Table 3.4 shows the parameters of the exciter and receiver coils. Non-conducting Nylon or Teflon was used as the material for the probe former. The effective length of the probe including the exciter and receiver coils is 47.5 mm. Detailed CAD simulation was carried out and found that slotted probe with 47.5 mm length negotiate the expansion bend regions of the SG tubes. Studies also showed that single piece of 47.5 mm nylon material having an OD of 11.7 mm could not pass through the bend regions. Alternate slots have been made in the region between the exciter and receiver coils as shown in Figure 3.15 (a) to make the probe flexible enough to move through the bend regions. Figure 3.15 (b) shows the photograph of this flexible RFEC probe head with 30 m cable.

Table 3.4 Design parameters of the RFEC probe.

S. No	Parameters	Exciter coil	Receiver coil
1	Former Material	Nylon/Teflon	Nylon/Teflon
2	Outer diameter	11.7 mm	11.7 mm
3	Inner diameter	2.7 mm	2.7 mm
4	Length	7.5 mm	5 mm
5	Number of turns	400	200
6	Copper wire gauge	36 SWG	36 SWG

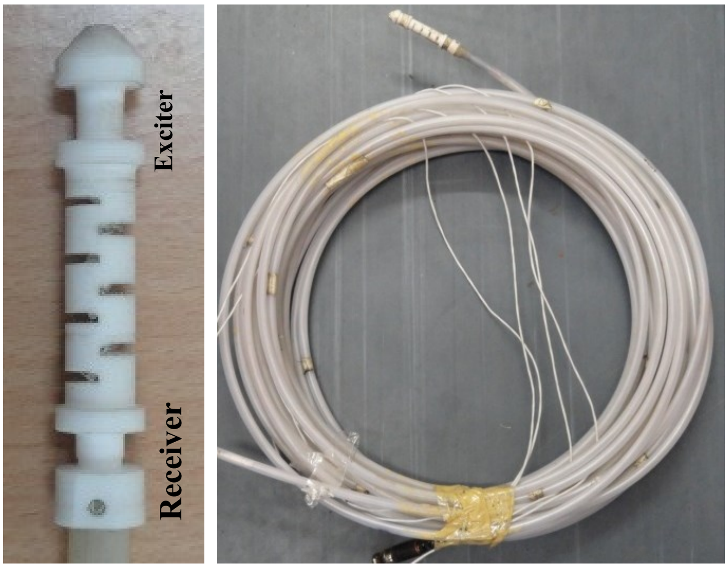

(a) (b)

Figure 3.15 Flexible RFEC probe developed for negotiation of bend regions in SG tubes.

3.11 Performance evaluation

In order to demonstrate the performance of the RFEC instrument, calibration tube with artificial defects as per the ASME standard, Section V, Article 17 was fabricated. Article 17 recommends the use of 5 mm diameter flat bottom holes (FBH) of different depths to simulate pits in tubes. In addition to FBH, a circumferential groove and a partial groove of 3 mm width were also machined in the calibration tube. A separation distance of 200 mm between calibration defects was maintained to ensure that the defects are non-interacting. Figure 3.16 shows the schematic of the calibration tube as per ASME with reference defects. Figure 3.17 shows the in-phase (real) and quadrature (imaginary) components of the RFEC signals from the calibration tube measured using the developed instrument.

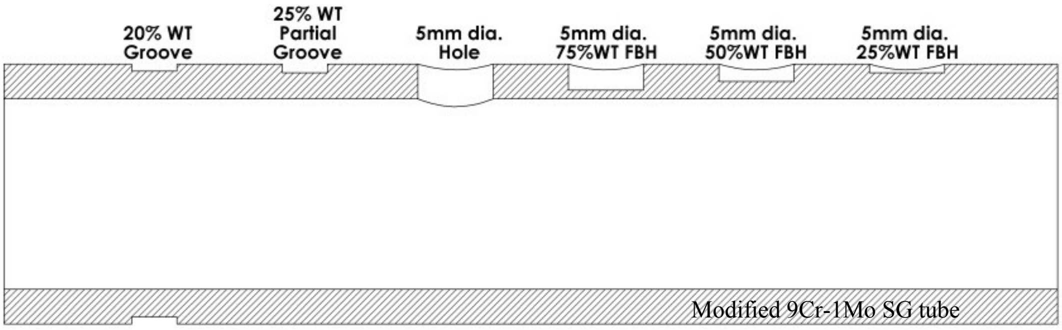

Figure 3.16 Schematic of the calibration tube with reference defects.

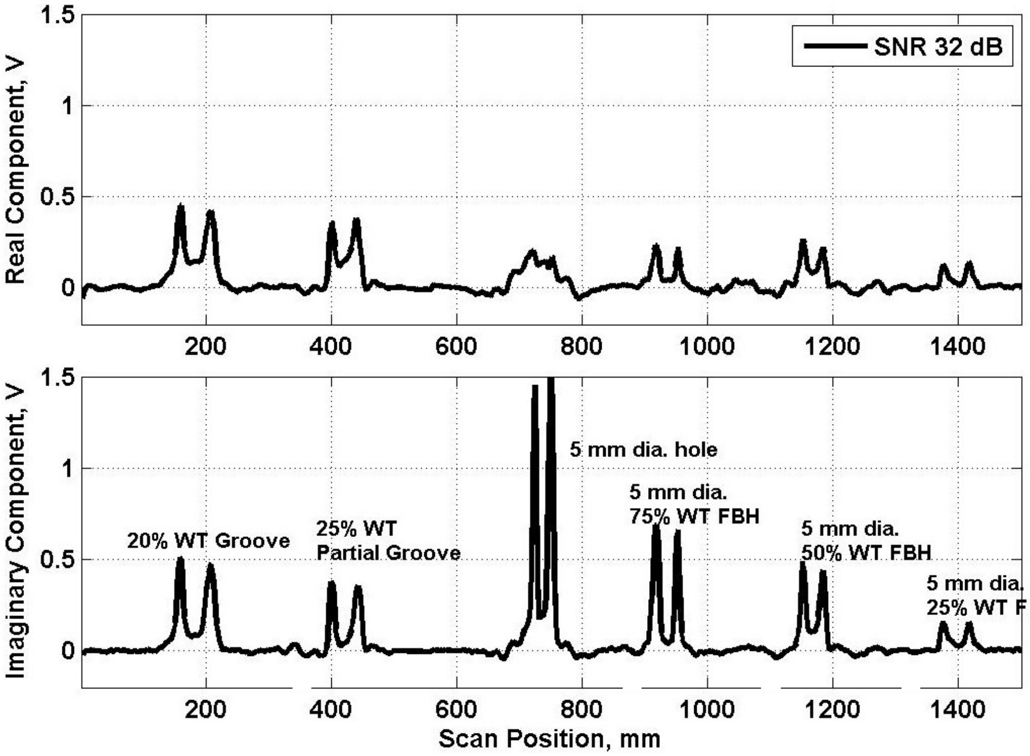

Figure 3.17 Experimentally measured real and imaginary components of the RFEC signals (at 825 Hz) of reference defects as per ASME Section V Article.17.

In order to assess the detection performance, signal and noise amplitudes were measured and the SNR was determined using

$$SNR = 20 \times log\frac{S}{N} \quad ...\ 3.21$$

where S is the amplitude of RFEC signal of a defect and N is the amplitude of RFEC signal in defect-free region of tube (noise). The SNR for 40% depth FBH has been found to be 32 dB. Whereas, the SNR of the same FBH obtained using a bridge circuit based commercial eddy current instrument operated in send-receive mode was found to be only 3 dB.

3.12 Experimental validation of the model predictions

For validation of the model predictions, RFEC signals of wall thinning grooves were experimentally obtained at 825 Hz using a RFEC probe fabricated as per the model optimized dimensions (refer Section 3.8.1). Grooves of width 3 mm and depths 0.46 mm (20% WT), 0.69 mm (30% WT) and 0.92 mm (40% WT) were machined in a SG tube using EDM. Figure 3.18 shows the experimentally obtained signals for the grooves. Comparison of Figure 3.10 and Figure 3.18 reveals that the model predictions and the experimental measurements are qualitatively in good agreement with each other. However, there is a large difference in the exact values between them. This difference is due to several factors that are not modeled and these include: gain setting, instrument transfer function characteristics and minor variations in the coil dimensions, material conductivity and spacing between the exciter and receiver coils.

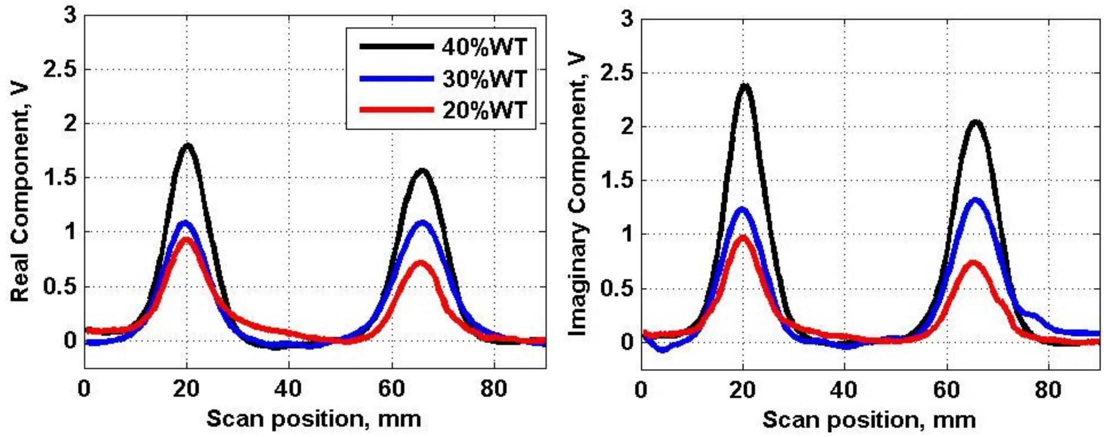

Figure 3.18 Experimentally measured RFEC signals of 0.46 mm (20% WT), 0.69 mm (30% WT) and 0.92 mm (40% WT) deep grooves in SG tube.

A transfer function approach was adopted to address the above important factors that are not considered in the FE model [86,87]. The transfer function for this case is determined based on the matrix inversion method. Let d_{exp} and d_{mod} are experimentally measured and the model predicted RFEC signals respectively. Then, the transfer function matrix (T) is obtained in the following manner:

$$T \times d_{mod} = d_{exp} \qquad \text{... 3.22}$$

$$T = d_{exp} \times d_{mod}^{-1} \qquad \text{... 3.23}$$

Singular value decomposition based pseudo inverse was used to obtain the inverse of d_{mod} matrix. The elements of the d_{mod} and d_{exp} matrices were complex with real and imaginary parts of the RFEC signals. The transfer function (T) was initially obtained using the experimental and model predicted RFEC signals of 40% WT deep groove. This transfer function was then applied to 30% and 20% WT deep grooves. Figure 3.19 shows the model predicted and experimental RFEC signals after applying the transfer function matrix to the model predicted signals. A very good agreement is seen between the model predictions and experimental measurements. The percentage relative error between the model and experimental signals was found to be less than 5%. Hence, the model predictions, from now on, would be subjected to this transfer function to compare with the experimental measurements.

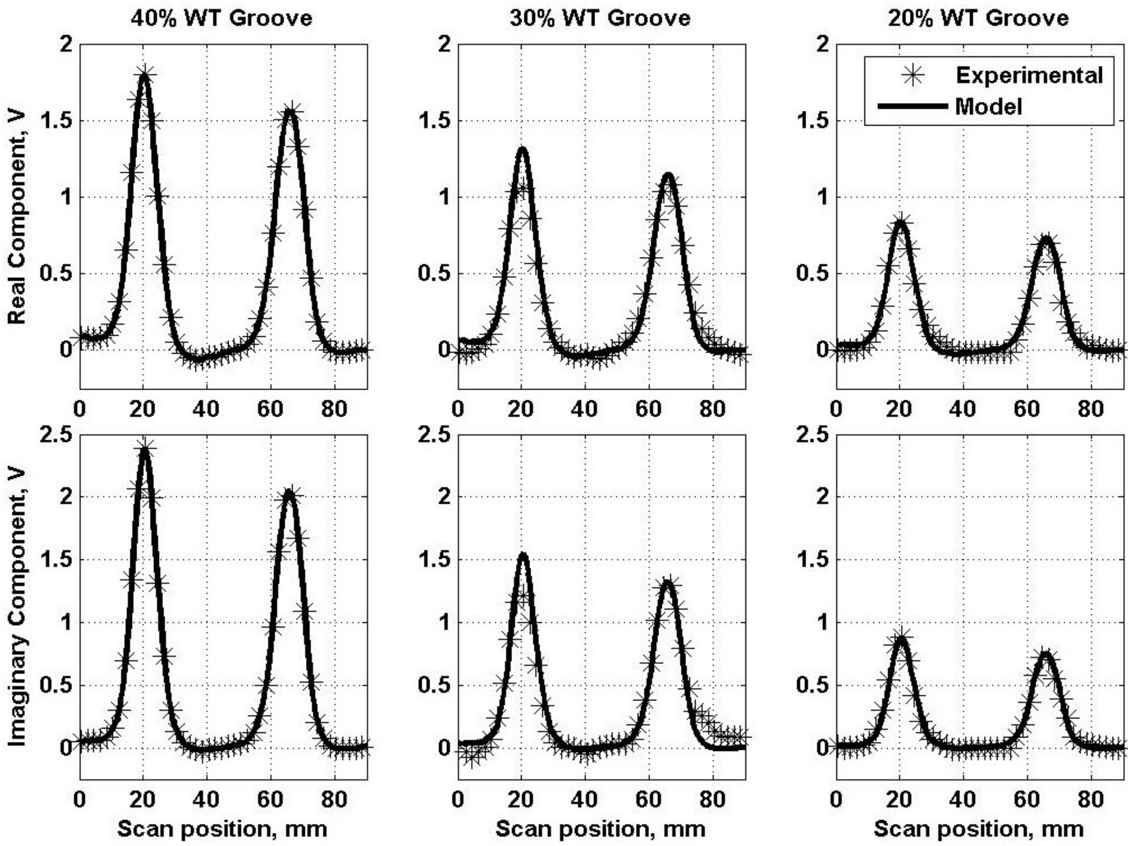

Figure 3.19 Measured and model predicted RFEC signals.

In order to study the difference between the linear and nonlinear models, the linear model predicted RFEC signals of 20%, 30% and 40% WT grooves were compared with the experimental measurements as it was done for the nonlinear model. Figure 3.20 shows the linear model predicted and experimental RFEC signals after applying the same transfer function matrix to the linear model predicted signals. As can be seen a large deviation is observed in the predictions of imaginary component of the RFEC signals with an error higher than 50%. This confirms the fact that the nonlinear model predictions are correct and reliable.

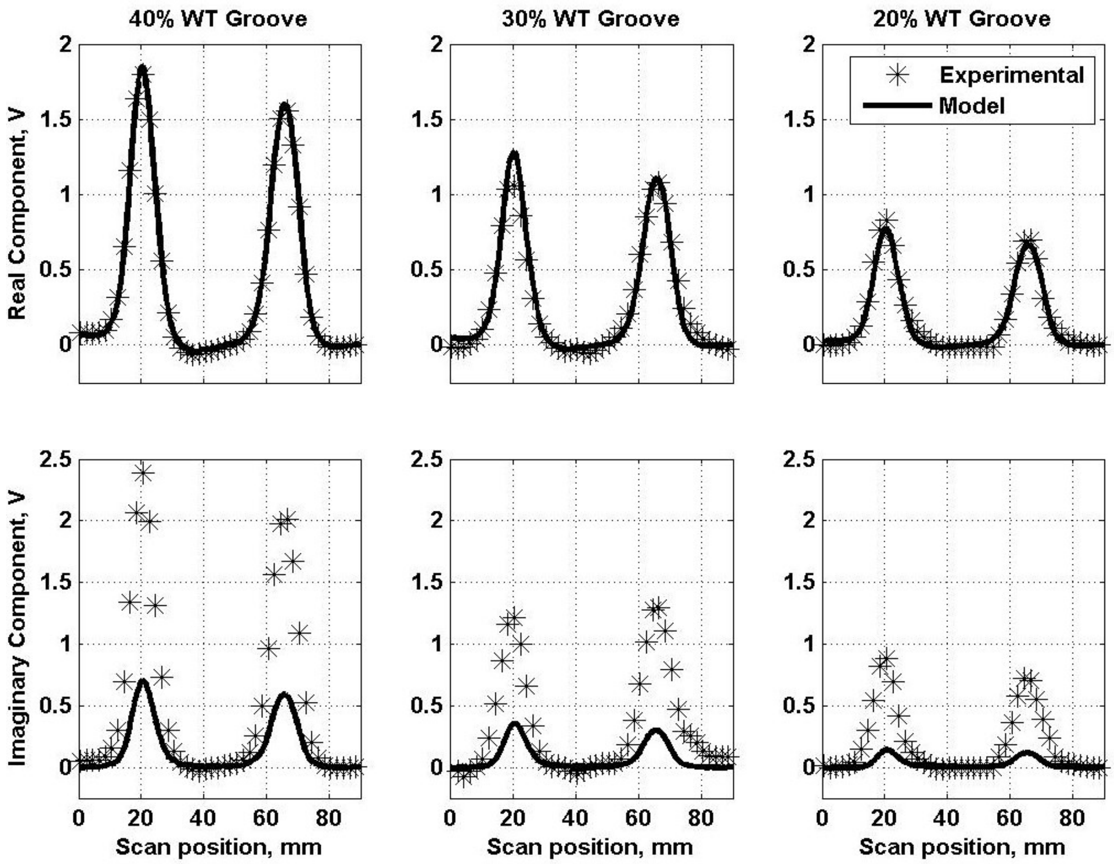

Figure 3.20 Measured and linear model predicted RFEC signals.

3.13 Discussion

When performing the nonlinear FE modeling, we define the excitation current in the coil. This current would correspond to a particular value of magnetization (H), and would fix an operating point on the BH curve (refer Figure 3.1). The nonlinear model predicts magnetic flux density corresponding to this magnetic field of the BH curve. But, in the case of a linear model a constant relative permeability is defined which essentially assumes a monotonic increase in B with H (applied excitation current), which is not practically feasible. The nonlinear model simulates the practical condition with the given BH curve. This advantage of the nonlinear model can be demonstrated by considering the RFEC signal amplitude of a defect obtained at different excitation currents for both linear and nonlinear models. For this demonstration purpose, the 3 mm width, 0.46 mm (20% WT) deep groove is considered. In the linear model a constant relative permeability of μ_r=100 has been chosen. Figure 3.21 shows the RFEC signal amplitude at different excitation currents for the linear and nonlinear models. As shown in the Figure 3.21, the RFEC amplitude of linear and nonlinear models is different for excitation current beyond 0.15 A. The RFEC signal amplitude of the groove increases monotonically with increase in the excitation current, but the nonlinear model shows saturation behavior, as it incorporates the BH characteristics. Table 3.5 shows the amplitude values for the groove by linear and nonlinear models and the difference. The difference between the linear and nonlinear models is minimum at lower excitation currents and increases with the excitation current which essentially shifts the operating point on the BH curve. Hence, the linear models tend to be erroneous at higher excitation currents, which is not the case with the nonlinear model. These results are in good agreement with those reported by Ostermeyer [43]. Thus, it appears that the FE model addresses the nonlinear variation in the material property in a better manner.

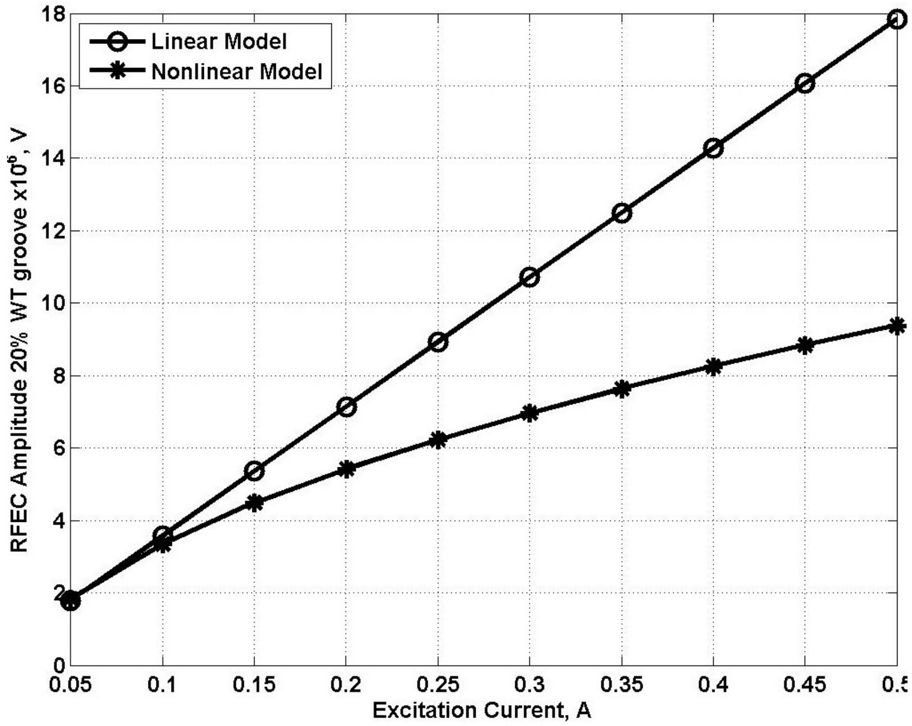

Figure 3.21 Comparative behavior of linear and nonlinear models.

Table 3.5 Comparsion linear and nonlinear model predicted RFEC amplitudes of a 20% WT deep groove.

S. No.	Excitation current, mA	Linear model predicted amplitude (L) $x10^{-6}$ V	Nonlinear model predicted amplitude (NL) x 10^{-6} V	Difference (L – NL) x 10^{-6} V
1	50	1.78	1.83	-0.05
2	100	3.57	3.34	0.23
3	150	5.35	4.48	0.87
4	200	7.14	5.41	1.73
5	250	8.92	6.22	2.70
6	300	10.70	6.96	3.74
7	350	12.50	7.63	4.87
8	400	14.28	8.25	6.03
9	450	16.06	8.83	7.23
10	500	17.84	9.38	8.46

The nonlinear model in 2D axi-symmetric case could be implemented without much additional cost on the computational resources and time, in comparison to an equivalent linear model and hence, advantageous in implementation of the same. Thus, the study reveals that nonlinear modeling is beneficial.

The optimum frequency reported in this study is based on groove type of defects. However, the optimum frequency is expected to be marginally different, when different types of defects are considered. This is very much true when ID defects are considered instead of OD defects. In view of this, when optimizing the frequency, it is suggested to consider the minimum size defect that should be practically detected by the technique either in OD or ID side of the tube. It is also interesting to note that the optimum frequency of 825 Hz reported in this study is on the higher side, as compared to the reported values of the literature for carbon steel pipes and tubes, which are usually less than 200 Hz. This is attributed to the thin walled nature of the SG tube considered in this study and to higher permeability of the carbon steel.

3.14 Summary

1. Complex effective permeability based nonlinear finite element modeling was carried out to study the RFEC technique in small diameter thin ferromagnetic SG tube. The experimentally measured BH curve of SG tube was provided as input to the model. Implementation of this kind of model to study the RFEC behavior in steel tubes is the first of its kind.
2. The arrow and surface plot of the magnetic field and flux density clearly depicted the RFEC characteristics such as amplitude valley and phase knots in SG tubes and these results are in good agreement with the reported literature.

3. The RFEC region could be accurately identified based on the deviation in the linear behavior of the logarithm of induced voltage in the receiver coil with axial distance. The nonlinear model predicted the RFEC region beyond 36 mm with respect to the center of the excitation coil for the SG tubes of interest.
4. The frequency was optimized based on the maximum amplitude of RFEC signal observed for grooves (width 3 mm and depth 10% WT, 20% WT, and 30% WT). An operating frequency of 825 Hz was considered to be optimum for high sensitive detection of defects in SG tubes.
5. A stable, noise-free, constant current excitation source with THD less than 3% was designed and developed for driving the exciter coil of the RFEC probe. Lock-in amplifier based high sensitive receiver unit with high dynamic range data acquisition system was realized for measuring the small amplitude receiver coil voltages. A dedicated graphical user interface was developed for viewing of signals and for post processing.
6. Flexible RFEC probe has been designed and developed as per the model predictions and operated at the optimized frequency of 825 Hz. The RFEC probe and instrument could detect OD defects as small as 5 mm diameter and 25% WT deep.
7. The model predictions were found to be qualitatively in good agreement with the experimental measurements. A transfer function approach was used to validate the model predictions with the measured results. The difference between the model and measured results was found to be less than 5%.

Chapter 4: Signal processing approach for NDE of bend region

4.1 Introduction

This chapter covers the results of the detection of different types of defects such as grooves, flat bottom holes and notches in the straight sections of the SG tube. It highlights the issues with the detection of defects in the bend regions and presents digital signal processing techniques for the elimination strong disturbing noise from the bend regions to enable detection of defects.

4.2 Detection of defects in the straight section of SG tube

Apart from the standard defects as per ASME discussed in Section 3.11, grooves, flat bottom holes (FBHs), axial and circumferential notch type of defects were machined in SG tubes to study the detection sensitivity of the instrument and probe for detection of defects in the straight sections of the SG tubes. Figure 4.1shows the RFEC signals of the grooves of 3 mm width having the depths of 0.46 mm (20% WT), 0.69 mm (30% WT), and 0.92 mm (40%WT). The RFEC instrument is capable of detecting all the grooves with an SNR greater than 32 dB. Figure 4.2 shows the RFEC signals of flat bottom holes of different depths starting from 20% WT depth. Careful observation of the figure reveals that the amplitude of the 20% WT deep FBH is nearly 2 orders less than the amplitude of the groove of same depth. It is also interesting to note that the double peak behavior of the RFEC signals exist for the localized defects. This has been attributed to synergistic effect of optimized probe and high sensitive lock-in amplifier based instrument.

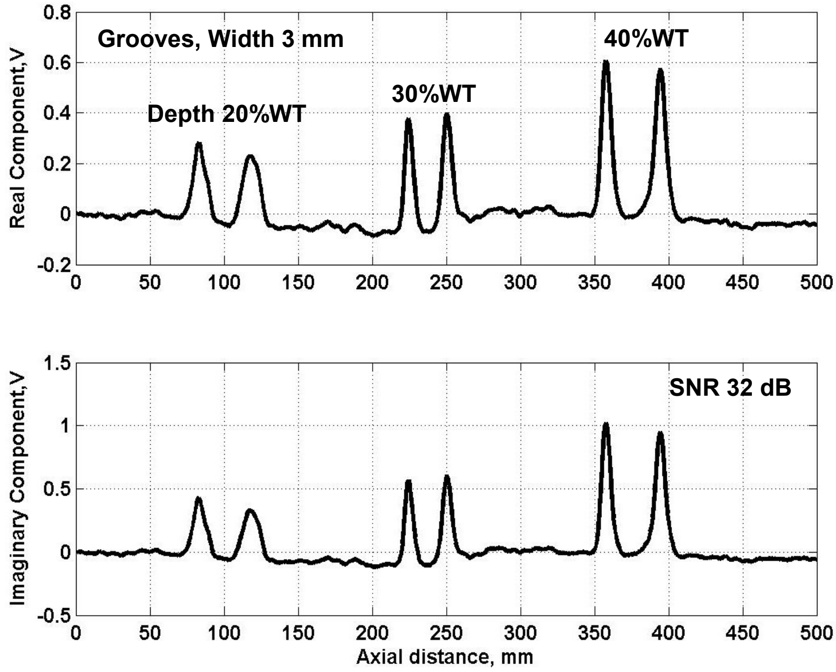

Figure 4.1 RFEC signals for grooves of 3 mm width at 825 Hz.

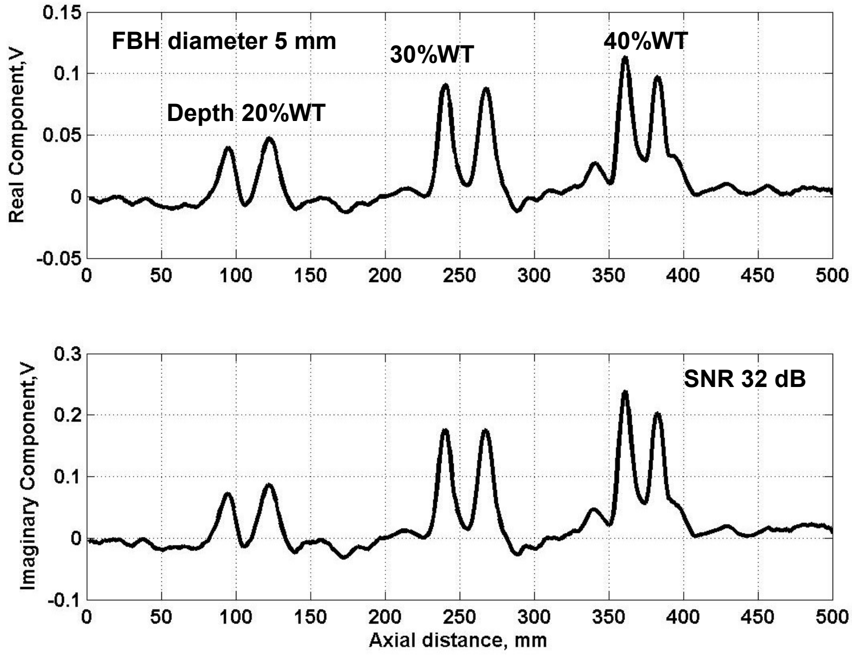

Figure 4.2 RFEC signals for 5 mm diameter flat bottom holes of different depths.

Figure 4.3 and Figure 4.4 show the RFEC signals of notches of same size oriented in axial and circumferential directions respectively. As can be observed, both the 20% WT deep defects could be reliably detected by the RFEC instrument and probe. Here also the double peak behavior is noticed. As expected the axial notches are extended in nature and the circumferential notches are highly localized, mainly due to their orientation. It should also be noted that the amplitude of axial and circumferential notches of same depths are nearly equal. This is mainly due to the size of the receiver coil, which is able to receive equal amounts of magnetic flux from the notches.

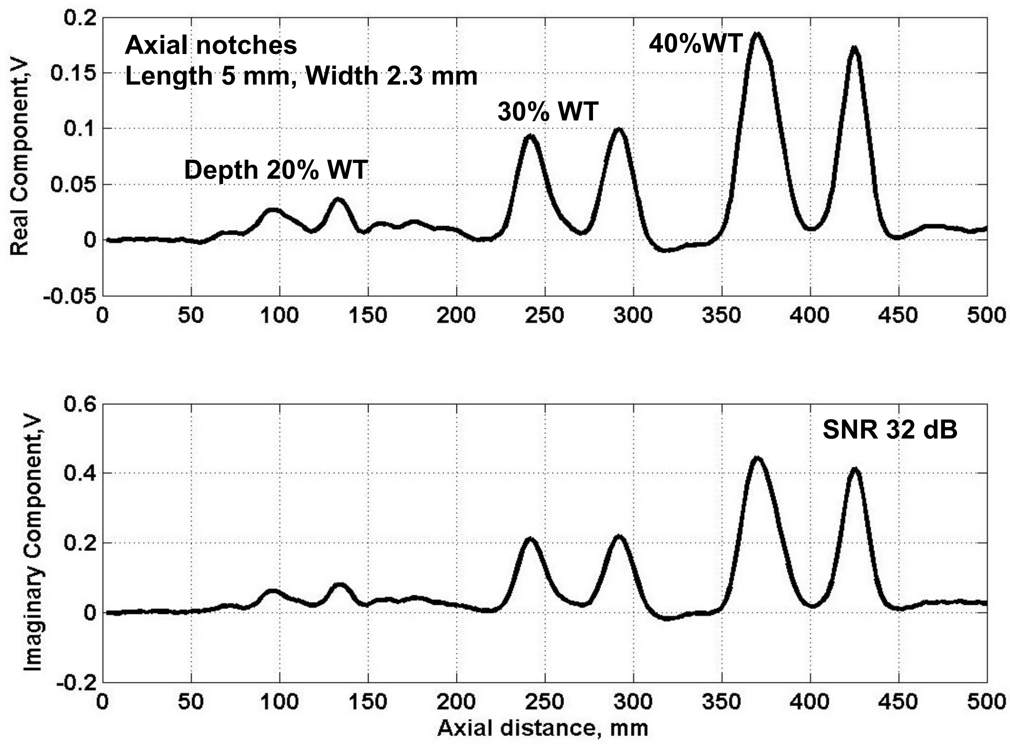

Figure 4.3 RFEC signals of 5 mm length, 2.3 mm width axial notches of different depths.

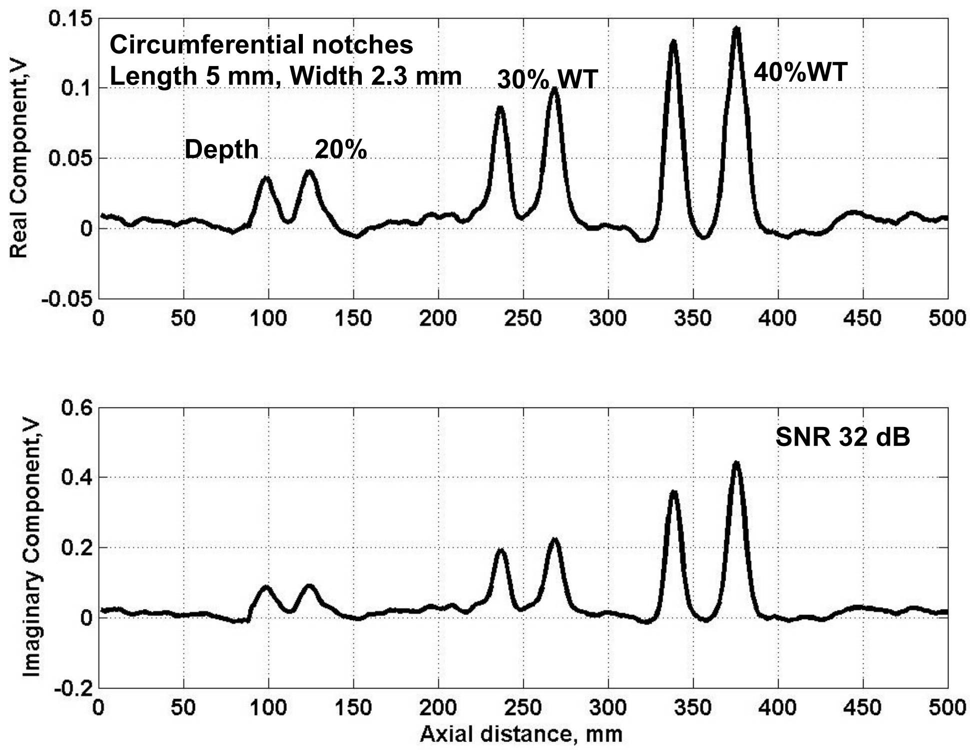

Figure 4.4 RFEC signals of 5 mm length, 2.3 mm width circumferntial notches of different depths.

Good detection sensitivity for localized defects such as FBH and notches (axial and circumferential) could be achieved in the straight sections of the SG tubes. Localized defects whose depth as small as 20% WT could be reliably detected using the optimized probe and the RFEC instrument developed as part of this research work.

4.3 Issues with detection of defects in the bend regions of SG tubes

Detection of defects in the bend regions of the SG tubes is limited by several disturbing variables such as exciter-receiver coil misalignment, permeability, probe wobble and stresses due to bending, as discussed in Chapter 2. Figure 4.5 shows the typical RFEC signals of 3 mm width 20% WT deep grooves at three characteristic locations of the bend regions (denoted as D1, D2, and D3 in the figure). A shift in the baseline has been observed in the RFEC signals. A distinct double-peak signal is observed only for groove D1, while the RFEC signals of the other grooves are seen merged with high-amplitude low-frequency noise. The SNR is negative, because, the noise amplitude is higher than the signal amplitude. Detection of these grooves by simple threshold is difficult. Hence, it is essential to improve the SNR for detection of defects in the bend regions.

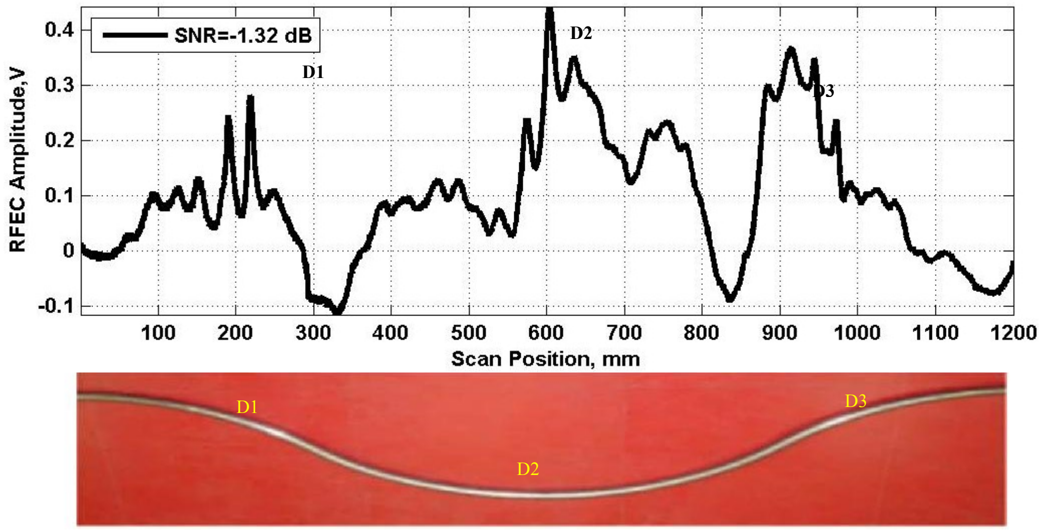

Figure 4.5 Typical RFEC signals from the bend regions of the SG tube having grooves at three characteristic locations and the photograph of the bend tube.

The RFEC response due to misalignment of coils, bending stresses and probe wobble are of low-frequency and extended in nature and contribute to the shift in the baseline as observed in Figure 4.5. The RFEC response due to permeability variations are relatively of higher frequency and distributed. On the contrary, the RFEC response for wall loss defects would be highly localized and are of intermediate frequencies, depending on the type and size of the defects. This frequency characteristic of the noise and the RFEC signals can be fruitfully utilized to selectively remove the unwanted information in the frequency domain. Thus, processing of RFEC signals based on frequency domain filtering seems promising for noise reduction.

The unique double peak RFEC signals of defects can be conveniently used to design a template for cross-correlation and also to choose a mother wavelet for signal enhancement enabling reliable detection of defects in the presence of disturbing noise. In this study, frequency domain filtering, template based cross correlation and wavelet transform based processing techniques have been studied and the noise reduction and signal enhancement characteristics of these techniques have been compared. The signal processing algorithms have been implemented on the amplitude of the RFEC signals of artificial grooves in the bend regions.

4.4 Signal processing techniques

This section describes the basic concepts of Fourier filtering, cross correlation and wavelet transform based digital signal processing techniques for eliminating the disturbing noise from the bend regions of the SG tube to enable detection of defects.

4.4.1 Fourier filtering technique

Fourier filtering technique is useful for elimination of one or more unwanted frequency components (noise) of a discrete time signal, when they are known *a priori* [88]. Fourier transform is a frequency domain representation of a time domain signals *x(t)*. The Fourier transform of a discrete time domain signal *x(t)* is computed using the following equation:

$$x(k) = \sum_{n=0}^{N-1} x(n) e^{-\left[\frac{i2\pi nk}{N}\right]} \quad \text{... 4.1}$$

Direct computation of equation (5.2) for an n-point time series data would involve $O(n^3)$ computations. The discrete Fourier transform algorithms reduce the number of computation to $O(n^2)$ [89]. But, in the Fast Fourier transform (FFT) algorithm which is widely used, the computations can further be reduced to $O(n\log_2 n)$. This means: as the number of data points becomes large, the computations are also reduced proportionately as compared to the discrete Fourier transform algorithm. FFT has been used in this study for designing a frequency filter for removing the frequency components that correspond to the noise from bend regions, and then for reconstructing the signal using the inverse FFT.

As the signals of the machined defects and the noise due to disturbing variables were unique and expected to be of different frequencies, Fourier band-pass filtering was applied to RFEC signals of tubes. However, the frequency characteristic of the disturbing noise from the bend regions was not known *a priori*, to selectively remove them. Hence, the cut off frequencies were identified heuristically. The SNR was analyzed at different upper and lower cut-off frequencies for optimizing the bandwidth of the band-pass filter.

4.4.2 Cross-correlation technique

Correlation between two signals is a measure of the degree of similarity between them. The cross-correlation function, $R_{xy}(l)$ of two discrete time domain signals x and y is given by

$$R_{xy}(l) = \sum_{-\infty}^{\infty} x(n)y(n-l) \qquad \text{... 4.2}$$

where l is lag or shift of y in the time with respect to x. In other words, the signal y, called a template, is shifted by l samples with respect to signal x and multiplied such that the cross- correlation function becomes large at points where the two signals have greatest similarity [88]. The RFEC signal of a localized defect shows two peaks and the distance between the peaks depends on the dimensions of the coils and distance between them. The distance between the peaks and the peak amplitude of the template signal are important. Thus, by using the double-peak signal as a template, the cross-correlation function of RFEC signal from bend regions is expected to increase when a defect is present in the RFEC signal. It may be desirable to use the RFEC signal from an artificial notch or natural defect in SG tube as template. In the study, the signal of 20% wall loss groove from straight portion of a SG tube has been used as the template and the cross-correlation function has been determined.

4.4.3 Wavelet transform technique

Wavelet transform is a signal processing technique that allows a signal of interest to be examined in both time and frequency domains simultaneously [90,91,92,93]. The continuous wavelet transform (CWT) of a time domain signal x(t) is defined as

$$X_w(s,b) = \frac{1}{\sqrt{s}}\int_{-\infty}^{\infty} x(t)\psi^*\left(\frac{t-b}{s}\right)dt \qquad \text{... 4.3}$$

where $\psi(t)$ is the mother wavelet which is a continuous function in both, time and frequency domains, b is the translation factor that depends on time, and s is the scale factor which is a function of frequency. Daughter wavelets are derived from the mother wavelet by varying the scaling factor. Thus, the frequency bandwidths of daughter wavelets are different from each other. The CWT coefficients $X_w(s,b)$ are obtained by cross-correlation of $x(t)$ with different daughter wavelets. The time frequency localization property of the wavelets enables one to use them as band-pass filters at the bandwidth of the wavelet.

Selection of the mother wavelet is important and is usually done such that its shape resembles the shape of the desired feature of a signal. As the shape of the RFEC signal of a defect is typically double-peaked, Gaussian like wavelets such as 2nd derivative of Gaussian (Gaus2), Mexican hat (Mexh), Biorthoganal (Bior2.8) and Daubechies (DB5) have been used as the mother wavelets. Figure 4.6 shows the shape of these wavelets.

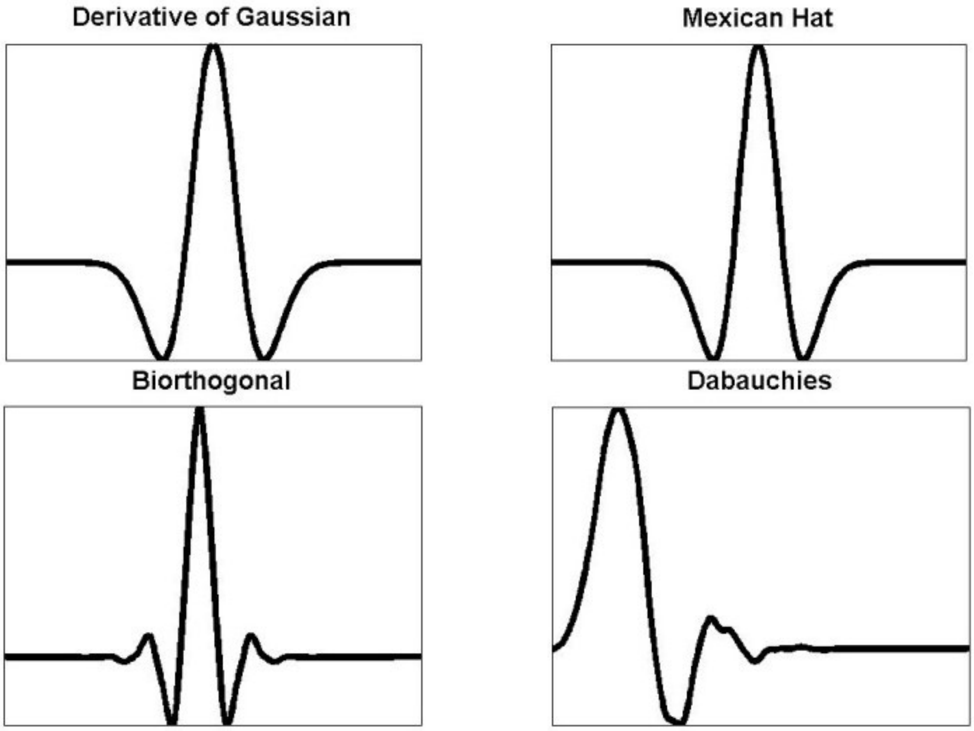

Figure 4.6 Different wavelets considered for processing of the RFEC signals.

In view of the well-known band-pass characteristic of the wavelet transforms, the as-received (raw) RFEC signals of tubes were used instead of the Fourier filtered signals. The CWT spectrograms of RFEC signals have been generated for these wavelets at different scale factors. It must be noted here that too high scaling factors would extract the slowly varying disturbing noise from misalignment and bending stresses while too low scaling factor would draw out the rapidly changing magnetic permeability noise. Thus, for the problem at hand it is preferred to identify an optimal intermediate scale factor for the wavelets. The wavelet with a scale factor that showed high SNR while retaining the double-peak behavior of the RFEC signals was chosen as optimum.

4.5 Experimental measurements in bend regions of SG tube

In this study machined grooves as well as localized defects such as notches and holes were used for comparing the performance of the signal processing techniques. Four modified 9Cr-1Mo tubes viz. T1, T2, T3 and T4 have been taken and expansion bends with same dimensions as that of the SG tubes have been fabricated by special bending rig. In two tubes (T2 and T3), three external grooves (width 3 mm) of same depth in each tube were machined at characteristic transition locations viz. straight-to-bend, bend-to-bend and bend-to-straight regions. As shown in Figure 4.7, grooves D1 and D3 were introduced in the straight-to-bend transition regions and groove D2 has been introduced in the bend-to-bend transition region.

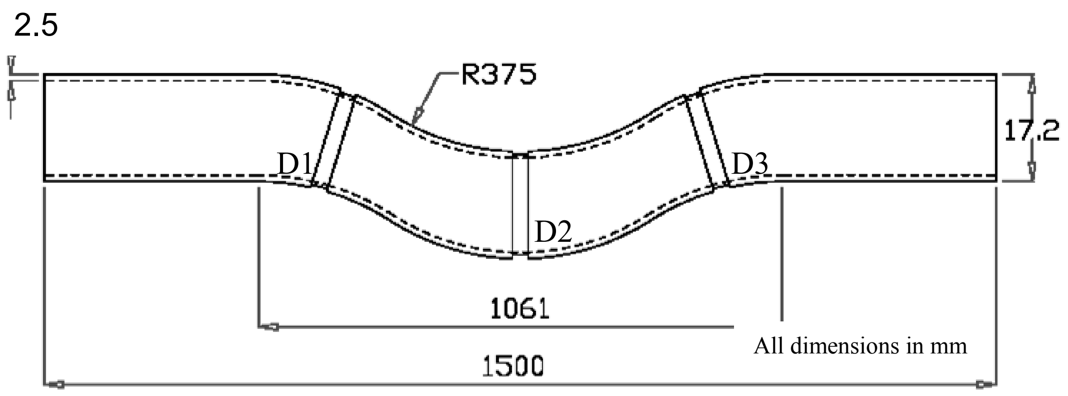

Figure 4.7 Schematic of SG tube with grooves D1, D2 and D3 in the bend region.

The depth of the three grooves in tube T2 was 10% of wall thickness (WT) while it was 20% WT in tube T3. In tube T4, a hole (diameter, 2 mm) and a circumferential notch (length 5 mm, width 1.5 mm and depth 1.15 mm) have been machined in the bend-to-straight regions. In tube T1 *i.e.* the tube that has maximum disturbing noise during RFEC preliminary studies among all the four tubes, no artificial defect were introduced. Table 4.1provides the details of the machined grooves used for the study.

Table 4.1 Details of the artificial defects made in the bend regions of the SG tube

Tube No.	Type of defect	Dimensions	Number of defects
T1	No defect	---	---
T2	Groove	Width 3 mm, Depth 0.23 mm	3
T3	Groove	Width 3 mm, Depth 0.46 mm	3
T4	Hole	Diameter 2.3 mm	2
	Circ. notch	Length 5 mm, Width 1.5 mm and Depth 1.15 mm	

In order to assess the performance of these three techniques the SNR as defined in equation 3.21 was used. Typical as received RFEC signals from tubes T1, T2 and T3 are shown in Figure 4.8, Figure 4.9 and Figure 4.10 respectively with the locations of artificial defects D1, D2 and D3 clearly marked. As discussed earlier, a random shift of the baseline of RFEC signals is observed for the three tubes and this is attributed to be due to the misalignment of exciter-receiver coils and to the presence of bend stresses. A distinct double-peak signal is observed only for groove D1 in tube T3, while the RFEC signals of the other grooves are seen merged with high-amplitude low-frequency noise. The signal, noise and SNR for the as-received signals (raw data) of tubes T2 and T3 are given in Table 4.2. The signal amplitude is determined for the regions of grooves while noise amplitude is determined for the regions between the grooves. Thus, for tubes T2 and T3 there are three signal viz. S1, S2 and S3 and four noise viz. N1, N2, N3 and N4 regions as shown in Figure 4.10. The maximum amplitude in S1, S2, and S3 regions has been considered as signal and the maximum amplitude in N1, N2, N3 and N4 regions has been considered as noise. For tube T1, same noise region as that of tubes T2 and T3 have been used for finding the noise amplitude, N. As can be observed from Table 4.2, the signal and noise amplitudes are nearly identical for T2 and T3 tubes and hence, the SNR is approximately one.

Table 4.2 Signal, noise and SNR of the tubes T2 and T3 in as received condition

Tube No.	Signal, mV	Noise, mV	SNR, dB
T2	300	266	1.02
T3	415	483	-1.32

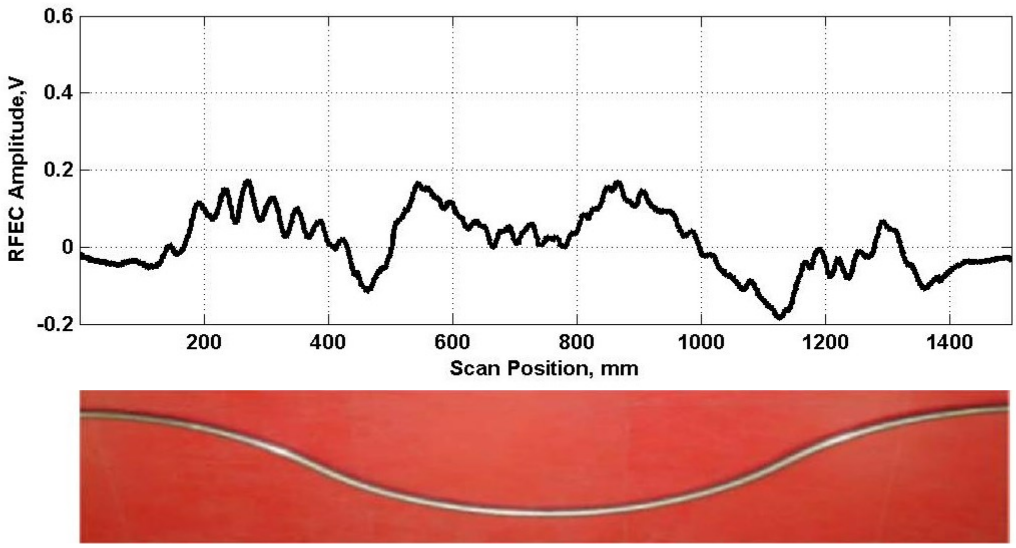

Figure 4.8 RFEC signals from tube defect-free bend tube (T1).

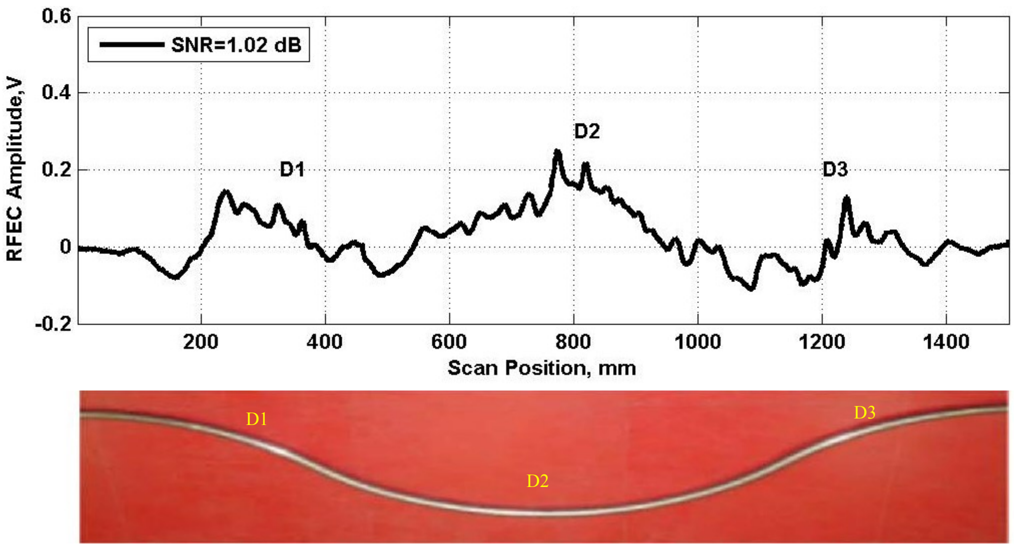

Figure 4.9 RFEC signals from tube T2 having 10% WT grooves in the bend regions.

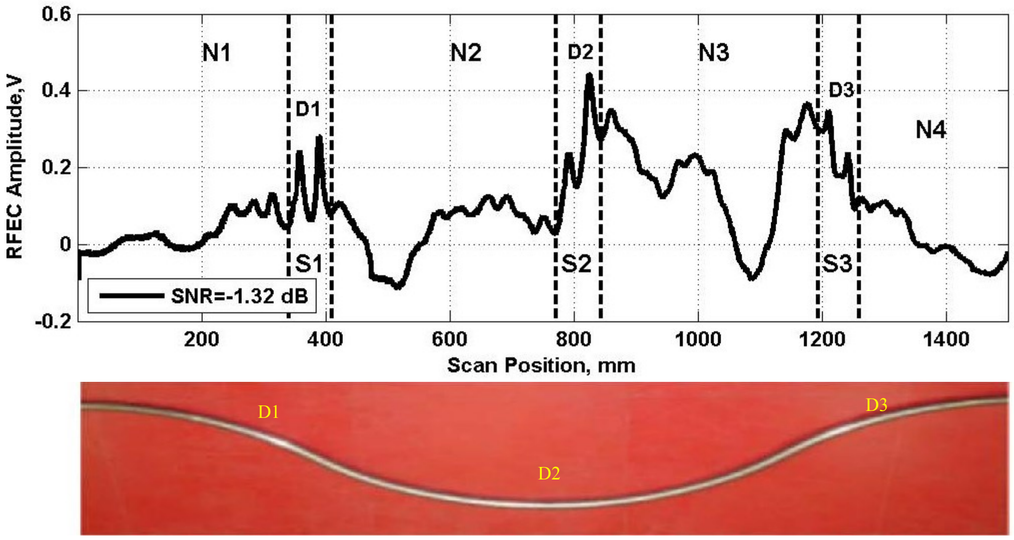

Figure 4.10 RFEC signals from tube T3 having 20% WT grooves in the bend regions.

4.6 Results of the application of signal processing techniques

4.6.1 Fourier filtering technique

In order to identify the upper and lower cut-off frequencies of the band-pass filter, SNR has been assessed using the RFEC signals of tubes T2 & T3. Figure 4.11 shows the contour plot of SNR as a function of the upper and lower cut-off frequencies for

RFEC signals of tube T3 having 20% WT grooves. The SNR is observed to be maximum *i.e.* 7.92 dB for a lower cut-off frequency of 32 Hz and upper cut-off frequency of 200 Hz. Hence, 32-200 Hz has been chosen as the optimum bandwidth for the Fourier filtering. This bandwidth has effectively retained the maximum information from RFEC signals of defects in the bend regions with minimum possible noise from the disturbing variables.

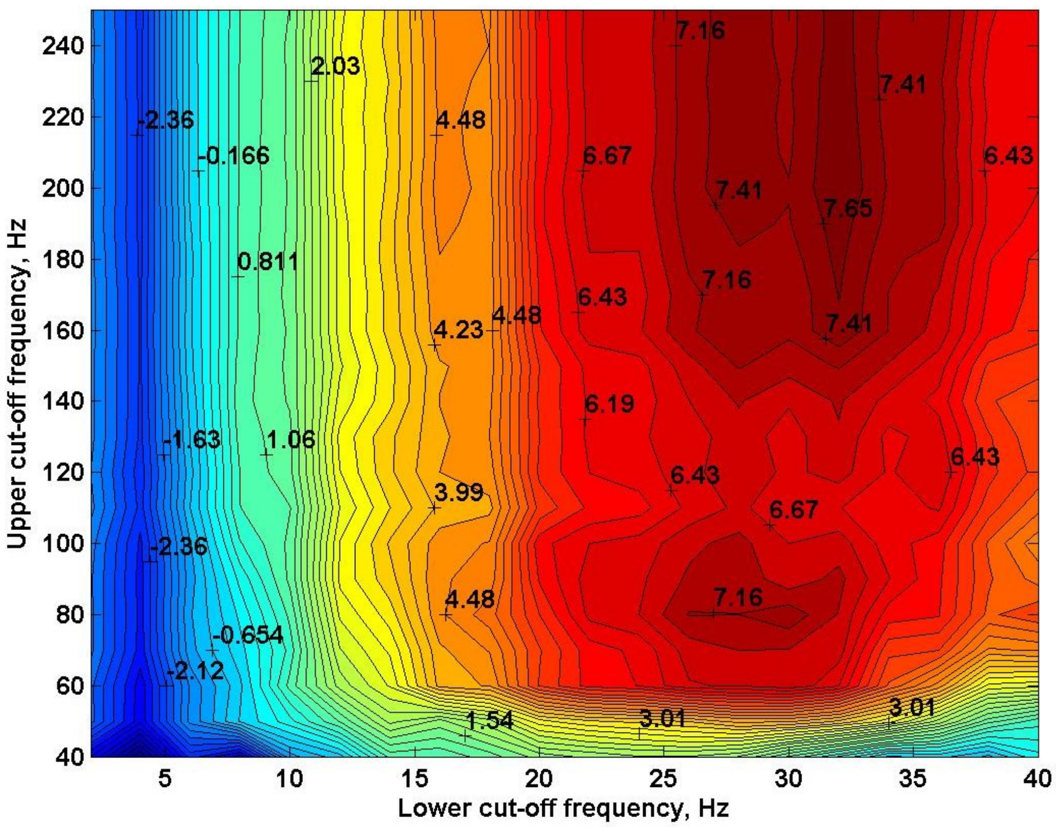

Figure 4.11 SNR as function of lower and upper cut-off band-pass frequencies for RFEC signals of tube T3.

Figure 4.12 shows the RFEC signals after the Fourier filtering for tubes T1, T2 & T3. It can be observed that the high amplitude low-frequency noise mainly due to the bend geometry vis-à-vis misalignment of exciter-receiver coils and bend stresses is significantly reduced. The baseline amplitude is found to be nearly zero for the three tubes. The performance of the Fourier filtering technique for RFEC signals of tubes T2 and T3 is given in Table 4.3. As can be seen, nearly ten-fold reduction in noise is observed and the SNR is found to increase significantly *i.e.* from 1.02 dB to 5.4 dB for tube T2 and from -1.32 dB to 7.92 dB for tube T3. When the maximum noise amplitude of tube T1 (defect-free bend tube) is used as threshold, shown as dotted line in Figure 4.12 grooves D1and D2 of tube T2 are not detected. The higher noise amplitude of tube T1 seems to be due to overlapping of certain frequency components of RFEC signals of grooves with those of noise. Removal of these frequencies may reduce the noise levels as well as the defect signal amplitudes and hence, it is not a preferred choice.

Table 4.3 Signal, noise and SNR of the tubes T2 and T3 before and after Fourier filtering

Tube No.	Signal, mV	Noise, mV	SNR, dB
Before filtering			
T2	300	266	1.02
T3	415	483	-1.32
After Fourier filtering			
T2	54	29	5.40
T3	112	45	7.92

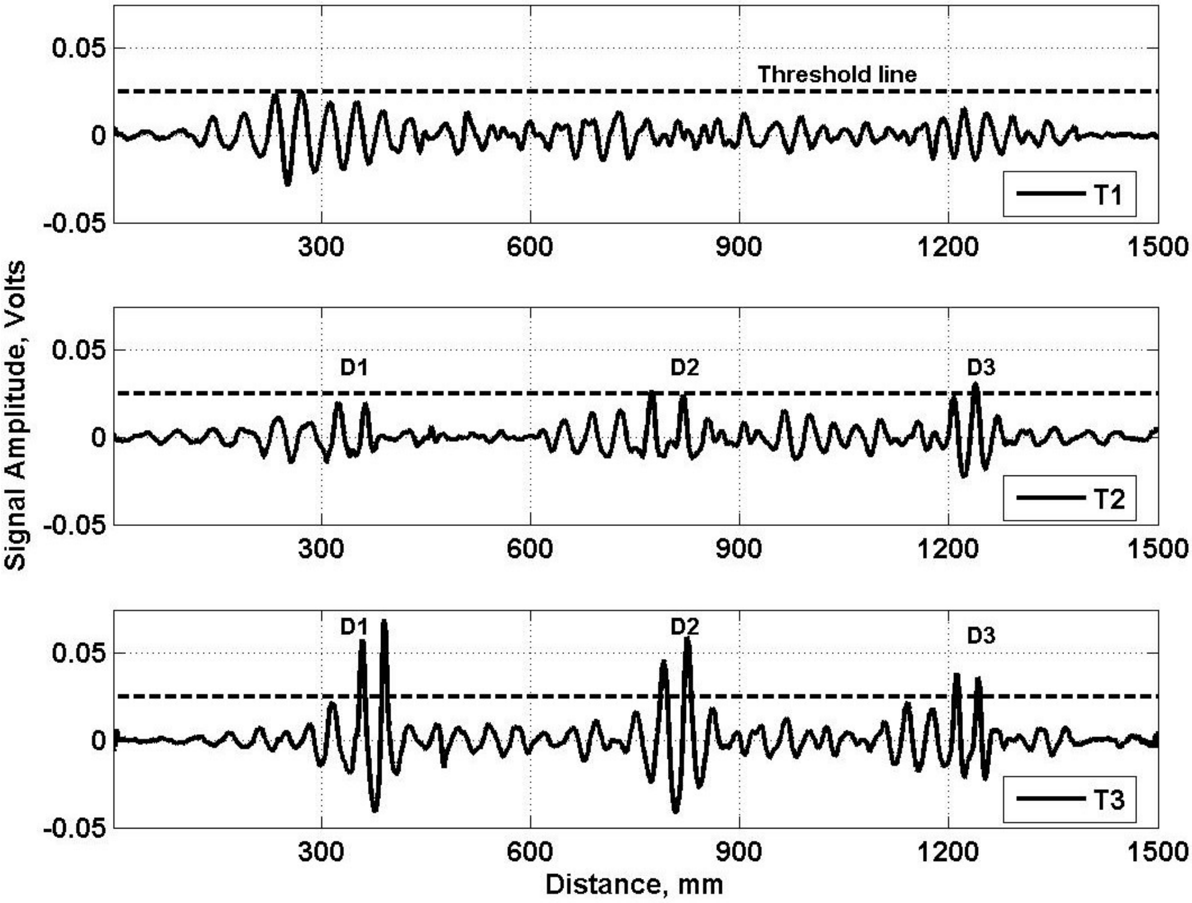

Figure 4.12 Results of application of Fourier filtering to RFEC signals of defect-free tube T1, tube T2 having three 10% WT deep grooves and tube T3 having three 20% WT deep grooves.

4.6.2 Cross-correlation technique

The results of application of the cross-correlation technique using 20% WT deep RFEC signal template to the Fourier filtered signals of tubes T1, T2 and T3 are shown in Figure 4.13. The performance of the cross-correlation technique is given in Table 4.4 for tubes T2 and T3. A nearly four-fold increase in the signal amplitude is observed for tubes T2 and T3 after cross-correlation. This significant enhancement is attributed to the appropriateness of the chosen template of double-peak signal that is identical to the typical RFEC signal of a defect. Interestingly, nearly same performance has been observed when RFEC signal of 10% WT deep groove is used as the template. Despite the signal enhancement, a reduction in SNR, *i.e.* from 5.4 dB to 3.8 dB for tube T2 and from 7.92 dB to 6.27 dB for tube T3, has been observed after applying the cross-correlation technique. Similar observation has also been made when RFEC signals of 20% WT deep groove was used a template. This may be due to the presence of small amplitude Gaussian type noise which resembles the template signal. When the maximum noise amplitude of tube T1 is used as threshold, shown as dotted line in Figure 4.13 all the 10% WT deep grooves and D3 groove of tube T3 are not detected. Closer observation of Figure 4.13 also reveals the loss of distinct double-peak behavior of RFEC signals. Further, it is expected that the cross-correlation technique may not work efficiently if the RFEC signals are asymmetric and distorted due to the presence of irregular wall loss defects.

Table 4.4 Signal, noise and SNR of the tubes T2 and T3 before and after the application of cross correlation.

Tube No.	Signal, mV	Noise, mV	SNR, dB
Before the application of cross correlation			
T2	300	266	1.02
T3	415	483	-1.32
After the application of cross correlation			
T2	196	127	3.80
T3	437	212	6.27

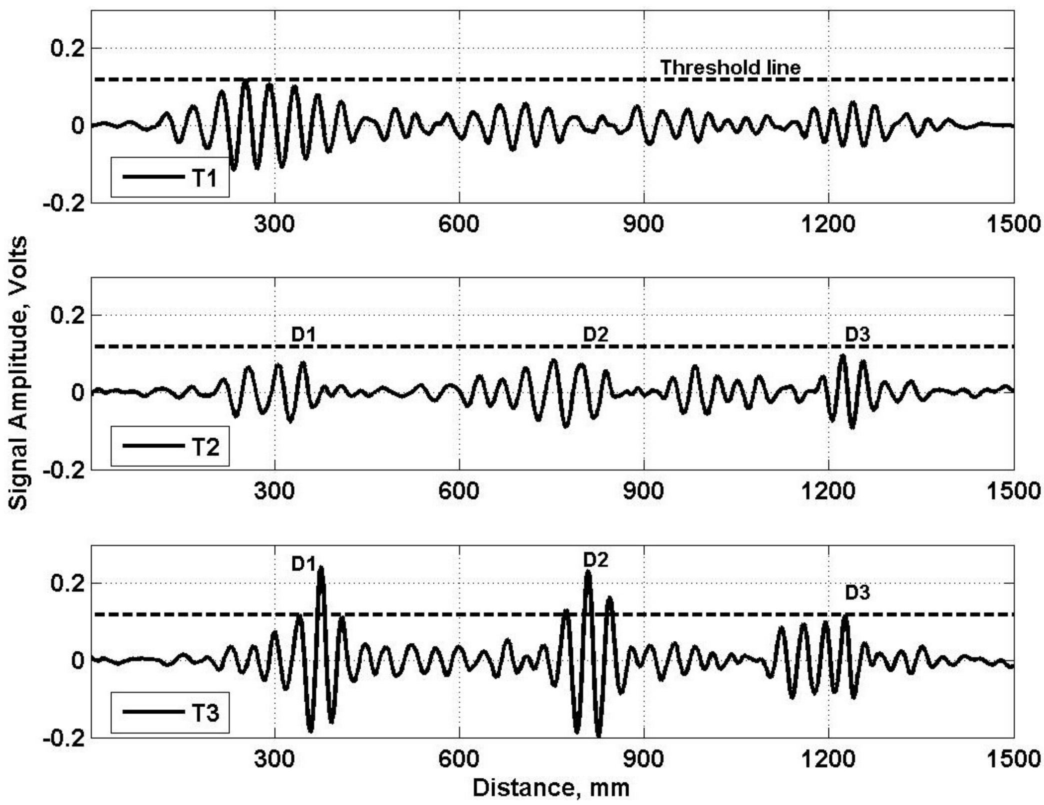

Figure 4.13 Results of application of cross correlation technique to RFEC signals of defect-free tube T1, tube T2 having three 10% WT deep grooves and tube T3 having three 20% WT deep grooves.

Table 4.5 shows the comparative performance of Gaus2, Mexh, Bior2.8 and DB5 wavelets for RFEC signals of tube T2 having 10% WT deep grooves. As can be seen from Table 4.5, the SNR is maximum (7.23dB) for Bior2.8 wavelet at a scale factor of 19 and this wavelet is also found to retain the double-peak behavior of the RFEC signals of localized defects. Hence, Bior2.8 wavelet has been chosen for detailed analysis.

Table 4.5 Comparative performance of various mother wavelets for RFEC signals from tube T2 having three 10% WT deep grooves.

Wavelet	Scale factor, Hz^{-1}	SNR, dB
Gaus2	7	6.50
Mexh	5	6.48
Bior2.8	19	7.23
DB5	15	6.70

Figure 4.14 shows the RFEC signals processed by Bior2.8 wavelet. It is clearly seen from the figure that the wavelet transform technique has resulted in significant increase in signal amplitude for tubes T2 and T3, as compared to the Fourier filtering and cross correlation techniques. At the same time, the noise reduction performance of the wavelet transform technique is superior to that of the cross correlation technique, but inferior to the Fourier filtering technique. When the maximum noise amplitude of tube T1 is used as the threshold, shown as dotted line in Figure 4.14 both 10% and 20% WT deep grooves are detected unambiguously. The improvement in SNR after CWT is found to be more than 7 dB. The signal, noise and SNR for tubes T2 and T3 after the application of CWT processing are given in Table 4.6.

Table 4.6 Signal, noise and SNR of the tubes T2 and T3 before and after CWT processing.

Tube No.	Signal, mV	Noise, mV	SNR, dB
Before wavelet processing			
T2	300	266	1.02
T3	415	483	-1.32
After wavelet processing			
T2	204	89	7.23
T3	530	204	8.30

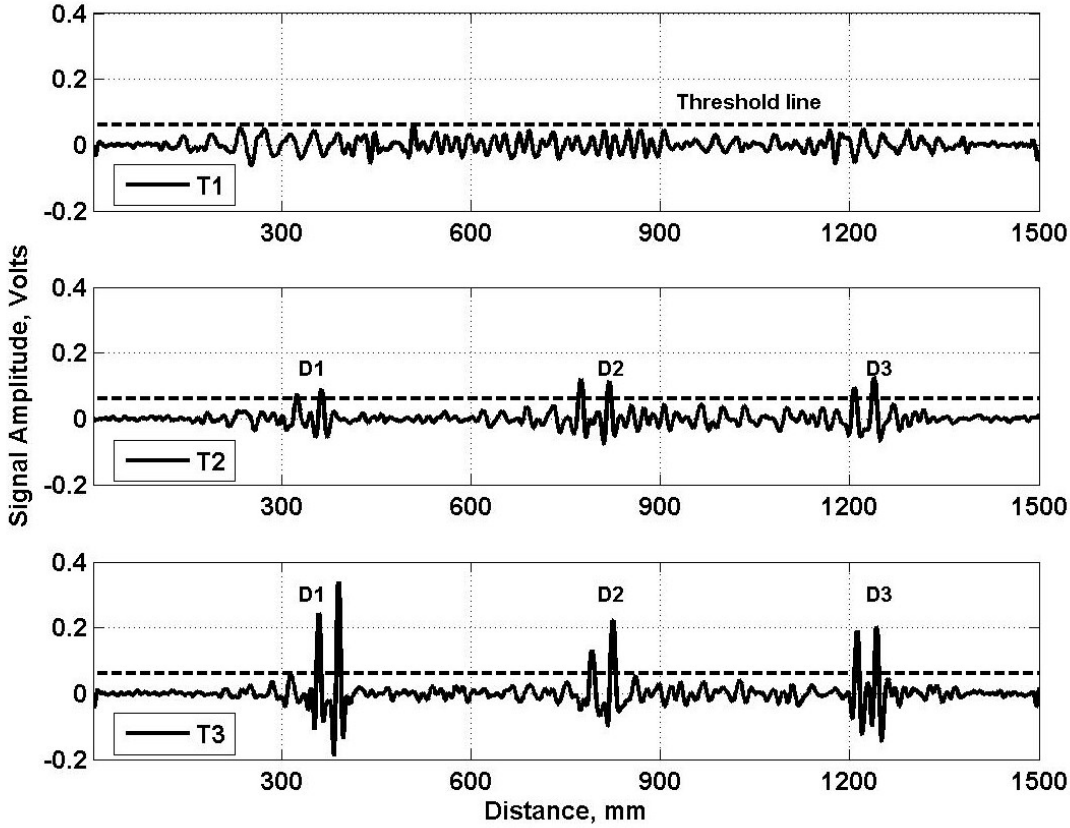

Figure 4.14 Wavelet transform processed RFEC signals of defect-free bend tube T1, tube T2 having three 10% WT deep grooves and tube T3 having three 20% WT deep grooves.

4.7 Discussion

The wavelet transform technique has preserved the double-peak behavior of the RFEC signals. The performance of the wavelet transform technique to the filtered RFEC data of tubes T2 and T3 has been found to be nearly the same. This reaffirms the fact that the wavelet transform technique possesses the band-pass characteristics of the Fourier filtering. Thus, the studies clearly establish that it would be possible to detect OD defects deeper than 10% WT in bend regions of SG tubes using the wavelet transform technique.

Results of application of the three techniques to RFEC signals of tube T4 having a hole and a notch in the bend regions are shown in Figure 4.15 The threshold levels determined earlier have been introduced in the figure for comparing the performance.

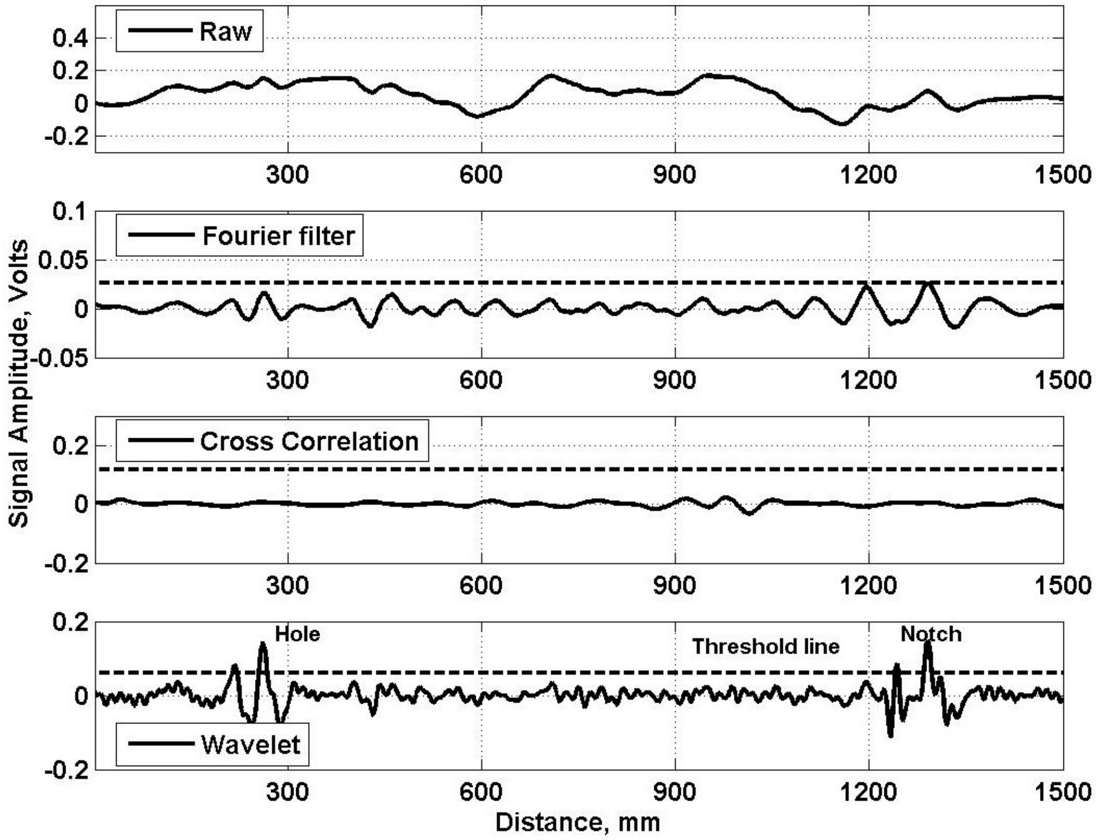

Figure 4.15 As-received RFEC signals from tube T4 having 2 mm diameter hole and 1.15 mm deep circumferential notch in the bend region and the signals processed by the Fourier filtering, cross correlation and wavelet transform techniques.

As can be observed, the wavelet transform technique outperformed the Fourier filtering and cross correlation techniques. The inferior detection performance of the cross-correlation technique is attributed to the spatial mismatch between the chosen template and the signals of localized defects.

The sizing performance of the wavelet transform technique has been analyzed for defects in bend regions as well as straight regions using arithmetic mean of peak amplitudes of RFEC signals. Figure 4.16 shows the mean peak amplitude of RFEC signals for grooves in straight regions and bend regions (wavelet processed) of SG tubes.

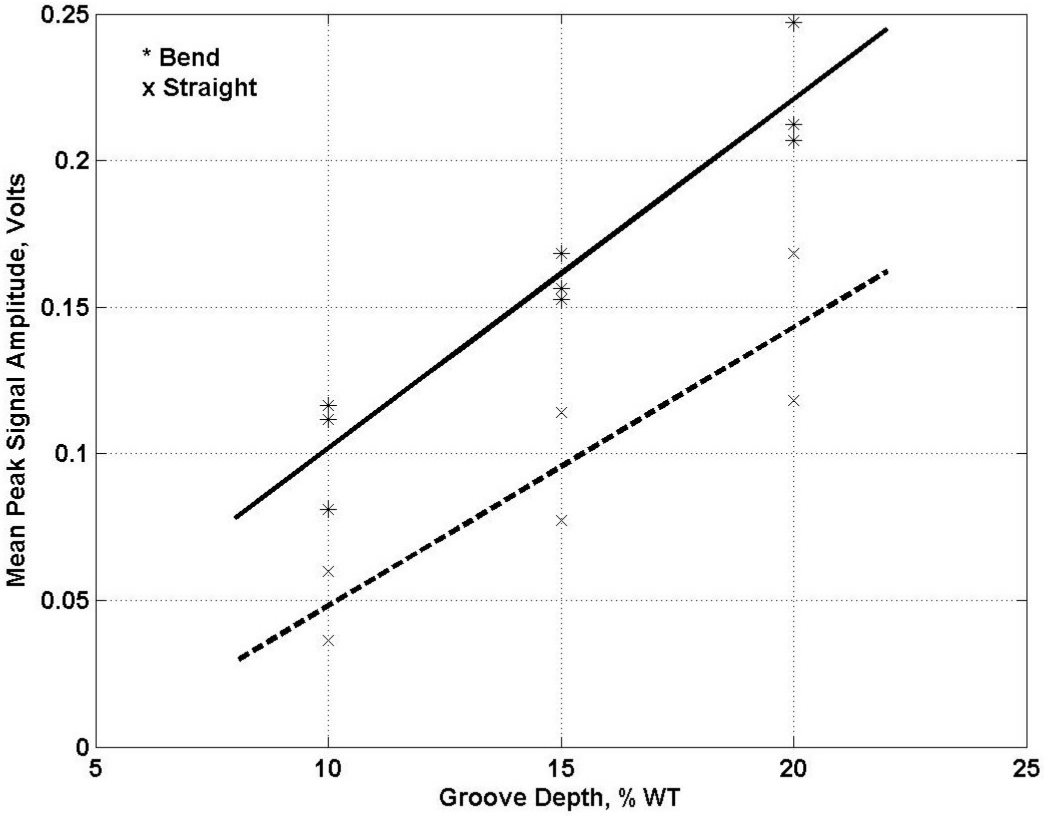

Figure 4.16 Quantitative evaluation of thickness of grooves in straight and bend regions of SG tubes.

As can be observed, the mean amplitude of signals of grooves in bend regions is always higher than that of the straight regions. Thus, this study reveals that separate calibration graphs are essential for sizing the defects in straight and bend regions of the SG tubes. But this could be avoided, if the RFEC signals from straight tubes are also subjected to the same type of processing. This particular approach is advantageous as there is chance of improving the SNR for the straight section of the SG tubes also.

The studies have clearly shown that signal processing approach is promising for detection of defects in the bend regions of the SG tubes. It might also be beneficial at this juncture to consider other approaches. As discussed in the Section 2.5.3, there could be approaches based on sensor level as well as interpretation of signals. However, these approaches are highly depended on the bend geometry and the SG tube under consideration. The signal processing approach is independent of the probe and geometry of the bend tube.

The key issue in the RFEC testing of bend regions is the misalignment of exciter-receiver coils as compared to other effects. This misalignment could also be minimized to improve the SNR. This is possible only when the distance between the exciter and receiver coils is as small as possible. Design of magnetic or conducting shielding would reduce the effective RFEC probe length, thereby bringing down the misalignment effect. As discussed in Chapter 3, nonlinear FE model would be highly useful in this context to study the shielding effects of different material on the RFEC characteristics.

4.8 Summary

1. The performance of the RFEC instrument and probe was validated by detecting grooves, FBHs and 20%, 30% and 40% WT deep notches. Reliable detection of 20% WT deep notch achieved in the straight sections of the SG tubes.

2. The CWT technique based signal processing approach using Bior2.8 wavelet has shown the noise reduction capability of Fourier filtering technique and the signal enhancement capability of the cross-correlation technique.
3. Application of the CWT based signal processing approach resulted in the unambiguous detection of 10% WT deep grooves present anywhere in the bend regions.
4. This study highlights for the first time, the need to use separate calibration curves for straight and bend regions of the SG tubes for reliable sizing of defects.

Chapter 5: Approaches based on signal feature identification and multifrequency mixing

5.1 Introduction

This chapter presents approaches for detection of defects in the presence of sodium deposits and support structures as these two problems are nearly similar in nature. The chapter describes the experiments carried out in a sodium test vessel to study the influence of sodium deposits on the RFEC signals of defects. It presents the feature based approach for detection and characterization of defects in the presence sodium deposits. The chapter later discusses the multifrequency mixing approach proposed for elimination of strong influence of support structures.

5.2 Experimental studies on sodium influence on RFEC signals

Inspection of SG tubes using RFEC technique would be carried out during reactor shutdown after draining sodium and water from the SG. During the draining process, some amount of residual sodium would remain on the tube wall or would also enter into the defects formed, if any, on the outer surface of the SG tubes. Sodium is a good electrical conductor (conductivity ~40% IACS) [67]. Hence, it is anticipated that residual sodium deposits would influence the RFEC signals and detection and characterization of defects. Experimental studies are necessary, in this regard, to investigate the influence of sodium deposits on RFEC signals.

5.3 Studies in sodium test vessel

In order to study the sodium influence on RFEC signals, experimental studies replicating the actual ISI conditions of the SG tubes, have been carried out. In the experimental studies, a set of SG tubes having artificial grooves have been exposed to sodium environment in a specially designed test vessel. Five numbers of defect-free, 1200 mm long SG tubes were taken and uniform wall thinning grooves of depths 0.23 mm (10% WT), 0.46 mm (20% WT), 0.69 mm (30% WT), and 0.96 mm (40% WT) deep and of 3 mm and 2 mm width were machined at the outer surface of four tubes as detailed in Table 5.1. One tube was included to obtain baseline data and to examine the influence of buildup of sodium deposits.

Table 5.1 Dimensions of grooves machined in steam generator tubes.

Tube Number	Depth of grooves, mm (% WT)	Width of Grooves, mm	
		Location 2 (400 mm from bottom), mm	Location 1 (200 mm from bottom), mm
1	0.92 (40%)	3	2
2	0.69 (30%)	3	2
3	0.46 (20%)	3	2
4	0.23 (10%)	3	2
5	No groove		

These five tubes were welded to a 233 mm diameter circular flange at a triangular pitch of 32 mm, same as that of the actual SG tube sheet. The bottoms of the tubes were hermetically sealed to prevent entry of sodium into the tubes. The flange was kept inside a specially designed stainless steel test vessel (height of 1248 mm and diameter of 417 mm) consisting of sodium at 500°C. Three resistance type level probes were installed at 260 mm, 375 mm and 595 mm heights to monitor the level of sodium inside the test vessel. The photograph of the sodium test vessel used is shown in Figure 5.1. As sodium is pyrophoric, the test vessel was evacuated initially and argon was purged to avoid entry of oxygen.

Figure 5.1 Photograph of the test vessel used to study the influence sodium deposits on SG tubes.

Baseline RFEC data for the uniform wall loss grooves were acquired prior to insertion of the flange in the test vessel. Hot sodium at 500° C was pumped into the test vessel to about 600 mm to ensure complete immersion of the grooves in the tubes and then, the sodium was drained after 2 hours. Five such cycles were repeated to simulate the actual condition of the SGs. RFEC signals were once again acquired and stored for comparative analysis prior to and after sodium exposure. The flange was taken out of the test vessel and visual examination was carried out to monitor the build-up of sodium deposits on the tubes in the flange as well as in the grooves. The RFEC measurements were repeated a number of times to ensure the repeatability of signals and to obtain the scatter in the measurements.

5.4 Results of the experimental studies

The photograph of the flange after it is removed from the test vessel is shown in Figure 5.2. As can be observed, sodium deposits are formed in the grooves as well on the tube outer surface. In all the grooves, sodium appeared to fill almost the whole volume. Sodium deposits are also observed on the bottom regions of the stainless steel flange due to condensation of sodium during the sodium exposure and draining.

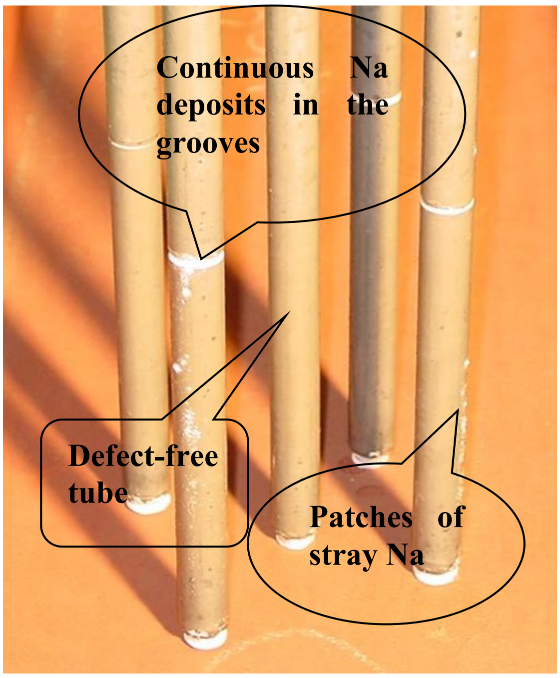

Figure 5.2 Photograph of the flange after sodium exposure and removal from the vessel.

RFEC signals before and after sodium exposure of the tubes having 10%, 20%, 30% and 40% WT deep grooves of 3 mm and 2 mm widths are shown in Figure 5.3 and Figure 5.4 respectively.

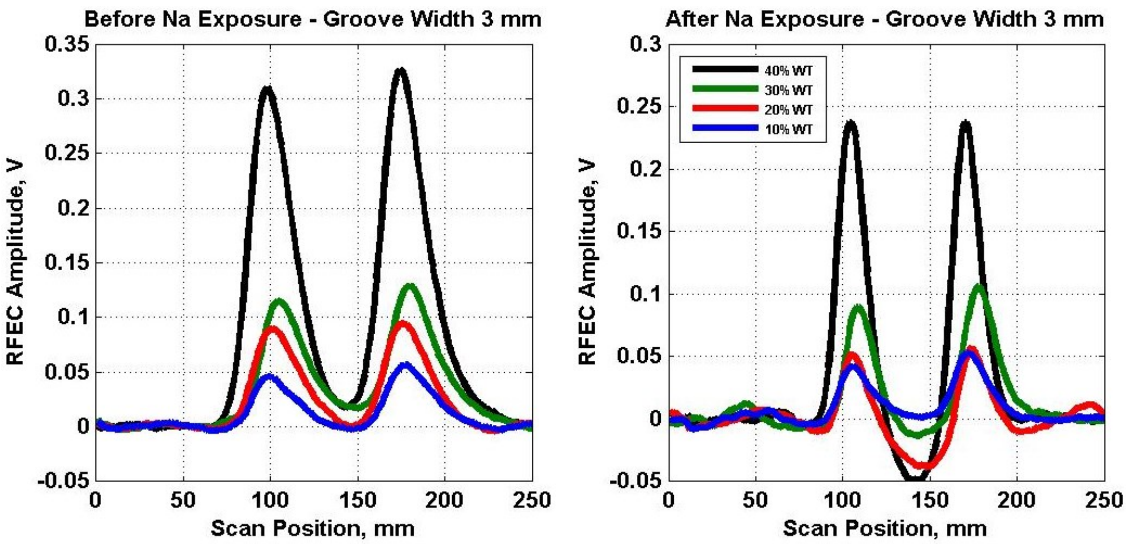

Figure 5.3 RFEC signals of 3 mm width grooves of different depths, before and after sodium exposure.

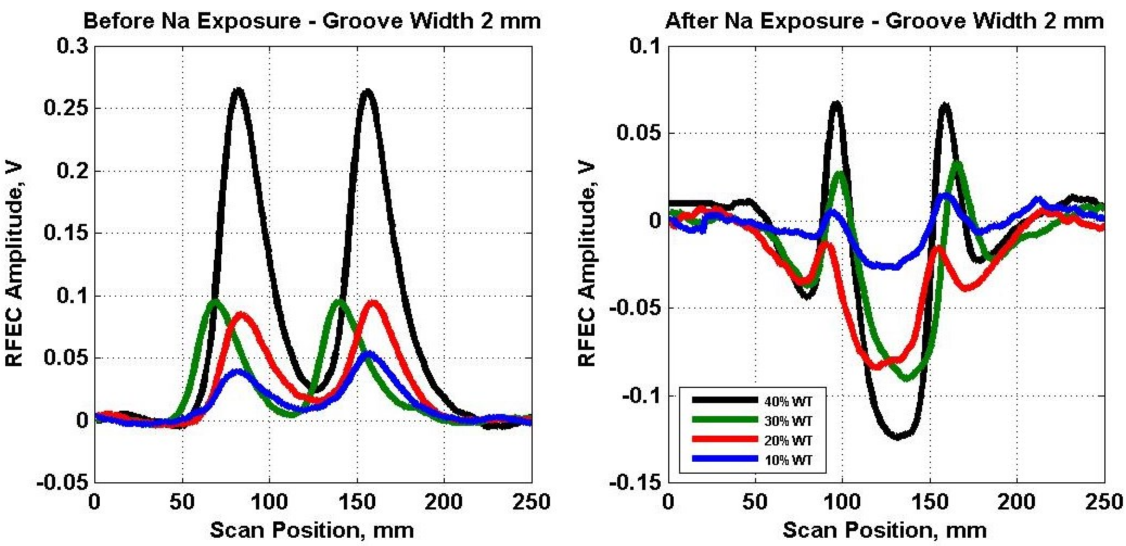

Figure 5.4 RFEC signals of 2 mm width grooves of different depths, before and after sodium exposure.

The raw RFEC signals were processed to remove the low frequency variations in the baseline and high frequency noise. The low frequency baseline was corrected by polynomial fitting algorithm without affecting the RFEC signals of defects. Moving window averaging (25 data points) was done to remove the high frequency noise in the RFEC signals due to electronics and material noise. The deposits on defect-free regions are seen to be scattered and discontinuous. As a result, only feeble signals from the deposits are noticed. However, significant changes in RFEC signals are noticed for grooves after exposure to sodium as shown in the figures. A very small shift of baseline with a marginal reduction in overall signal amplitude is noticed after exposure to sodium. Further, a valley formation between the characteristic peaks of the RFEC signals is observed for the grooves. As there are no other disturbing variables present, this change in the signal shape is attributed to the presence of sodium deposits in the grooves. The RFEC signal parameters have been analyzed in detail to quantitatively characterize the sodium influence. Figure 5.5 shows the parameters viz., valley depth of the RFEC signals below the baseline, denoted as ‘H’ and the peak-to-peak amplitude denoted as ‘A’ considered for this analysis.

The reason for the valley formation is predominantly due to the electrically conductivity of the sodium deposits, which strengthen the distribution of eddy currents in the vicinity of the defects which is in contrast to wall loss situation. Wall loss condition reduces the effective permeability and conductivity, which results in the higher magnetic field reaching the receiver coil thus increasing the induced voltage. Hence, RFEC signals due to wall loss defects shows positive peaks. On the contrary, sodium deposit increases the effective conductivity, which strengthens the distribution of eddy current in the vicinity of the defects. This causes very small amount of magnetic field reaching the receiver coils. As a result, the RFEC signals due to sodium deposits produce negatively peaked RFEC signals.

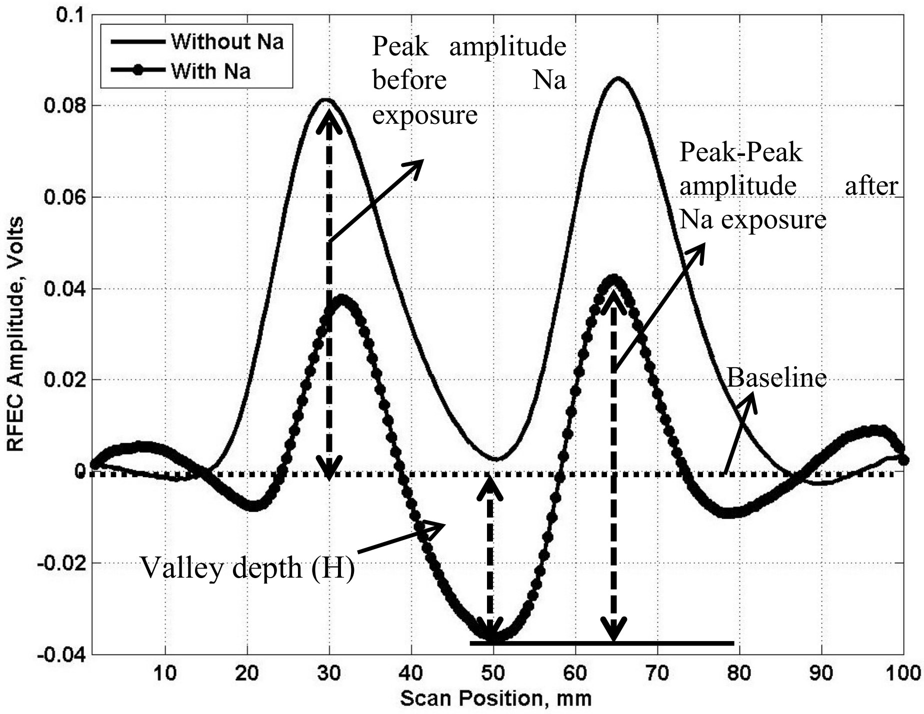

Figure 5.5 Measured RFEC signal with and witout sodium deposits in 20% WT groove of 3 mm and derived signal parameters used.

With increase in depth of groove, the valley depth is found to increase systematically due to the enhanced volume of sodium deposits in the groove. Thus, this study brings out the point that it is possible to identify the presence of sodium deposit in a defect through the identification of a valley between the characteristic RFEC signals. The measured ‘H’ values for 3 mm and 2 mm wide grooves as a function of wall loss are plotted in Figure 5.6. A monotonic increase in ‘H’ values is observed with groove depth, in other words, with increasing volume of the deposited sodium. This confirms the strong influence of sodium conductivity on the RFEC signals and hence, it is possible to use the parameter ‘H’ for estimating the volume of sodium deposited in defects. It is also observed from Figure 5.6 that the ‘H’ values are higher for the 2 mm width grooves in comparison with the 3 mm width grooves.

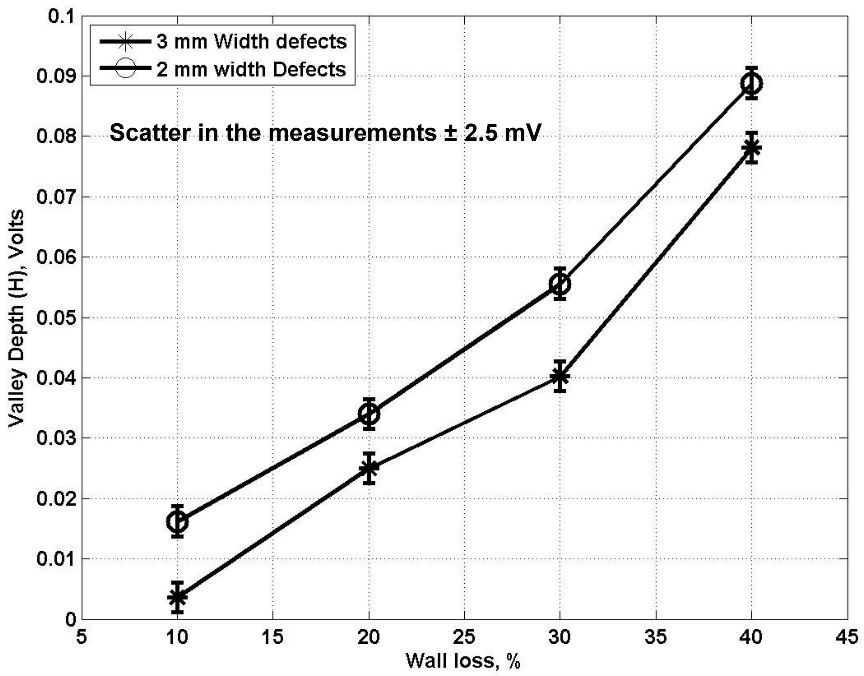

Figure 5.6 Valley depth (H) for 3 and 2 mm width grooves of different wall loss.

During visual examination of the groove regions in the flange immediately after removal from the test vessel, the amount of sodium deposited in the 2 mm width grooves appeared more as compared to the 3 mm width grooves. This is attributed to the combined effect of surface tension due to which the accumulated sodium in defects becomes more, when the width of the defects is relatively small. Hence, the probability sodium sticking to the grooves having width less than 2 mm is more. In a similar manner, the chance of sodium sticking to grooves having width more than 3 mm would be very small as sodium would tend to flow rather confining to this large area due to the surface tension.

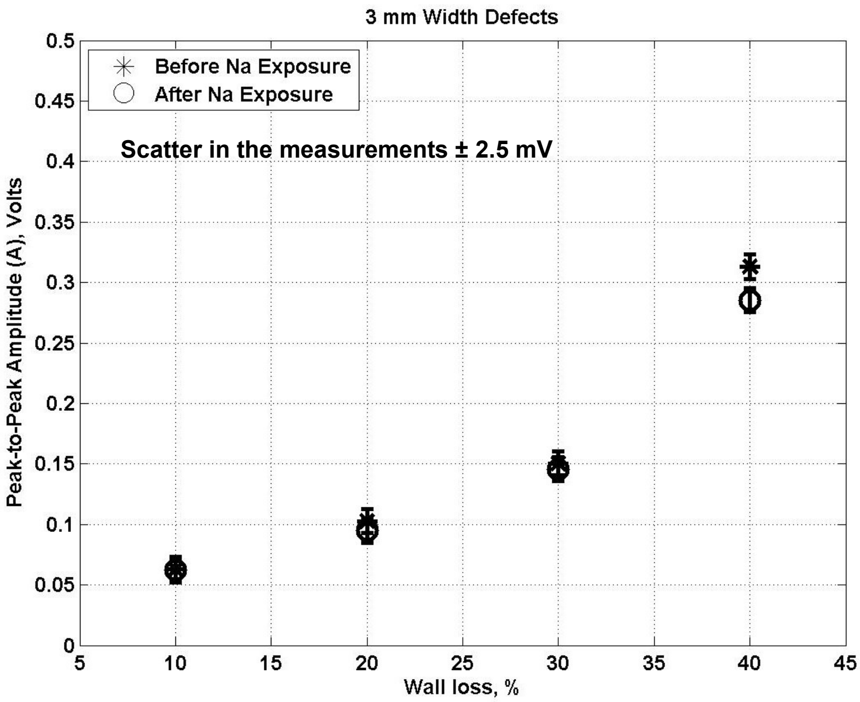

Figure 5.7 The measured peak-to-peak amplitude (A) for different wall loss defects (width 3 mm) before and after sodium exposure.

The variations of Peak-to-Peak amplitude 'A' with wall loss for 3 mm and 2 mm wide grooves before and after exposure to sodium are shown in Figure 5.7 and Figure 5.8, respectively. As expected, there is an increase in magnitude of 'A' with increasing the width and wall loss. However, it is observed that the Peak-to-Peak amplitude is found to be nearly the same before and after sodium exposure. This is an interesting observation reported for the first time and makes 'A' a very useful parameter, essentially because it is independent of sodium influence as compared to 'H'. In view of this, Peak-to-Peak amplitude is useful for sizing of defects, despite the presence of sodium deposits in defects. Thus, the experimental study clearly shows that the sodium deposits do not significantly influence detection and sizing of defects in SG tubes, if the invariant parameters are judiciously used.

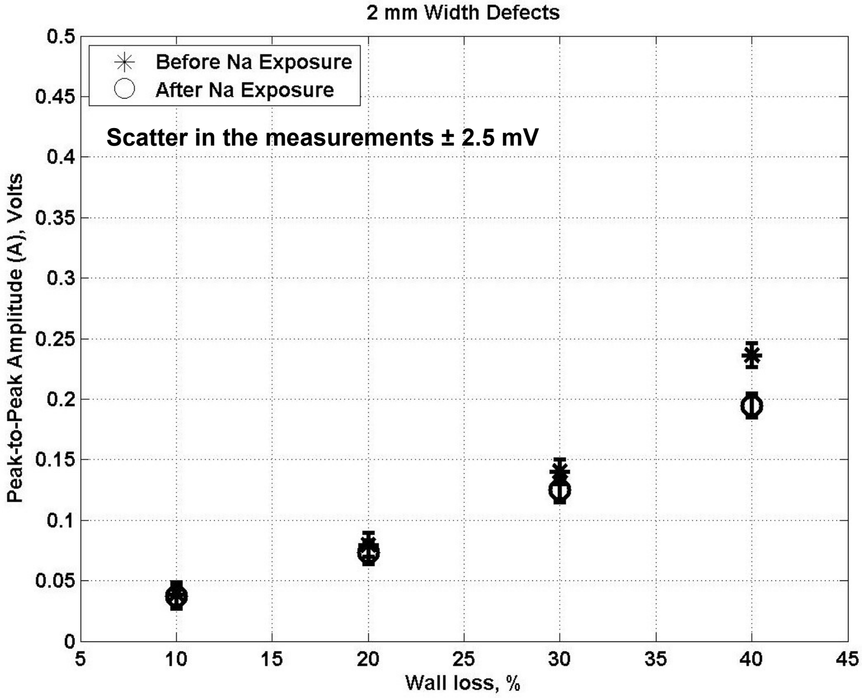

Figure 5.8 The measured peak-to-peak amplitude (A) for different wall loss defects (width 2 mm) before and after sodium exposure.

5.5 Model based investigation of the sodium influence

In order to understand the experimental observation, FE modeling has been performed. RFEC signals of the grooves with and without sodium filling have been predicted by the 2D axisymmetric nonlinear model. Figure 5.9 shows the induced current density in the regions of a 50% WT groove and the groove filled sodium. Higher eddy current density is observed for the case of the groove with sodium. This would cause a reduction in the induced voltage of the detector coil. This result further strengthens the understanding of the behavior of valley formation in the RFEC signals when sodium deposits are formed in the defects.

.

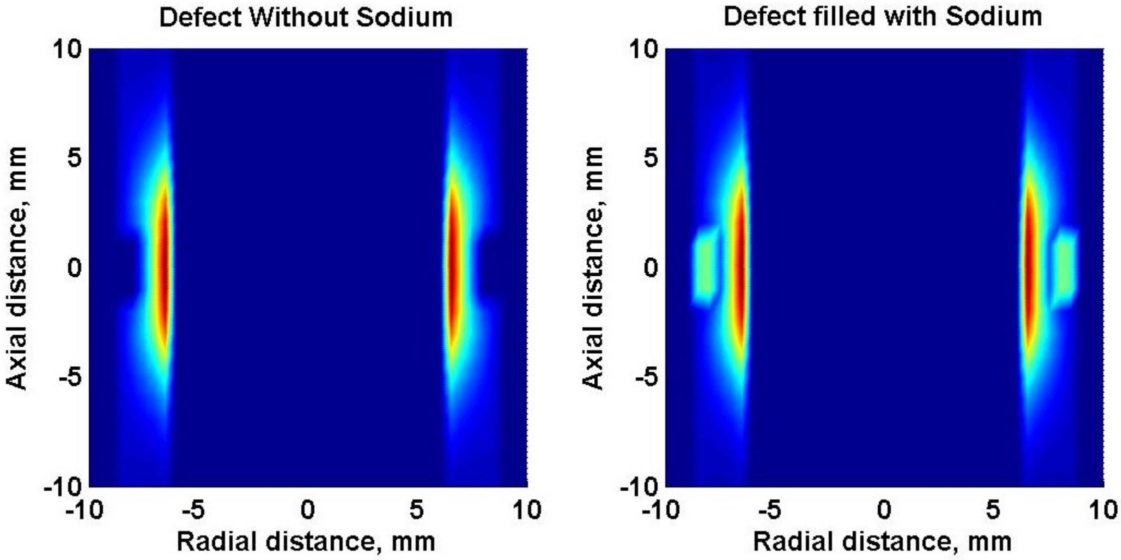

Figure 5.9 Surface plots of the induced current density in the tube wall due to the exciter coil and a 50% wall loss groove and the groove filled with sodium.

Figure 5.10 shows the model predicted RFEC signals of 20% WT groove of 2 mm width, with and without sodium filling. As seen from the figure, the formation of a valley below the baseline of the RFEC signals with sodium filling has been correctly predicted by the model. It can be observed that the model predictions are in good agreement with the experimental measurements presented in Figure 5.4 The model predicted peak-to-peak amplitude (A) for different wall loss defects (width 3 mm) with and without sodium filling the groove regions, has been shown in Figure 5.11 . The results from the graphs closely agree with the experimental observation. Thus, the model predictions reiterate the results of the experimental studies and this gives the confidence that the nonlinear FE model correctly represents the electromagnetic field interactions.

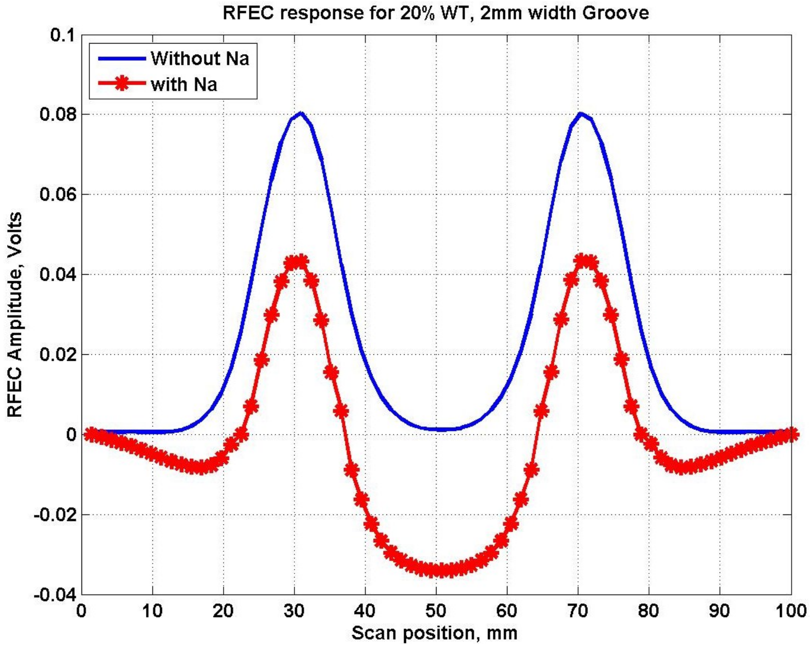

Figure 5.10 Model predicted RFEC signals of grooves with and without sodium filling.

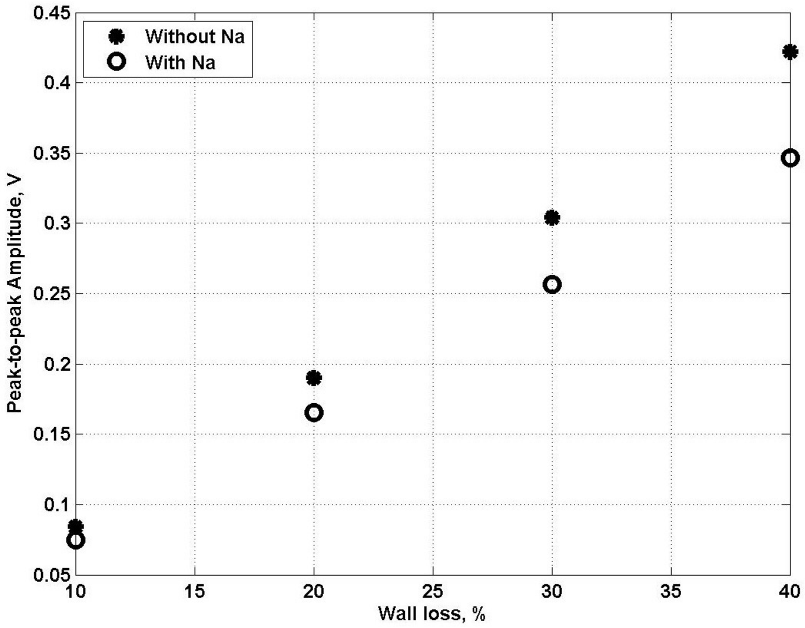

Figure 5.11 The model predicted peak-to-peak amplitude (A) for different wall loss defects (width 3 mm) with and without sodium filling.

5.6 Multifrequency mixing approach

The PFBR SG tubes are supported at various locations including the bend regions by egg crate type support structures. Unlike the regular baffle arrangement, egg crate type structures are used in PFBR SG to reduce the shell side pressure. Figure 5.12 shows the drawing of the tube support structure strip and photograph of the tube bundle with egg crate support strips.

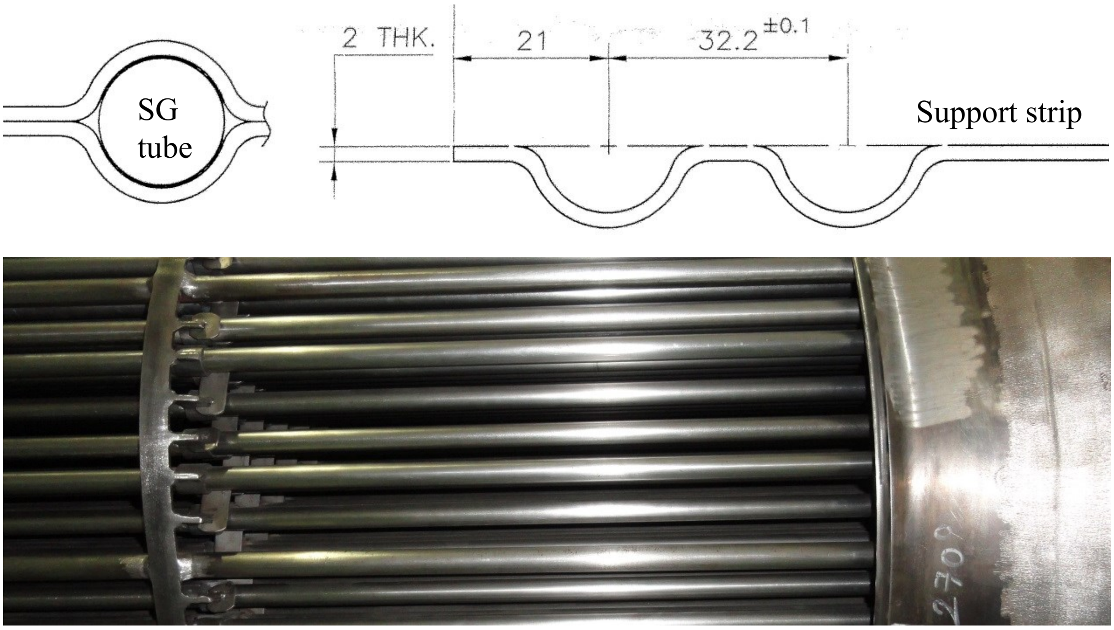

Figure 5.12 Drawing of the tube support strip and photograph of the tube bundle.

The support structures are made of Aluminized Inconel 718, to reduce fretting wear rate. The electrical conductivity of Inconel 718 is $8x10^5$ S/m or 1.3% IACS. This change in the conductivity at the support structure locations in the SG tubes and formation of thin sodium layer in between and besides, the support structures would influence the RFEC signals of defects, if any, present in the vicinity. Hence, it is important to identify an approach (e.g., multifrequency) for detection of defects under the support structures.

5.7 Background of the multifrequency mixing technique

Multifrequency mixing technique is routinely used in eddy current NDT to eliminate disturbing variables. The multifrequency technique can be used to eliminate any number of disturbing variables such as wobble, noisy signals due to magnetic deposits, support plate influence and any other geometrical variations in the structure under inspection [35]. The general rule of thumb for the number of frequencies to be used is as follows: If there are N numbers of disturbing variables, N+1 numbers of excitation frequencies and N number of mixing sequences should be used to eliminate them. Although, it is a standard practice in eddy current testing, application of multifrequency mixing in RFEC testing has not widely been reported. This might probably due to the fact that the RFEC characteristic in the tube under consideration is highly dependent on the excitation frequency.

In a typical dual frequency mixing technique a high and low frequency sinusoids are simultaneously used to excite the RFEC probe. The primary frequency (F_1) is the optimum frequency and the secondary frequency (F_2) is selected to be lower than F_1 to penetrate deeper in the material. Selection of the secondary frequency is subjective and is discussed in Section 5.10. In traditional offline mixing algorithms, the RFEC signal of support structure from F_2 is matched with F_1, such that the arithmetic difference results in zero. This is achieved by iteratively scaling and rotating the signal of support structure from F_2 using affine transformation matrix. Nonlinear least square minimization technique is employed for these iterative schemes [94,95].

5.8 New multifrequency mixing algorithm

Neural networks, gradient descent search or perceptron learning algorithms could be used in place of the iterative least square minimization to transform the impedance data of F2 to the impedance of data of F1. In this work, a new mixing algorithm based on linear kernel transform (LKT) is proposed. A linear kernel transform is a neural network, which makes a simple linear regression model into nonlinear through the use of kernel [96]. The kernel is a matrix containing similarity measures for a dataset. The kernel should be in Hilbert space (inner product vector space) satisfying the positive definitiveness, symmetry and bilinearity conditions [97].

Typical single layer LKT neural network as shown in Figure 5.13 consists of an input, kernel matrix and the output. The input consists of *N* independent components and *M* number of training data set. Accordingly the kernel is an $N \times N$ matrix. The individual matrix elements are functions of the input. The output is the weighted sum of the kernel matrix as given in Equation 5.1.

$$\hat{\boldsymbol{y}} = \boldsymbol{K_{nn}} \times \boldsymbol{w_n} \quad \ldots 5.1$$

Commonly used kernels in regression algorithms include the radial basis function and polynomial kernel. In this study, radial basis function kernel is used:

$$K_{ij} = e^{\frac{\left\| x_j - x_i \right\|_2}{2\sigma^2}} \quad \ldots 5.2$$

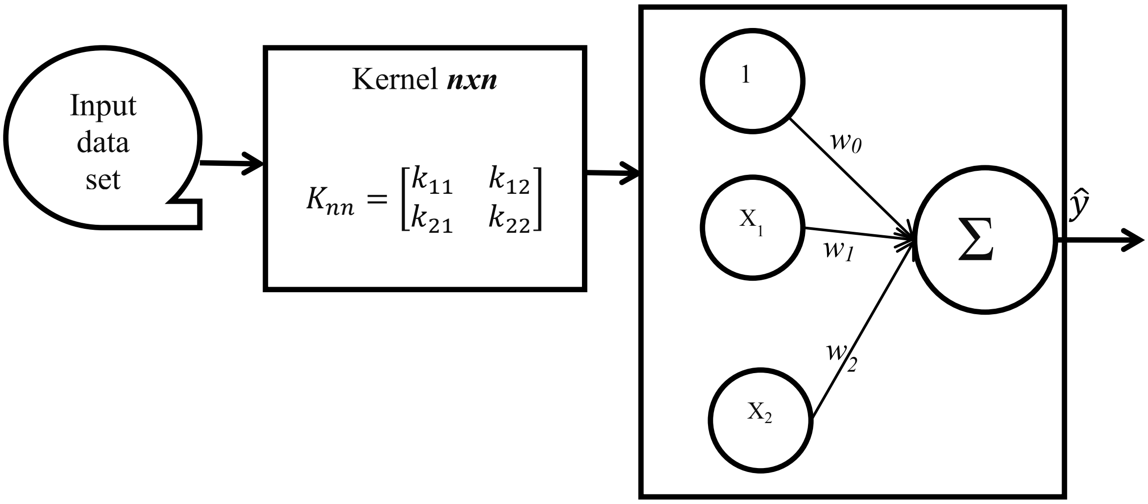

Figure 5.13 Schematic of the architecture of linear kernel transform.

In present study, two inputs have been used (n=2), which are the real and imaginary components of the RFEC signals from F_2. The output is trained to be F1 for support structures. Training of the LKT involves the computation of the kernel matrix and optimization of the weights. Iterative error minimization technique has been applied for optimizing the weights. The LKT has been trained once based on the RFEC signals of the support structure at two different frequencies. Mixing of two frequency data has been carried out after computing the transformed F2 impedance data by the trained LKT and computing the difference between the transformed impedance data of F2 and the primary frequency (F1) impedance data. Two frequency RFEC signals obtained from FE model predictions have been used for training and evaluation of the LKT neural network.

5.9 Multifrequency mixing of model predicted signals

RFEC signals of 3 mm width, 20% WT (0.46 mm), 30% WT (0.69 mm) and 40% WT (0.92 mm) depths of wall thinning grooves in the presence of support structures have been predicted by finite element model at operating frequencies of 825, 725 and 625

Hz. Figure 5.14 shows real and imaginary components of the RFEC signals from these frequencies. These signals were used for mixing to eliminate the influence of support structure.

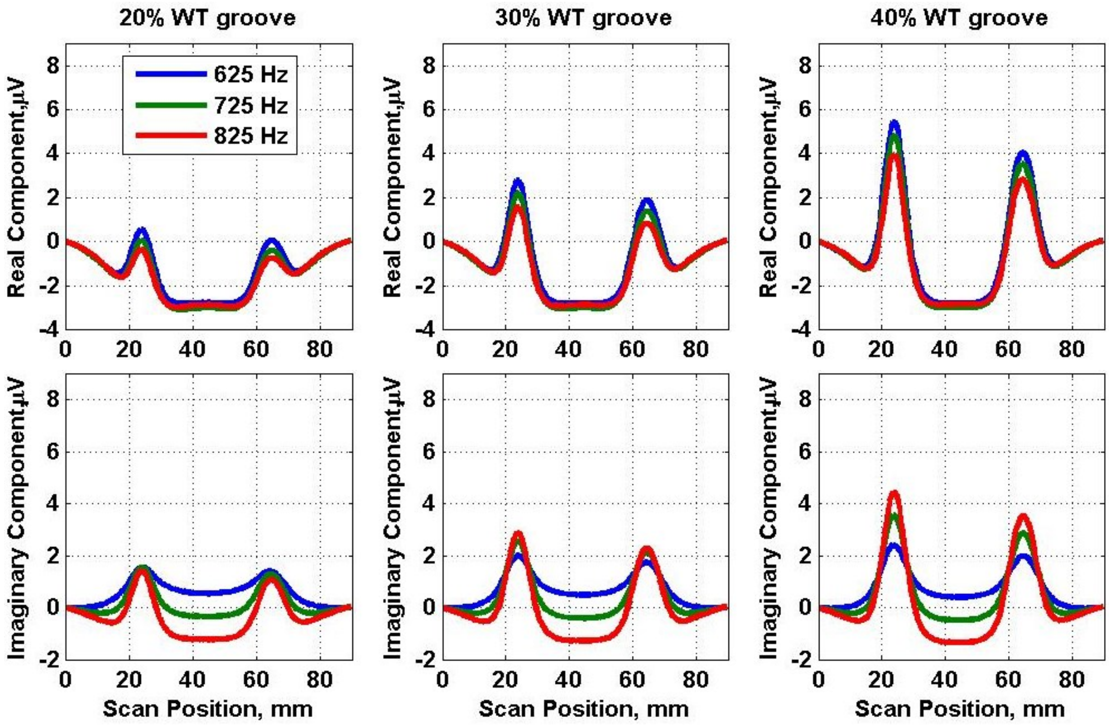

Figure 5.14 Model predicted RFEC signals of wall thinning grooves in the presence of support structure at different frequencies.

As can be seen, the RFEC signals show a valley formation like in the case of defects filled with sodium deposits (refer Section 5.4). This is due to the effective change in the conductivity due to the support structure build up. The phase angle (orientation) of the support structure and grooves are found to be different within one frequency and are also different for different frequencies.

Two different combinations of mixing *i.e.* Mix-1 and Mix-2 have been chosen from the three model predicted RFEC signals. Mix-1 uses 825 Hz & 725 Hz and Mix-2 uses 825 & 625 Hz. Figure 5.15 and Figure 5.16 shows the output of the LKT for the Mix-1 and Mix-2 signals. As observed the mixer output is free from the influence of support structure signals. In order to assess the performance of the Mix-1 and Mix-2 combinations, the outputs were compared with RFEC signals of support structure obtained at 825 Hz.

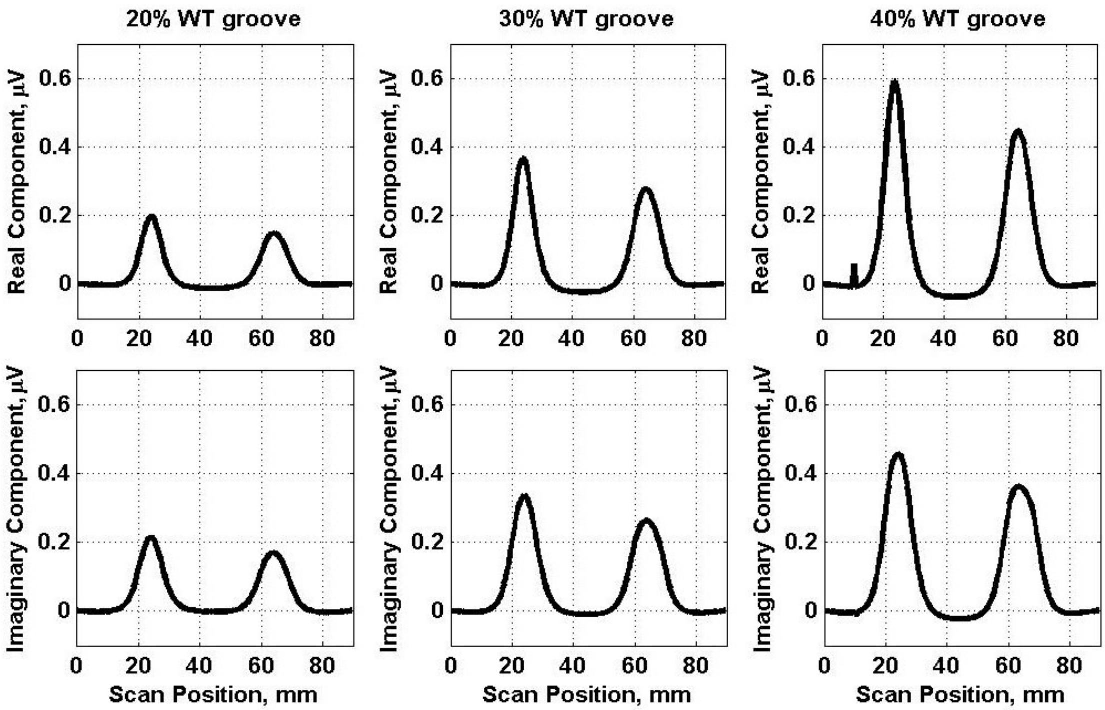

Figure 5.15 Results of Mix-1 (825 & 725 Hz) for different wall thinning grooves.

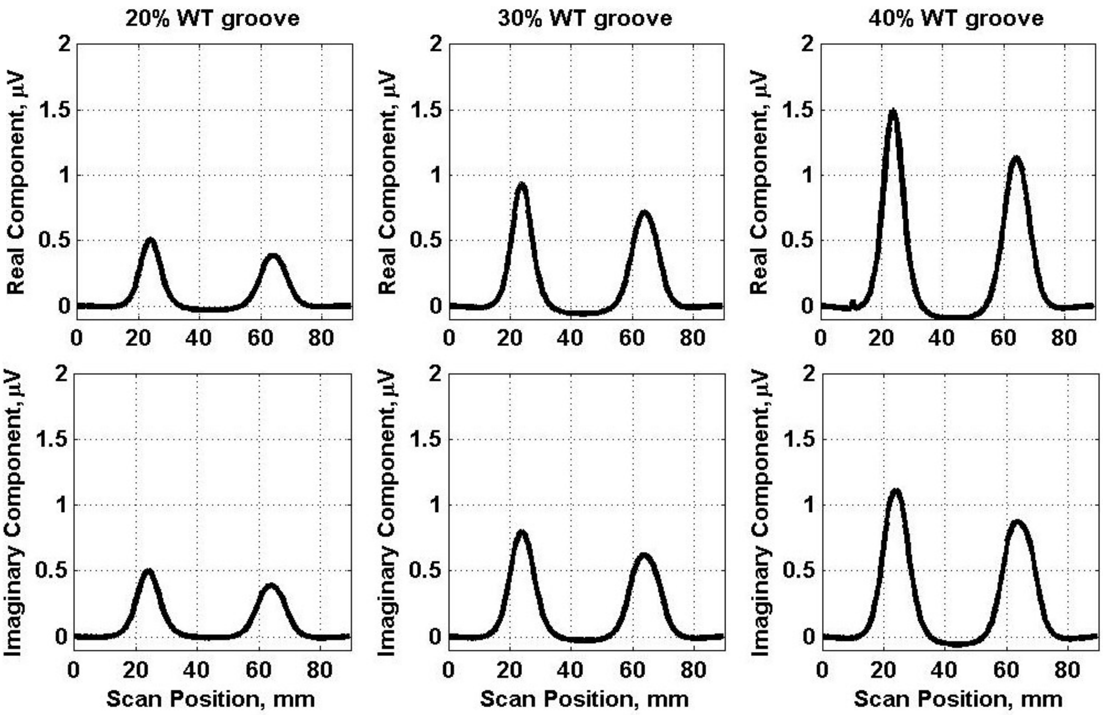

Figure 5.16 Results of Mix-2 (825 & 625 Hz) for different wall thinning grooves.

Euclidian distance (Metric-1) and cross correlation (Metric-2) metrics have been used for comparing Mix-1 and Mix-2 performance. Metric-1 was calculated as the sum of the Euclidian distance of the individual impedance data and Metric-2 was calculated as the maximum cross correlation between mix signals and the 20% WT thinning grooves signal. Larger values of Euclidian distances and smaller values of cross correlation means better performance and complete elimination of the support structure signature. The computed performance metrics for the Mix-1 and Mix-2 are given in Table 5.2. Observation of Table 5.2 reveals that the performance of the Mix-2 is better for eliminating the influence of the support structure signals.

Table 5.2 Similarity metric to assess the performance of the Mix-1 and Mix-2.

Groove depth	Mix-1 (825 Hz -725 Hz)		Mix-2 (825 Hz -625 Hz)	
	Metric1- (sum of Euclidian distance)	Metric-2 (Max. cross correlation)	Metric1- (sum of Euclidian distance)	Metric-2 (Max. cross correlation)
20% WT	383.44	62.47	387.30	25.87
30% WT	379.53	108.71	385.08	44.60
40% WT	376.57	166.33	382.23	67.87

In order to check the robustness of the LKT algorithm, RFEC signals of a 20% WT groove, fully off-centered, (CASE-I) and partially off-centered with the support structure (CASE-II) have been subjected to mixing. A schematic of the CASE-I and CASE-II defects are shown in Figure 5.17 and Figure 5.18 show the raw RFEC signals for CASE-I defect under support structure at 825 Hz and 625 Hz. Due to positional influence of the defect, one of the RFEC signal peaks has been highly influenced by the support structure, while the other peak remains predominantly unperturbed. Figure 5.18 also shows the result of the dual frequency mixing. Figure 5.19 shows the raw and mixed RFEC signals for the CASE-II defect under support structure.

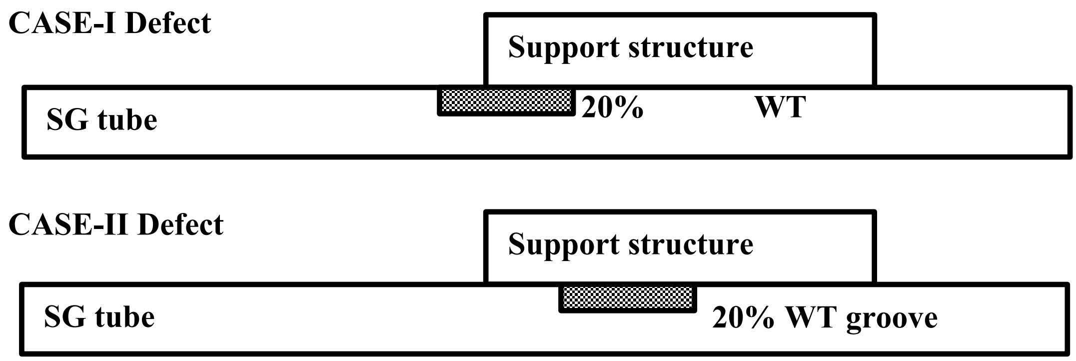

Figure 5.17 Schematic of the CASE-I and CASE-II defects under support structures.

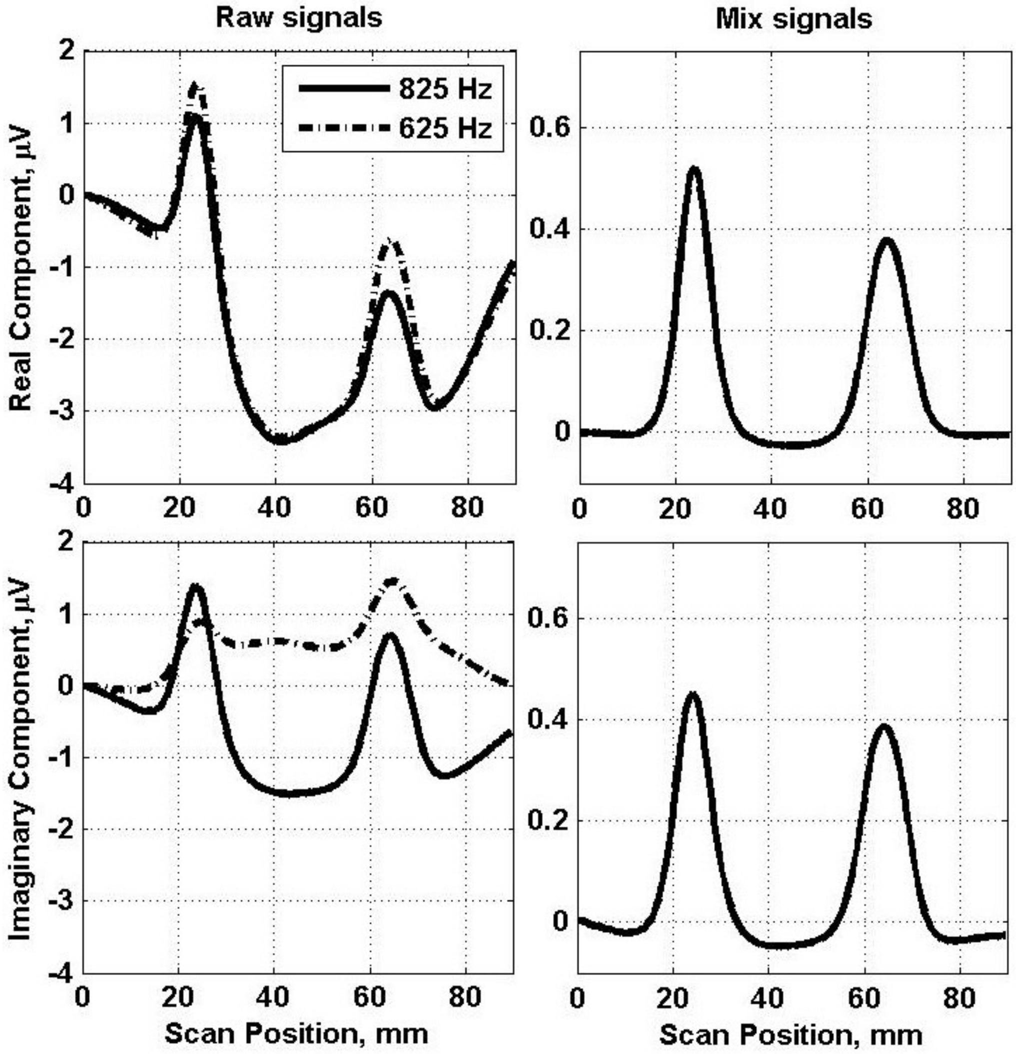

Figure 5.18 Raw and mixed RFEC signals of a 20% WT groove partly outside the support structure (CASE-I).

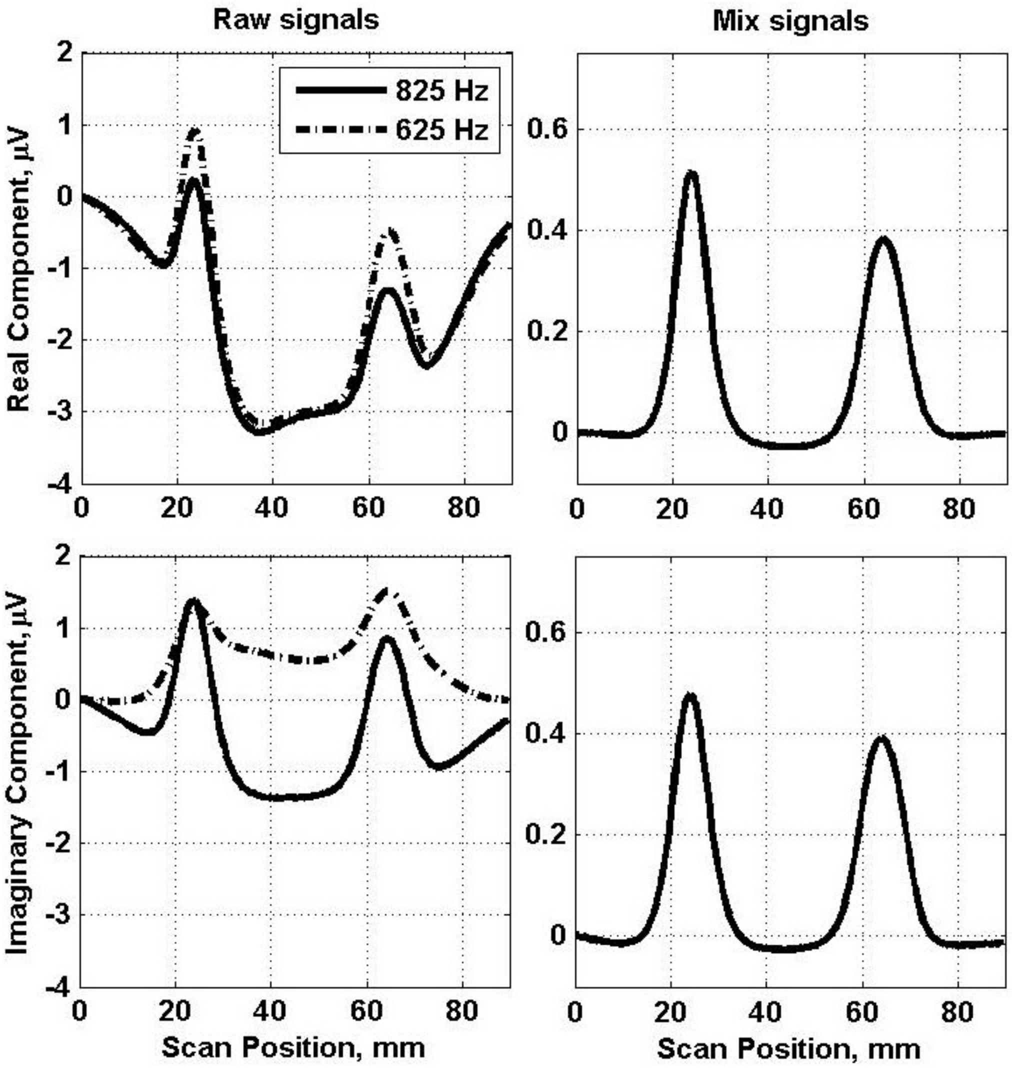

Figure 5.19 Raw and mixed RFEC signals of a 20% WT groove off-centred with the support structure (CASE-II).

In both CASE-I and CASE-II defects, complete suppression of the support structure signal have been observed. The mixed RFEC signals of the 20% WT groove, in both the cases, is same as that of the RFEC signals shown in Figure 5.16, in which the groove was present exactly at the center of the support structure. Thus the study reveals that there would not be any loss of information due to mixing, when the defects are located at different axial positions with respect to the support structure. The observations also proves the point that the dual frequency mixing algorithm based on the LKT has been robust enough to suppress the influence of support structure and bring out the genuine RFEC signals of defects when the defects are present anywhere in the vicinity of the support structure.

5.10 Discussion

Model based investigations of the sodium deposits in the defect regions revealed that the presence of sodium strengthen the distribution of eddy currents in sodium. This would result in the reduction of detector coil voltage. The valley formation is mainly due to the pull down of the RFEC signals of grooves below the baseline. A parametric study of the model also clearly indicates that the Peak-to-Peak parameter is invariant for small amounts of sodium.

The experimental and the model based investigations have clearly established the fact that the invariant parameter based approach is promising for detection as well as sizing of defects in the presence of stray sodium deposits in the defects. The valley depth as presented in the previous section is mainly due to the conducting nature of the sodium and also proportional to the amount of sodium deposit in the defects. This fact can lead to situations wherein a small size defect is completely filled with excess amount sodium. In such situations, the valley depth might be higher resulting in the merger of the characteristic RFEC peaks with the valley, so that, it would not be possible to estimate the peak-to-peak amplitude parameter of the RFEC signals. Hence, the invariant parameter based approach is subjective to the amount of sodium present in the defects and also the size of the defects. Dual frequency mixing is also a potential approach for detecting defects in the presence of sodium.

The RFEC signals of defects under support structure are characteristically similar to the defects filled with remnant sodium. But, it is qualitatively different with sodium deposits which are random in nature, tend to fill the defects and high in electrical conductivity. On the contrary, the support structures always have fixed size and are an extra buildup of material on the OD side and low in electrical conductivity. Due to larger width of the support structure, its influence of the RFEC signals is much higher than the sodium influence. The invariant parameter identification approach highlighted in the previous sections would also be useful for detecting defects in the presence of support structures. However, due to larger influence of the support structure, it might not be possible to identify the peak-to-peak amplitude parameter, especially, for smaller size defects. During actual inspection of SG tubes, a different situation may arise in which the sodium deposits might form around the support structures and influence the RFEC signals. In such circumstances, it is important to eliminate one variable first, to study the effect of other. Hence, multifrequency mixing is an essential step in studying the defect detection in the presence of support structures.

Selection of the secondary frequency is another important aspect when dual frequency mixing is performed. The rule of thumb in conventional EC testing is to select a frequency which is sub harmonic of the primary frequency. For example, if 100 kHz is the primary frequency, 50 kHz would be chosen as the secondary frequency for effectively eliminating the support structure influence. However, adopting such criteria is difficult in RFEC testing, owing to the fact that, well defined transition and RFEC regions might not exist in the sub harmonic frequency. On the other hand, selection of a close by frequency is also meaningless, as it would result in larger redundancy in the input data to the mixing algorithm, which might result in singular matrix for solving the simultaneous equations. It should also be noted that the RFEC probe has been optimized for a fixed frequency of 825 Hz. However, when secondary frequencies are applied in the same probe, there is a chance that the remote field regions would shift resulting in change in the RFEC signals. In this study, it was ensured that the receiver coil was placed in the RFEC region to predominantly receive indirectly coupled field. Moreover, clear transition and RFEC regions have been observed after 600 Hz (refer Section 3.8). The optimum frequency chosen for detecting OD defects is 825 Hz. Hence, 625 Hz and 725 Hz were chosen for support structure elimination.

5.11 Summary

1) Experimental studies carried out in a sodium test facility, to investigate the influence of sodium deposits on RFEC signals of defects present in the SG tubes. Four numbers of 1.5 m long SG tubes having artificial grooves welded to a specially designed sodium test vessel for this study.
2) RFEC testing of the SG tubes carried out at simulated test conditions identical to actual ISI. Scattered deposits of sodium in smaller quantities were observed on the outer surface of the tubes in defect-free regions. These scattered deposits produced small amplitude variations which were below the measurable limits of the instrument. The signal would be measureable if the deposits are large enough at least volumetrically equivalent to 5% WT groove. Residual sodium was observed in artificial grooves and the quantity of sodium was found to be relatively more in less-width grooves due to the combined effect of surface tension and capillary action. A definite influence of sodium deposits was observed on the RFEC

signals. For the first time, formation of a valley was observed between characteristic RFEC peaks due to sodium in the defects.

3) The valley depth was found to be proportional to the volume of sodium deposit in the defect. The signal Peak-to-Peak amplitude was found to be independent of the sodium deposit; as a result, this invariant parameter could be reliably used for sizing of defects with appropriate calibration graphs.
4) This study clearly brought out the important point that sodium deposits do not significantly influence detection and sizing of defects in SG tubes, based on the experimental studies carried out using uniform wall loss grooves and also confirmed by the model.
5) A new LKT based mixing algorithm has been developed to eliminate the influence of support structures made of Inconel-718 on RFEC signals of defects. The kernel matrix used Gaussian function. Iterative gradient based error minimization technique has been applied for optimizing the weights.
6) The mixing algorithm has been successfully applied on model predicted RFEC signals of wall thinning grooves of 20%, 30% and 40% deep groves under support structures. RFEC signals of wall loss grooves have been obtained from FE model predictions at 825 Hz (optimized frequency), 725 Hz and 625 Hz. The mixing algorithm was applied to 825 Hz & 725 Hz and 825 Hz & 625 Hz signals to eliminate support structures.
7) The mixing combinations have been compared with the RFEC signals of the support structure at 825 Hz based on Euclidian distance and cross correlation based metrics. Near complete suppression of the support structure signals has been observed when 825 and 625 Hz frequencies were used for mixing.

8) The robustness of the mixing algorithm has been validated for 20% WT deep grooves partially and fully off-centered with the support structure. The mixing results have been found to be identical in both the cases.

Chapter 6: Conclusions

A finite element model incorporating the nonlinear magnetic behavior has been applied to study the remote field eddy current technique, in this research work. This model has been used to identify the direct, transition and remote field regions in small diameter (17.2 mm OD and 2.3 mm thick) modified 9Cr-1Mo ferromagnetic steam generator (SG) tubes used in Prototype Fast Breeder Reactor (PFBR) in India. The model predicted that the RFEC region lies beyond 36 mm with respect to the center of the excitation coil for the SG tubes. Based on the predicted amplitude of the RFEC signals of various defects in the SG tubes, the optimum frequency has been found to be 825 Hz. The efficacy of the nonlinear model has been found to be better than a linear model, especially at higher excitation currents. The model based studies have been found to be useful to precisely position the receiver coil in the RFEC region (>36 mm) and to accurately identify the optimum frequency (825 Hz). This model based optimization approach has clearly enabled enhanced detection of defects in the SG tubes.

A high sensitive RFEC instrument has been developed using a stable constant current excitation source with a total harmonic distortion (THD) less than 3%. A lock-in amplifier based high sensitive receiver unit with high dynamic range data acquisition capabilities has been incorporated for measuring small amplitude receiver coil voltages from localized defects. Flexible RFEC probe has been designed and developed as per the model predictions to negotiate the bend regions of the SG tubes and operated at the optimum frequency of 825 Hz. The FE model predicted RFEC signals of grooves of depths 0.46 mm (20% WT), 0.69 mm (30% WT), and 0.92 mm (40% WT) have been compared with that of the experimental measurements. The difference has been found to be less than 5%. The RFEC instrument and optimized probe could reliably detect longitudinal as well as circumferential notches as small as 0.46 mm (20% WT) in the straight sections of the SG tube. The sensitivity of this instrument has been found to be superior to a commercial RFEC instrument operating at same test condition. The RFEC instrument and probe developed in this work has resulted in high sensitive detection of localized defects in SG tubes.

A continuous wavelet transform (CWT) based signal processing approach has been proposed, for the first time, to process RFEC signals from bend regions of the SG tubes. The performance of the CWT based signal processing approach has been compared with Fourier filtering and template based cross correlation, signal processing techniques. The CWT approach using the optimum Bior2.8 wavelet has shown the noise reduction capability of Fourier filtering and the signal enhancement capability of the cross-correlation techniques. The CWT approach has unambiguously detected 10% WT deep grooves present anywhere in the bend regions, which otherwise would have been missed. An improvement in the SNR of 7 dB from 1.02 dB has been observed for RFEC signals from the bend regions by the application CWT approach. The study has also brought out a new finding that two separate calibration graphs need to be employed for bend and straight tubes for sizing of defects, subsequent to the application of signal processing approach.

Experimental study has been carried out in a sodium test facility, to investigate the influence on RFEC signals due to sodium deposits in the defective regions of SG tubes. RFEC signals obtained from machined artificial grooves exposed to sodium in a test vessel revealed that there is a definite influence of the sodium deposits. Formation of a valley between characteristic RFEC peaks due to sodium deposits has been observed for the first time. The valley depth has been found to be proportional to the volume of sodium deposit in the defect. However, the peak-to-peak amplitude of the RFEC signals has been found to be same with and without sodium deposits in the defects. This invariant parameter has been found to be useful for detecting and sizing of defects filled with sodium deposits. The experimental studies have provided a thorough understanding of the sodium influence on RFEC signals. The approach based on identifying an invariant parameter has given enough confidence to carry out ISI of the SG tubes even with the presence of sodium.

A new linear kernel transform (LKT) based mixing algorithm has been proposed to eliminate strong disturbing noise in the RFEC signals of defects due to support structures made of Inconel-718. The mixing algorithm has been successfully applied for model predicted RFEC signals of grooves of depths 0.46 mm (20%WT), 0.69 mm (30%WT), and 0.92 mm (40% WT), under support structures at 825 Hz (optimized frequency), 725 Hz, and 625 Hz. Two different mixing combinations have been considered viz., 825 & 725 Hz and 825 & 625 Hz and their performance have been compared using Euclidean distance and cross correlation metrics. The mixing output has been found to be free from the influence of support structure signal, when RFEC signals from 825 Hz and 625 Hz have been considered. The robustness of the mixing algorithm has been validated for grooves lying partially and fully off-centered with the support structure. The mixing results have been found to be identical in all the cases. Thus, the LKT based mixing algorithm provides a reliable and robust approach for detection of defects under the support structures of the SG tube.

The approaches presented in this thesis are useful for realizing a comprehensive RFEC technology for ISI of the SG tubes. The research work has also resulted in a field worthy RFEC instrument capable of detecting linear as well as volumetric defects in straight sections, bend regions, and under support structures of the SG tubes. Availability of such a dedicated ISI technique will enable assessment of structural integrity of the SGs. This technology, in turn, will ensure safety of the SGs and will enable achieving higher plant availability factors.

6.1 Technical and scientific contribution

This thesis has provided a deeper insight into the RFEC phenomenon through the nonlinear FE model which essentially conveys the point that for higher excitation currents there is a considerable difference in the behavior of linear and nonlinear models. It could also be derived from the studies that an equivalent linear model can be performed, provided an appropriate magnetic permeability value is chosen. Through systematic studies, for eliminating unwanted signals from the bend regions of the SG tubes, the thesis has clearly brought out the characteristics of CWT based processing technique, which inherits the features of both Fourier filtering and cross correlation techniques. The thesis highlighted for the first time, the need to employ separate calibration graphs for straight and bend regions of the SG tubes after the application of signal processing technique for the bend regions. The effect of sodium deposits on the RFEC signals has been studied through numerical modeling and experiments for the first time. An invariant parameter, peak-to-peak amplitude has been proposed for detection and sizing of defects in the presence of sodium deposits. Overall, this thesis showed a way to efficiently apply the RFEC technique for ISI of small diameter ferromagnetic tubes and this will immensely contribute to the safety and reliability.

Chapter 7: Future works

The active length of RFEC probe is more than 50 mm. This will leave significant length uninspected on either side of the tube. In this regard, approaches to reduce the probe length are useful. The model based approach proposed in this study is beneficial in various ways such as studying the shifting of the direct, transition and remote field regions when conducting and magnetic shielding is employed in the RFEC probe. This aspect has not been studied in the present work. Such conducting and magnetic shielding is expected to further enhance the detectability and to effectively reduce the probe size. 2D axi-symmetric model has been used in this study, exploiting the cylindrical symmetry of coil and tube to evolve and optimize the proposed approaches. However, 3D nonlinear model is necessary to study influence of localized defects. Development of computationally efficient 3D finite element model incorporating the nonlinear material properties is a potential future problem.

In this research work, conventional inductive coil based RFEC sensor has been used. However, the detection performance and the spatial resolution of the RFEC technique could further be improved with the use of high sensitive solid state sensors such as Hall, Giant Magneto Resistance (GMR) and Giant Magneto Impedance (GMI) sensors. It is attractive to explore, the off-chip GMR sensors in place of inductive receiver coil of the RFEC probe, which can be arranged in an array fashion for localization of the defects in the SG tubes. The RFEC instrument developed as part of this research work is laboratory worthy. However, a modular design approach would be more effective towards realizing a compact, computer controlled and portable field worthy RFEC instrument. Further, pulsed excitation enabling testing at several frequencies will also be attractive.

The influence of bending stresses on RFEC signals has not been studied in the present work, as the stresses are assumed to be uniformly distributed and expected to be relived under high temperature sodium environment. Further identical bending procedure was followed for all the SG tubes. However, there could be situations where the bending stresses are different. In such situations, it is essential to carry out systematic studies to measure the bending stresses by different NDE techniques and to analyze their influence. Understanding the RFEC characteristics in the bend regions may also be beneficial for design and development of efficient probes without the need for signal processing. 3D finite element models are required for this purpose, which are computationally expensive. Nonlinear FE modeling of the bend regions is highly involved. Use of hybrid and scale down models would be beneficial in this context. Coordinate transformation to effectively reduce the 3D bend tube geometry into 2D axi-symmetric geometry would also be effective to model the bend regions.

The experimental investigations carried out to understand the influence of sodium, are limited straight sections of SG tubes. However, systematic experimental as well as model based investigations may be desirable to study the variation in the RFEC signals with sodium deposits in defects in the bend regions.

Sizing of the defects has not been explored in this present study. Multi-parametric, multi-frequency approaches are attractive for defect sizing. Pulsed electromagnetic technique is a potential tool for assessing the material integrity at multiple frequencies in one go. RFEC using pulsed excitation would be attractive for quantitative characterization of defects in ferromagnetic components.

The RFEC technique and the proposed approaches can readily be applied to carbon steel piping in other industries such as oil and gas industries.

REFERENCES

[1] S C. Chetal, V. Balasubramaniyan, P. Chellapandi, P. Mohanakrishnan, P. Puthiyavinayagam, C.P. Pillai, S. Raghupathy, T.K. Shanmugham, and C. Sivathanu Pillai, "The design of the prototype fast breeder reactor," *Nuclear Engineering and Design*, vol. 236, pp. 852-860, 2006.

[2] T K. Mitra, Aravinda Pai, and Prabhat Kumar, "Challenges in manufacture of PFBR steam generators," *Energy Procedia*, vol. 7, pp. 317-322, 2011.

[3] S L. Mannan, S C. Chetal, Baldev Raj, and S B. Bhoje, *Transactions of Indian Institute of Metals,* vol. 56, no. 2, pp. 155-178, 2003.

[4] Y. Dai, X. J. Jia, and K. Farrell, "Mechanical properties of modified 9Cr–1Mo (T91) irradiated at ≤300°C in SINQ Target-3," *Journal of Nuclear Materials*, vol. 318, pp. 192-199, 2003.

[5] Riqiang Duan, Zhou Wang, Xianjong Yang, and Rui Luo, "Numerical simulation of sodium-water reaction products transport in steam generator of liquid metal fast breeder reactor on small water/steam leak," *Journal of Nuclear Science and Technology*, vol. 38, no. 7, pp. 527-532, July 2002.

[6] S. Kishore, A. Ashok Kumar, S. Chandramouli, B K. Nashine, K K. Rajan, and S C. Chetal P. Kalyanasundaram, "An experimental study on impingement wastage of Mod 9Cr 1Mo steel due to sodium water reaction," *Nuclear Engineering and Design*, vol. 243, pp. 49-55, 2012.

[7] *Nondestructive testing handbook - Nondestructive testing overview*, 2nd ed.: Columbus, OH: American Society for Nondestructive Testing, 1996, vol. 10.

[8] Baldev Raj, T. Jayakumar, and M. Thavasimuthu, *Practical nondestructive testing*, 3rd ed. New Delhi: Narosa Publishing House, 2007.

[9] International Atomic Energy Agency, IAEA-TECDOC-981.

[10] Baldev Raj, T. Jayakumar, and B P C. Rao, "Review of NDT techniques for structural integrity," *Sadhana*, vol. 20, pp. 5-38, 1995.

[11] S S. Udpa and P O. Moore, *Nondestructive testing handbook - Electromagnetic testing*, 3rd ed.: ASNT, 2004, vol. 5.

[12] B P C. Rao, *Practical eddy current testing*. New Delhi: Narosa Publishing House, 2007.

[13] H L. Libby, *Introduction to electromagnetic NDT methods*. New York: Wiley-Interscience, 1971.

[14] B P C. Rao, "Eddy current testing: Basics," *Journal of Nondestructive Testing and Evaluation*, vol. 10, no. 3, pp. 7-16, 2011.

[15] V S. Cecco, G. Van Drunnen, and F L. Sharp, "Eddy current manual test method," *AECL-7523*, vol. 1, November 1983.

[16] NDT Education Resource Center, 2001-2012, The collaboration for NDT education, Iowa State University. [Online]. http://www.ndt-ed.org

[17] Waikhom Sharatchandra Singh, *Optimization of GMR array sensor based magnetic flux leakage techniques using finite element modeling*. PhD dissertation, Homi Bhabha National Institute, Mumbai, India, July, 2013.

[18] Md. Afzal and S S. Udpa, "Advanced signal processing of magnetic flux lakage data obtained from seamless gas pipeline," *NDT&E International*, vol. 35, pp. 449-457, 2002.

[19] V. Moorthy and B A. Shaw, "Contact fatigue performance of helical gears with surface coatings," *Wear*, vol. 276-277, pp. 130-140, 2012.

[20] V. Moorthy, S. Vaidyanathan, T. Jayakumar, and Baldev Raj, "Microstructural characterisation of tempered and deformed ferritic steels using magnetic Barkhausen emission technique," *Journal of Nondestructive Evaluation*, vol. 20, no. 4, pp. 33-39, 2000.

[21] V. Moorthy, S. Vaidyanathan, T. Jayakumar, and Baldev Raj, "On the influence of tempered microstructures on magnetic Barkhausen emission in ferritic steels," *Philosophical Magazine*, vol. 77, no. 6, pp. 1499-1514, 1998.

[22] Giuseppe Sposito, *Advances in potential drop techniques for nondestructive testing*. PhD dissertation, Imperial College London, UK, 2009.

[23] R. Nagendran, N. Thirumurugan, N. Chinnasamy, M P. Janawadkar, R. Baskaran, L S. Vaidhyanathan, and C S. Sundar, "Optimum eddy current excitation frequency for subsurface defect detection in SQUID based non-destructive evaluation ," *NDT&E International*, vol. 43, no. 8, pp. 713-717, 2010.

[24] Unsang Park, Lalita Udpa, and George C. Stockman, "Motion-based filtering of magneto-optic imagers ," *Image Vision Computing*, vol. 22, pp. 243-249, January

2004.

[25] Shuaib Ahmed, S. Thirunavukkarasu, B P C. Rao, and T. Jayakumar, "Competitive learning on cosine similarity method for classification of defects in two-layered metallic structures," *Studies in Applied Electromagnetics and Mechanics*, vol. 36, pp. 183-191, 2012.

[26] B P C. Rao, Baldev Raj, T. Jayakumar, and P. Kalyanasundaram, "Using artificial neural networks to quantify discontinuities in eddy current testing," *Materials evaluation*, vol. 60 , no. 1, pp. 84-88, 2002.

[27] K V. Rajkumar, B P C.Rao, B.Sasi, Anish Kumar, T. Jayakumar, Baldev Raj, and K K. Ray, "Characterisation of ageing behaviour inM250 grade maraging steel using eddy current non-destructive methodology," *Materials Science and Engineering-A*, vol. 464, no. 1, pp. 233-240, 2007.

[28] S. Thirunavukkarasu, B P C. Rao, T. Jayakumar, N. Narayanankutty, and P V. Prabhakaran, "Eddy current based assessment of thickness of silicon carbide coating on carbon-carbon composites," *Journal of Aerospace Sciences and Technology*, vol. 63, no. 3, pp. 223-229, August 2011.

[29] B. Sasi, B P C. Rao, T. Jayakumar, and Baldev Raj, "Characterisation of solution annealed VT-14 titanium alloy using eddy current based electrical resistivity measurements," *Transactions of Indian Institute of Metals*, vol. 63, no. 5, pp. 773-777, 2010.

[30] "Standard guideline for eddy current examination of non-ferromagnetic heat exchanger tubing," ASME Boiler and Pressure Vessel Code, Section V - Nondestructive Examination, Article 8, 2010.

[31] K. Arunachalam, S. Kumar, M. Kumar, S. Soo, U. Parrikar, P. Ramuhalli, L. Udpa, S S. Udpa, and J. Benson, "Development of automated analysis algorithms for rotating probe data," in *the Proceedings of the 24th Annual EPRI Steam Generator NDE Workshop*, San Diego, CA, July 11-13, 2005.

[32] [Online]. http://www.zetec.com/wp-content/uploads/2010/06/ds_xprobe.pdf

[33] P J. Shull, *Nondestructive evaluation: theory, techniques and applications*. New York: Marcel Dekkar, Inc., 2002.

[34] "RCCMR code: Design and construction rules for mechanical components for

nuclear installations -Section 3: Examination methods, RMC-2000, Ultrasonic examination, RMC-6000, Eddy current examination of tubular productsions," RCCMR Codes,.

[35] B P C. Rao, S. Thirunavukkarasu, T. Jayakumar, and Baldev Raj, "An approach for stringent quality assurance of steam generator tubes," *Insight, British Journal of Non Destructive Testing and Condition Monitoring*, vol. 49, pp. 698-700, 2007.

[36] B. Sasi, B P C. Rao, S. Vaidyanathan, S. Thirunavukkarasu, T Jayakumar, and P. Kalyanasundaram, "On the quality control of ferromagnetic steam generator tubes of prototype fast breeder reactor," *Journal of Non-Destructive Testing and Evaluation*, vol. 21, no. 1, pp. 41-46, 2001.

[37] W R. McLean, "Apparatus for magnetically measuring thickness of ferrous pipe," 2,573,799, November 6, 1965.

[38] T R. Schmidt, "History of remote-field eddy current inspection technique ," *Materials Evaluation* , vol. 47, no. 1, pp. 14-22, 1989.

[39] T R. Schmidt, "The casing inspection tool – An instrument for the in-situ detection of external corrosion in oil wells," *Corrosion*, vol. 17, no. 7, pp. 14-22, 1989.

[40] Y S. Sun, W. Lord, L. Udpa, S S. Udpa, S K. Lua, K H.Ng, and S. Nath, "Thick-walled aluminum plate inspection using remote field eddy current techniques," *Review of Progress in Quantitative Nondestructive Evaluation* , vol. 16, no. , pp. 1005-1012, 1997.

[41] Markus Witte, "Weld seam inspection of thick wall austenitic steel tubes beyond standard eddy current technology," in *the Proceedings of the European Conference on NDT (ECNDT)*, 2006, p. Paper id. We. 2.6.3.

[42] T R. Schmidt, D L. Atherton, and S. Sullivan, "The remote field transition zone," *Materials Evaluation*, vol. 47, pp. 969-979, September 1989.

[43] H. Ostermeyer, "New aspects of remote field eddy current probe development," in *the Proceedings of the 7th European conference on NDT*, 1998, pp. 2569-2575.

[44] D L. Atherton, D D. Mackintosh, S. Sullivan, J M S. Dubois, and T R. Schmidt,

"Remote field eddy current signal representation," *Materials Evaluation*, vol. 51, no. 7, pp. 782-789, 1993.

[45] S. Thirunavukkarasu, B P C. Rao, S. Vaidyanathan, T. Jayakumar, and Baldev Raj, "Influence of sodium deposits in steam generator tubes on remote field eddy current signals," *International Journal of Pressure Vessels and Piping*, vol. 85, no. 4, March 2008.

[46] R. Palanisamy, "Remote field eddy current testing – A Review," *Review of Progress on Quantitative Nondestructive Evaluation*, vol. 7, pp. 157-164, 1988.

[47] Anmol Birring. Eddy current testing Vs. ultrasonic IRIS for inspection of heat exchanger tubing. [Online]. http://www.nde.com/ECT%20vs%20IRIS.pdf

[48] D. Mackintosh and B. Beresford, "Probes for remote field eddy current testing of heat exchangers: Configurations and capabilities," *Materials Evaluation*, vol. 63, no. 3, pp. 292-296, March 2005.

[49] Albert Teitsma, Stephen Takach, Julie Maupin, Jennifer Fox, Paul Shuttleworth, and Paul Seger, "Small diameter remote field eddy current inspection for unpiggable pipelines," *Journal of Pressure Vessel Technology*, vol. 127, p. 269, August 2005.

[50] R. Palanisamy, "Electromagnetic field calculations for the low frequency eddy current testing of tubular products," *IEEE Transactions on Magnetics*, vol. 23, no. 5, pp. 2663-2665, September 1987.

[51] W. Lord, Y S.Sun, S S. Udpa, and S. Nath, "Physics of the remote field eddy current effect," *Review of Progress on Quantitative Nondestructive Evaluation*, vol. 7, pp. 165-172, 1988.

[52] Young Kil Shin, Tae Eon Chung, and William Lord, "Remote field eddy current technique applied to the inspection of nonmagnetic steam generator tube," *Review of Progress in Quantitative Nondestructive Evaluation*, vol. 20, pp. 392-399, 2001.

[53] Musolino, R. Rizzo, and E. Tripodi, "A quasi-analytical model for remote field eddy current inspection," *Progress in Electromagnetics Research*, vol. 26, pp. 237-249, 2012.

[54] M. Ovidiu, T. Yamaguchi, M. Ueda, and T. Yamashita, "Experimental

confirmation of 3D numerical simulations of remote field signals from defects in magnetic steam generator tubes," *Review of Progress in QNDE*, vol. 25, pp. 391-398, 2005.

[55] Y. Zhang and D. L. Atherton, "Finite element analysis for remote field eddy current responses for near and far side cracks," *Research in Nondestructive Evaluation*, vol. 10, pp. 163-169, 1998.

[56] Lin He-Yun and Sun Yu-Shi, "Application of `zoom-in' technique in 3D remote field eddy current effect computation," *IEEE Transaction on Magnetics*, vol. 6, no. 2, pp. 881-884, 1990.

[57] D L. Atherton, S. Sullivan, and M. Daly, "A remote field eddy current tool for inspecting nuclear reactor pressure tubes," *British Journal of Nondestructive Testing*, vol. 30, no. 1, pp. 22-28, 1988.

[58] J M S. Dubois, D L. Atherton, W. Czura, and T R. Schmidt, "Circumferential groove defect characterization in the remote field eddy current transition zone," *British Journal of nondestructive testing*, vol. 34, no. 8, pp. 401-406, 1992.

[59] J. Bruce Nestleroth, "Innovative electromagnetic sensors for pipeline crawlers," vol. doi: 10.2172/875411, 2005.

[60] D L. Atherton, T R. Schmidt, T. Svendson, and E V. Rosen, "Effects of remote-field exciter coil tilt and eccentricity in a steel pipe," *Materials Evaluation*, vol. 50, no. 1, pp. 44-50, 1992.

[61] J. Sutherland and D.L. Atherton, "Effects of bending stresses and tubes curvature on remote field eddy current signals," *Materials Evaluation*, vol. 55, no. 1, pp. 85-89, 1997.

[62] E V. Rosen and D L. Atherton, "Effect of shielding and exciter coil tilt on the remote field effect," *Materials Evaluation*, vol. 51, no. 1, pp. 66-71, 1993.

[63] S S. Udpa, T H. Ou-Yang, and W. Lord, "Signal processing for remote field eddy current inspection technique ," *Review of Progress in QNDE*, vol. 7A, no. 831-838, June 1987.

[64] L.A.N.M. Lopez, D.K.S. Ting, and B.R. Upadhyaya, "Removing eddy-current probe wobble noise from steam generator tubes testing using wavelet transform," *Progress in Nuclear Energy*, vol. 50, pp. 828-835, 2008.

[65] A. Shatat and D L. Atherton, "“Remote field eddy current inspection of support plate fretting wear”," *Materials evaluation*, vol. 55, no. 3, pp. 361-366, 1997.

[66] Ovidiu Mihalache, Toshihiko Yamaguchi, and Masashi Ueda, "Investigations of multifrequency algorithms for detection of defects in FBR magnetic steam generator tubes covered with sodium," *Journal of Advanced Maintenance, Japan Society of Maintenology*, vol. 1, pp. 68-76, 2009.

[67] Ovidiu Mihalache, Toshihiko Yamaguchi, and Masashi Ueda, "Computational challenges in numerical simulations of ISI of ferritic steam generator tubes in fast breeder reactors using eddy currents and multi-frequency algorithms," *E-Journal of Advanced Maintenance, Japan Society of Maintenology*, vol. 3, no. 2, pp. 54-77, 2011.

[68] M V K. Chari and S J. salon, "Numerical methods in electromagnetism," *Academic Press*, 2000.

[69] K B. Baltzis, "The FEMM package: A simple, fast, and accurate open source electromagnetic tool in science and engineering," *Journal of Engineering Science and Technology Review*, vol. 1, pp. 83-89, 2008.

[70] Y. Tian, Y. Li, L. Udpa, and S S. Udpa, "Simulation of the world federation's second eddy current benchmark problem," *Review of progress in Quantiative Nondestructive Evaluation (QNDE)*, vol. 22, CP 657, pp. 1816-1823, 2003.

[71] N. Ida, "Numerical modeling for electromagnetic non-destructive evaluation," 1995.

[72] J. Jin, *The finite element method in electromagnetics*. New York: John Wiley & Sons, Inc. Publication, 2002.

[73] [Online]. http://www.femm.info/wiki/HomePage

[74] [Online]. http://www.netlib.org/voronoi/

[75] M. Pattabiraman, R. Nagendran, and M P. Janawadkar, "Rapid flaw depth estimation from SQUID-based eddy current nondestructive evaluation," *NDT&E International* , vol. 40 , pp. 289–293, 2007.

[76] D. O'Kelly, "Hysteresis and eddy current losses in steel plates with nonlinear magnetization characteristics," *Proceedings of the IEE*, vol. 119, no. 11, pp. 1675-1676, November 1972.

[77] A G. Jack and B C. Mecrow, "Methods for magnetically nonlinear problems involving significant hysteresis and eddy currents," *IEEE Transactions on Magnetics*, vol. 26, no. 2, pp. 424-429, March 1990.

[78] Richard L. Stoll, *The analysis of eddy currents (Monographs in electrical and electronic engineering)*.: Clarendon Press, 1974.

[79] W L. Soong, "BH curve and iron loss measurements for magnetic material," *Power engineering briefing note series No. 5*, pp. 3-4, May 2008.

[80] D L. Atherton, W. Czura, and D A. Lowther, "Open-boundary finite element calculations for remote field eddy current systems," *IEEE Transactions on Magnetics*, vol. 26, no. 5, pp. 2863-2864, September 1990.

[81] R W. Freund, "Conjugate gradient-type methods for linear systems with complex symmetric coefficient matrices," *SIAM Journal of Scientific and Statistical Computing*, vol. 13, no. 1, pp. 425-448, , January 1992.

[82] Michael T. Heath, "Chapter 11-Iterative methods for linear systems," in *Scientific Computing - An Introductory Survey*.: McGraw Hill, 1997.

[83] J M S. Dubois, D L. Atherton, and T R. Schmidt, "Remote field transition zone results in steel pipe," *British Journal of NDT*, vol. 34, no. 5, pp. 227-233, 1992.

[84] H. Hoshikawa, K. Koyama, J. Koido, and Y. Ishibishi, "Characteristics of remote field eddy current technique," *Materials Evaluation*, vol. 47, pp. 93-97, January 1989.

[85] *NI Lock-in amplifier start-up kit, User Manual*.: National instruments, 2002.

[86] B P C. Rao and N. Nakagawa, "A study of boundary element eddy current model validation," *Review of progress in Quantitative Nondestructive Evaluation (QNDE)*, vol. 25, 2005.

[87] S. Thirunavukkarasu, B. Purna Chandra Rao, S. Shuaib Ahmed, and T. Jayakumar, "Solution to the third eddy current benchmark problem of WFNDE centres," *Journal of Nondestructive testing Evaluation*, vol. 11, no. 2, pp. 42-46, September 2012.

[88] K. Sanjit Mitra, *Digital signal processing – A Computer-based approach*.: McGraw-Hill publishing Ltd., ISBN-13:978-0-07-066756-3 and 10:-0-07-066756-X, 2008.

[89] Michael T. heath, *Scientific Computing - An introductory Survey.*: The McGraw Hill Companies, 1997.

[90] S G. Mallat, "Multifrequency channel decompositions of images and wavelet models," *IEEE transactions on Acoustics, speech and signal processing*, vol. 37, no. 1, pp. 2091-2110, December 1989.

[91] Daubechies, *Ten lectures on wavelets*. Philadelphia: CBMS-NSF- Regional conference series in Applied Mathematics, Society for Industrial and Applied Mathematics , 1992.

[92] S. Poornachandra, "Wavelet-based denoising using subband dependent threshold for ECG signals," *Digital Signal Processing*, vol. 18, pp. 49-55, 2008.

[93] C. Sidney Burrus, A. Ramesh Gopinath, and Haitoo Guo, *Introduction to wavelets and wavelet transform primer*. New Jersey: Prentice Hall, 1998.

[94] K. Arunachalam, O. Uduebho, S A. Kumar, P. Ramuhalli, J. Benson, L. Udpa, and S S. Udpa, "Defect profiling using multi-frequency eddy current data from steam generator tubes," *Studies in Applied Electromagnetics and Mechanics*, vol. 28, pp. 131-138, 2006.

[95] Ping Xiang, *Automatic multi-frequency rotating-probe eddy-current data analysis*. PhD dissertation, Iowa State University, Ames, Iowa, 2005.

[96] Vladimir N. Vapnik, *Statistical learning theory.*: John wiley & sons, 1998.

[97] Mark J. Embrechts, Boleslaw Szymanski, and Karsten Sternickel, "Chapter 10: Introduction to scientific data mining direct kernel methods and applications," in *Computationally intelligent hybrid systems: The fusion of soft computing and hard computing*. New York: Wiley, 2005, pp. 317-365.